

FINAL REPORT

MetalMapper: A Multi-Sensor TEM System for UXO
Detection and Classification

ESTCP Project MR-200603

FEBRUARY 2011

Mark Prouty
Geometrics

David C. George
G&G Sciences

Donald D. Snyder
Snyder Geoscience, Inc.

This document has been cleared for public release



REPORT DOCUMENTATION PAGE
*Form Approved
OMB No. 0704-0188*

The public reporting burden for this collection of information is estimated to average 1 hour per response, including the time for reviewing instructions, searching existing data sources, gathering and maintaining the data needed, and completing and reviewing the collection of information. Send comments regarding this burden estimate or any other aspect of this collection of information, including suggestions for reducing the burden, to the Department of Defense, Executive Services and Communications Directorate (0704-0188). Respondents should be aware that notwithstanding any other provision of law, no person shall be subject to any penalty for failing to comply with a collection of information if it does not display a currently valid OMB control number.

PLEASE DO NOT RETURN YOUR FORM TO THE ABOVE ORGANIZATION.

1. REPORT DATE (DD-MM-YYYY) 28-02-2011	2. REPORT TYPE Final Report	3. DATES COVERED (From - To) June 2006 – November 2010		
4. TITLE AND SUBTITLE MetalMapper: A Multi-Sensor TEM System for UXO Detection and Classification		5a. CONTRACT NUMBER W912HQ-06-C-0041		
		5b. GRANT NUMBER		
		5c. PROGRAM ELEMENT NUMBER		
6. AUTHOR(S) Mark Prouty David George Donald Snyder		5d. PROJECT NUMBER MR-0603		
		5e. TASK NUMBER		
		5f. WORK UNIT NUMBER		
7. PERFORMING ORGANIZATION NAME(S) AND ADDRESS(ES) Geometrics, Inc 2190 Fortune Drive San Jose, CA 95131		8. PERFORMING ORGANIZATION REPORT NUMBER		
9. SPONSORING/MONITORING AGENCY NAME(S) AND ADDRESS(ES) SERDP 901 N. Stuart Street Arlington, VA 22203		10. SPONSOR/MONITOR'S ACRONYM(S)		
		11. SPONSOR/MONITOR'S REPORT NUMBER(S)		
12. DISTRIBUTION/AVAILABILITY STATEMENT Approved for public release; distribution is unlimited				
13. SUPPLEMENTARY NOTES				
14. ABSTRACT The MetalMapper is an advanced time domain electromagnetic (TEM) system for application towards the detection and characterization of UXO. The antenna configuration includes 3 orthogonal transmitter loops and 7 tri-axial receiver loops. The system can be deployed in mapping (or detection configuration) wherein it acquires data along profiles while the antenna platform is in motion. However, the most important benefit of the elaborate antenna configuration is that it permits us to characterize a buried metallic target from measurements at a single spatial point located (approximately) above the target. This system is being commercialized by Geometrics, Inc (San Jose, CA).				
15. SUBJECT TERMS MetalMapper, UXO, Discrimination, Classification, Electromagnetic Induction, Time Domain Electromagnetic				
16. SECURITY CLASSIFICATION OF: a. REPORT U		17. LIMITATION OF ABSTRACT b. ABSTRACT U	18. NUMBER OF PAGES 109	19a. NAME OF RESPONSIBLE PERSON Mark Prouty
				19b. TELEPHONE NUMBER (Include area code) 408-954-0522

Table of Contents

Acronyms.....	v
Figures	vii
Tables.....	xii
Executive Summary.....	1
1. INTRODUCTION	3
1.1. BACKGROUND	3
1.2. OBJECTIVE OF THE DEMONSTRATIONS.....	3
1.3. REGULATORY DRIVERS	3
2. TECHNOLOGY	4
2.1. TECHNOLOGY DESCRIPTION	4
2.1.1. MetalMapper Hardware	4
2.2. TECHNOLOGY DEVELOPMENT.....	7
2.2.1. AOL System (2003-2005).....	7
2.2.2. AOL2 System.....	8
2.2.3. Other Advanced EM Systems	9
2.3. ADVANTAGES AND LIMITATIONS OF THE TECHNOLOGY	9
3. PERFORMANCE OBJECTIVES	13
3.1. OBJECTIVE: COMPLETE COVERAGE OF DEMONSTRATION SITE	14
3.1.1. Metric.....	14
3.1.2. Data Requirements.....	15
3.1.3. Success Criteria.....	15
3.2. OBJECTIVE: REPEATABILITY OF CALIBRATION STRIP MEASUREMENTS	15
3.2.1. Metric.....	15
3.2.2. Data Requirements.....	15
3.2.3. Success Criteria.....	15
3.3. OBJECTIVE: DETECTION OF ALL ITEMS OF INTEREST.....	15
3.3.1. Metric.....	15
3.3.2. Data Requirements.....	15
3.3.3. Success Criteria.....	15
3.4. OBJECTIVE: MAXIMIZE CORRECT CLASSIFICATION OF MUNITIONS	15
3.4.1. Metric.....	15
3.4.2. Data Requirements.....	16
3.4.3. Success Criteria.....	16

3.5. OBJECTIVE: MAXIMIZE CORRECT CLASSIFICATION OF NON-MUNITIONS ..	16
3.5.1. Metric	16
3.5.2. Data Requirements	16
3.5.3. Success Criteria	16
3.6. OBJECTIVE: SPECIFICATION OF NO-DIG THRESHOLD	16
3.6.1. Metric	16
3.6.2. Data Requirements	16
3.6.3. Success Criteria	16
3.7. OBJECTIVE: MINIMIZE NUMBER OF ANOMALIES THAT CANNOT BE ANALYZED	17
3.7.1. Metric	17
3.7.2. Data Requirements	17
3.7.3. Success Criteria	17
3.8. OBJECTIVE: CORRECT ESTIMATION OF TARGET PARAMETERS	17
3.8.1. Metric	17
3.8.2. Data Requirements	17
3.8.3. Success Criteria	17
3.9. OBJECTIVE: DYNAMIC-MODE SURVEY PRODUCTIVITY	17
3.9.1. Metric	19
3.9.2. Data Requirements	19
3.9.3. Success Criterion	19
3.10. OBJECTIVE: REPEATABILITY OF PARAMETER ESTIMATION	20
3.10.1. Metric	20
3.10.2. Data Requirements	20
3.10.3. Success Criteria	20
3.11. OBJECTIVE: STATIC-MODE SURVEY PRODUCTIVITY	20
3.11.1. Metric	21
3.11.2. Data Requirements	21
3.11.3. Success Criteria	21
4. SITE DESCRIPTION	22
4.1. SITE SELECTION	22
4.1.1. Standardized Demonstration Sites (APG and YPG)	22
4.1.2. Camp San Luis Obispo (SLO)	22
4.2. SITE HISTORY	23
4.3. SITE GEOLOGY	23

4.3.1. Standardized Sites	23
4.3.2. San Luis Obispo	23
4.4. MUNITIONS CONTAMINATION	24
4.4.1. Standardized Sites	24
4.4.2. San Luis Obispo	24
5. TEST DESIGN	25
5.1. CONCEPTUAL EXPERIMENTAL DESIGN	25
5.1.1. Target Detection (Mapping Survey)	25
5.1.2. Cued ID (Static Survey)	25
5.1.3. Post-Acquisition Analysis	26
5.2. SITE PREPARATION	26
5.3. SYSTEM SPECIFICATION	27
5.3.1. Antenna Platform	27
5.3.2. Signals and Timing	27
5.3.3. Data Acquisition: Dynamic Data	28
5.3.4. Post-Acquisition Data Processing: Dynamic Data	28
5.3.5. Post-Acquisition Processing: Static Data	29
5.4. CALIBRATION ACTIVITIES	29
5.5. DATA COLLECTION	30
6. DATA ANALYSIS AND PRODUCTS	33
6.1. PREPROCESSING	33
6.1.1. Dynamic Survey Data	33
6.1.2. Static Data	33
6.2. TARGET SELECTION FOR DETECTION	34
6.2.1. Detection at YPG	34
6.2.2. Detection at APG	35
6.2.3. Detection at Camp SLO	35
6.3. PARAMETER ESTIMATES	43
6.3.1. Implementation Issues	45
6.3.2. Meta-Parameters	47
6.4. CLASSIFIER AND TRAINING	50
6.4.1. Discrimination at YPG	51
6.4.2. Discrimination at APG	52
6.4.3. Discrimination at Camp San Luis Obispo	58

6.5. DATA PRODUCTS.....	74
7. PERFORMANCE ASSESSMENT	75
7.1. SITE COVERAGE	75
7.1.1. GPS Data Quality.....	75
7.1.2. Area Coverage - SLO.....	76
7.1.3.....	77
7.2. Repeatability of Test Strip Calibrations.....	77
7.2.1. Dynamic Calibrations	77
7.3. Target Detection.....	83
7.4. Analysis and Classification Performance	85
7.4.1. Maximize Correct Classifications - Munitions (see Section 3.4)	85
7.5. Maximize Correct Classification of Clutter	92
7.6. Operating Point Specification (No-Dig Threshold)	93
7.7. Minimization of Cannot Analyze Points.....	94
7.8. Correct Estimation of Parameters	94
7.8.1. Position Estimates.....	94
7.8.2. “Beta” Estimates	95
7.9. Dynamic-Mode Survey Productivity	99
7.10. Static-Mode Calibration Repeatability	101
7.11. Static-Mode Survey Productivity.....	101
8. COST ASSESSMENT.....	104
8.1. COST MODEL	104
8.1.1. Equipment Costs	105
8.1.2. Mobilization and Demobilization	105
8.1.3. Instrument Setup and Calibration	106
8.1.4. Dynamic Survey Costs.....	106
8.1.5. Static Survey Costs	106
8.1.6. Detection Data Processing	106
8.1.7. Discrimination Data Processing.....	106
8.2. COST DRIVERS	106
8.3. COST BENEFIT	106
9. IMPLEMENTATION ISSUES	107
10. REFERENCES	108
Appendix A: Points of Contact.....	110

Acronyms

Acronym	Definition
ALLTEM	USGS Advanced EM System
ANN	Artificial Neural Network
AOL	Advanced Ordnance Locator
APG	Aberdeen Proving Ground
ATC	Aberdeen Test Center
ATV	All-Terrain Vehicle
BRAC	Base Realignment And Closure
BUD	Berkeley UXO Discriminator
CRREL	Cold Regions Research & Engineering Laboratory
CSV	Comma Separated Values
DAQ	Data Acquisition
DF	Direct Fire
EM	Electromagnetic
EMI	Electromagnetic Interference
EOD	Explosive Ordnance Demolition
ESTCP	Environmental Security Technology Certification Program
E-W	East-West
FOM	Figure Of Merit
FUDS	Formerly Used Defense Sites
GDB	Geosoft Data Base
GPS	Global Positioning System
GX	Geosoft eXecutable
IDA	Institute for Defense Analyses
IF	Indirect Fire
LBL	Lawrence Berkeley Laboratories
MM	MetalMapper
MM/RMP	MetalMapper/RbstMultiPrince (Inversion Program)
MOI	Munitions Of Interest
MPV	Man-Portable Vector
NAVSEA	Naval Sea Systems Command
NI	National Instruments
NRL	Naval Research Laboratory
OM	Oasis Montaj
P0	Polarizability at t = 0
PC	Personal Computer
PCI	Peripheral Component Interface
PDF	Portable Document Format
POC	Points Of Contact
PXI	Compact Peripheral Component Interface (cPCI)
QA/QC	Quality Assurance/Quality Check
RMS	Root Mean Square

Acronym	Definition
ROC	Receiver Operating Characteristics
RTK	Real Time Kinetic
SAGEEP	Symposium for Applied Geophysics for Environmental and Engineering Problems
SERDP	Strategic Environmental Research and Development Program
SLO	San Luis Obispo
SNR	Signal to Noise Ratio
TEM	Transient Electromagnetic
TEMTADS	TEM Towed Array Detection System (NRL/SAIC TEM array)
TOI	Targets Of Interest
USAEC	U.S. Army Environmental Center
USB	Universal Serial Bus
USGS	U. S. Geological Survey
UTM	Universal Transverse Mercator
UXO	Unexploded Ordnance
YPG	Yuma Proving Ground

Figures

Figure 2.1: Functional block diagram of the MetalMapper of the showing the major components of the overall system.....	4
Figure 2.2: Photos showing the MetalMapper antenna array together with the electronics package and control console (inset). The photo was taken at a demonstration conducted at Aberdeen Proving Grounds (APG) in September, 2008.....	6
Figure 2.3: Time lines for the MetalMapper and related projects.....	7
Figure 2.4: Photos that illustrate the evolution of the MetalMapper from the AOL(1) system deployed at Blossom Pt (2004) to the MetalMapper deployed at San Luis Obispo and Camp Butner.....	8
Figure 2.5: Figure contrasting the difference between single coil and multi-axis coil transmitter illumination[1].....	9
Figure 2.6: MetalMapper receiver locations. All 7 receivers are in the plane of the horizontal transmitter (Z) loop.....	10
Figure 2.7: An MM acquisition block illustrating a bipolar transmitter waveform with 50% duty cycle and a repeat factor (N) of 3. Block periods are operator selectable from 33.333ms to 0.9 s in multiplicative steps of 3.....	10
Figure 3.1: Detection maps derived from the same MetalMapper data set acquired over the Blind Grid at YPG. The data were acquired with a lane spacing of 1m. The average 5MI detection map (left) is similar to the map that would be derived from an EM61 survey. The Split Cube map (right) maps the amplitude of the secondary field of each triaxial cube receiver independently. The result is a detection map with an effective Lane spacing of 13cm. The inset shows the path of the (split) cube receivers.....	19
Figure 5.1: Gantt charts providing time lines and activity breakdowns for 3 MetalMapper demonstrations covered in this report.....	25
Figure 5.2: Target detection map – Blind Grid. MetalMapper demonstration at APG (Sep '08). The “+” symbol denotes the center of a 2m x 2m cell.....	28
Figure 5.3: Principal polarizability transients output from MM/RMP.....	29
Figure 6.1: A small area from each (A & B) of the maps in Figure 3.1 illustrating improved resolution for target detection arising from split cube processing. The profile view (C) is also very useful finding smaller and/or deeper targets that often distort the side lobes of a bigger anomaly.....	34
Figure 6.2: Detection map for the Indirect Fire area of the APG standardized test site. The parameter mapped is the average of vertical secondary field for the 5 inner-most cubes of the MetalMapper receiver array. The “x” symbols mark a target pick.....	36
Figure 6.3: Detection map for the Direct Fire area of the APG standardized test site. The parameter mapped is the average of vertical secondary field for the 5 inner-most cubes of the MetalMapper receiver array. The “x” symbols mark a target pick.....	37
Figure 6.4: Base map of the 11.8-acre study site at Camp San Luis Obispo. The map shows the subdivision of the area into 54 survey blocks (30m x 30m), and 11 sub-areas. Also shown are the target picks based on the MM dynamic survey. Picks marked in green comprise the picks for which ground-truth was supplied to all data processing demonstrators. The blue picks represent targets for which demonstrators submitted a prioritized dig list. The 8 blocks in the rectangular area K6-N7 plus the narrow strip outlined in orange are areas that were excluded from the study for budgetary reasons. ..	38

Figure 6.5: The average principal polarizability curves (red,green,blue) for the 4 targets of principal interest at Camp SLO. These curves were derived from approximately 15 independent static MetalMapper measurements acquired in the free-air (SLO Test Pit), and in the ground (SLO Test Strip). The average curves were used in estimating the target detection threshold to be used at SLO.....	39
Figure 6.6: Detection plots for the 4 targets of interest at SLO. The curves represent the peak response as a function of depth below the antenna platform for two target attitudes: vertical, and horizontal. The MM platform when deployed on skids is 21 cm above ground level. The dashed vertical green line has been placed at a depth of 66cm (45cm below ground level). The noise floor (shown correctly for the 60mm and 2.36-in targets is around 0.1 nT/s).....	40
Figure 6.7: A “Pseudo” split cube map consisting of 60 calibration profiles acquired over a period of approximately 3 weeks. Each profile has been offset from its neighbor by 1m. There are 10 calibration targets (rows) at approximately 6m intervals starting a 0m. There are also several spurious “uninvited” targets the most obvious of which is the one that forms the row at about 30m.	41
Figure 6.8: Annotated detection figures for the 2.36-in rocket and the 60mm mortar. The plotted points are average peak amplitudes for the vertical (“x”) and horizontal (“+”) buried targets.....	42
Figure 6.9: Parameter extraction using MM/RMP. The input data are transients (63) acquired during a single static-mode measurement with the MetalMapper. The outputs are the principal polarizability rate transients, target position, and target attitude.....	43
Figure 6.10: Summary of the theory for approximating the response of a small conducting and permeable object with a point dipole.....	44
Figure 6.11: Flow diagram showing the how dipole modeling is implemented in MM/RMP. The problem is divided into two estimation problems, one non-linear, the other linear. These problems are solved for each time gate in the MetalMapper data.	45
Figure 6.12: Two examples from the YPG Calibration Grid illustrating the difference between Type 0 and Type 1 tracking of the principal polarizability curves. This behavior only occurs with targets exhibiting a cross-over in the curves suggesting that the targets apparent attitude changes with time.....	46
Figure 6.13: Example of principal polarizability curves for a clutter object. The object does not exhibit the symmetry characteristic of UXO. This object is buried in the Calibration Grid (cell D2) at APG.	50
Figure 6.14: A categorized scatter plot made with two scalar parameters extracted from data taken over the calibration grid at APG.	50
Figure 6.15: A scatter plot showing the correlation between target weight and object size. The symbols are colored (red,green,blue) to indicate 3 categories of munitions (small, medium, and large).	51
Figure 6.16: Flow diagram for discrimination as applied to detected targets from the Blind Grid at YPG (June 2008).....	52
Figure 6.17: A flow diagram of the discrimination process as it was applied for the discrimination stage of the APG demonstration. The discrimination decisions were, for the most part, founded on rule-based decisions and library curve matching wherein a multiplicative penalty function based on data quality was applied to the decision metrics.	53

Figure 6.18: Scatter plot illustrating the relationship between static data SNR and Fit. The 3 rd dimension is a figure-of-merit metric M_a that can be used as a penalty function for discrimination of data sets with low SNR and/or low Fit statistic. The data are from the cal lanes at APG. Color has been modulated by M_a .	54
Figure 6.19: Polarizability plots of the 6 ordnance types of interest in the recently reconfigured UXO test area at APG. All 6 are present in the Blind Grid. The 3 types identified with an appended “(DF)” have been seeded in the “Direct Fire” area and likewise type names with an appended “(IF)” have been seeded in the “Indirect Fire” area. The heavy dashed curves represent the (geometric) average of a population of training polarization curves extracted from MetalMapper data acquired over the Calibration Grid at APG.	57
Figure 6.20: A simplified computational flow diagram that shows the process of using library polarizability curves to identify the target “type” of an unknown target. The index i indicates the i^{th} library type. The unknown polarizability curves are matched with each of the (N) “types” in the Target “Type” Library.	58
Figure 6.21: Processing diagram for discrimination with MetalMapper static data sets from SLO.	59
Figure 6.22: Histograms showing the distribution of SNR and Fit statistic for 2492 MM static files acquired at SLO.	60
Figure 6.23: Plots showing the figure of merit functions defined in equation (3-1) for the parameter values in Table 3-1.	61
Figure 6.24: Fit histogram (left) together with the cumulative static data points as a function of the MMRMP Fit statistic.	62
Figure 6.25: Polarizability scatter plots based on ground truth from the training dig (Top – 177 targets) and training data from the test pit and test strip at SLO (67 targets). The vertical bars (green) represent the parameter P_{0E} . Targets with large P_{0E} do not exhibit an axis of symmetry that is generally associated with ordnance items	63
Figure 6.26: Principal polarizability curves for the 4 munitions of primary interest at SLO. Each curve set is derived from an ensemble of 14 static measurements over targets at different depths and orientations. The heavy curves (red/green/blue) are the geometric mean curves computed by taking the geometric mean of their respective ensemble.	64
Figure 6.27: Principal polarizability curves for 2 mortar types: Mortars with fins (and fuses?) exhibit characteristically larger values of P_{0x} and a larger aspect value (P_{0R}).	65
Figure 6.28: ROC curves showing the results of applying ANN and the ANN + Library Curve matching to their respective training sets after training. The type curve library contains 5 types (60mm, 60mmNF, 2.36-in, 81mm, 4.2-in).	71
Figure 6.29: ROC curves furnished by IDA after scoring. Results of applying ANN and the ANN + Library Curve matching to the dig lists are shown. ANN Network 2 was used.	72
Figure 6.30: Categorized “beta” plots overlaid with a contour plot of the ANN only (left) and ANN plus Library Matching (right) decision surface. The decision threshold contour line (dashed yellow).	73
Figure 6.31: Polarizability curves and dig photos for 2 targets in the MM target list. Both targets were classified as “Clutter” with relatively unambiguous scores.	73
Figure 7.1: An index map showing the 53 survey blocks of the SLO study area. The study area was divided into 13 sub-areas. The brown shading is actually survey points. The inset shows the actual survey profiles for a small area. The plotted profiles are on 0.75m centers and represent the track of the MetalMapper survey platform.	76

Figure 7.2: Base map showing the SLO Test Strip. The map on the left shows the strip with the locations of the 59 calibration survey lines plotted in brown. The red numbered symbols indicate the locations of the 10 seeded targets. For reference, the diameter of the symbols is 0.8m.....	80
Figure 7.3: Stacked profiles from the vertical (z) component of the 7 MetalMapper receiver cubes as pass over a buried (horizontal) 60mm target. These profiles were calculated for different profile offsets (x-coordinate) from the target center. For an offset of x=0, cube 0 has the largest peak anomaly. For an offset of 30cm (target is 30cm left of profile), cube 7 has the largest peak anomaly. Cube 7 is located at x=-39cm relative to the center of the receiver array. The target is placed at depth = 51cm, which is the nominal depth of the seeded targets in the SLO test strip plus 21cm to account for the antenna array height (skid-mounted)......	81
Figure 7.4: Variation of relative peak amplitude as a function of profile offset for split cube analysis and for Avg5IZ. The Avg5IZ detection parameter is similar in behavior to that of an EM61.	81
Figure 7.5: Parametric profiles of the Avg5IZ detection scalar for the MetalMapper. The parameter is the cross-track profile offset from the target location. The target is a horizontal 60mm mortar at 51cm depth.....	81
Figure 7.6: Scatter plots suggesting that part of the problem with poor anomaly amplitude repeatability is due to offset. In these scatter plots, the horizontal axis is the cross-axis error between the anomaly peak and the target position. The vertical axis is the observed anomaly relative to its mean.	82
Figure 7.7: Base map upon which has been plotted the location of 25 dynamic calibration lines at APG. The red circle marks the target (shotput) and the inset shows that the envelop of the line tranverse to the direction of motion is less than 10cm.....	83
Figure 7.8: Figure showing one target that went undetected in the MetalMapper dynamic survey. Target 410 is readily discernible on both map and on the profiles. Although it has a broad areal extent indicating a deep target, its amplitude fails to rise above the detection threshold.....	83
Figure 7.9: Photograph of the recovered 60mm “body” associated with SLO target number 410.	84
Figure 7.10: IDA ROC curves for the two discrimination stage target lists submitted in connection with the SLO classification study. The differences in the lists a the result of using different data sets for training the ANN and different versions of the ANN software. In the insets, we have identified the 4 false negative targets that occur beyond the MM threshold. Note that the same 4 targets are involved in both target lists (albeit, in different order).	85
Figure 7.11: Principle polarizability curves for a 37mm projectile. The curves on the left (A) represent the average 6 or 8 curve-sets extracted from data sets observed over 37mm projectiles in the Calibration Lanes at APG. The curves on the right were extracted from static data set SLOStatA00292.tem, the only data set observed over this 37mm target. This target was miss-classified as Clutter.....	86
Figure 7.12: Detection profiles and a segment of the associated split cube detection map for MetalMapper Cued ID target number 1177. The anomalies seem to reflect a shallow target such as the tail booms found (presumably) above the deeper 60mm mortar.	87

Figure 7.13: MM Cued ID No. 1177 and the corresponding dig photo. The target in the hole is a 60mm mortar. The polarizability curves appear to represent the associated tail booms and/or fuse.....	87
Figure 7.14: Polarizability curves and dig results for MM-ID Numbers 1718 and 1782, two of 4 false negatives in both target lists submitted to IDA	88
Figure 7.15: Detection profiles and map segment showing the target MM-ID No 1718, classified incorrectly as clutter (false negative). The spikes and offsets in the individual cube profiles are the result of a problem we had with shorting turns in one of our transmitter loops. The problem was corrected in the early days of the dynamic survey. For reference, the yellow target symbols have a diameter of about 1m. The static data files SLOStatA01715 and SLOStatA02204 were acquired at positions close to 1718. Field notes (for 1715) indicate the presence of a “rocket shaft” on the surface that obviously been moved from its original position. The notes also indicated that 1715 DID NOT correspond with a target pick.....	89
Figure 7.16: Field note describing target near 1715 as a “rocket shaft” (A) together with the polarizability curves for 1715 and a repeat (2204). The polarizability curves both look like rocket parts. These two data sets are within a meter or two of MM-ID 1718.	90
Figure 7.17: Polarizability curves for two 2.36-in “empty” warheads. The target on the left is from the training dig, the one on the left is from the test dig. Although target 1782/1541 was deeper than 954/1260, both targets exhibit similar behavior in the early time.....	91
Figure 7.18: Polarizability curves for MetalMapper static files 1717 and 1718 corresponding to SLO target 1475. The curves are not indicative of a target like the 2.36-in rocket motor shown on the white board. More likely, they characterize the 60mm tail boom that is shown.....	91
Figure 7.19: ROC curves for SLO test results. These curves were generated from ground-truth provided by IDA. However, we used the ranks we generated for the 15 category 4 targets rather than score them as “unnecessary digs”. The ROC curve for List 1 (A) also reflects a minor change to the decision rules that was made after the original List 1 was submitted. This change was applied to List 2 before submission.....	93
Figure 7.20: Depth error histogram for 187 seed targets at SLO.....	94
Figure 7.21: Polar scatter plot showing the errors in the estimation of horizontal position for 187 seed targets at SLO.	95
Figure 7.22: Figure comparing individual (fine lines) and geometric mean principal polarizability curves (heavy red/green/blue curves) corresponding to seed targets acquired on the one hand in free air with the NRL/SAIC MTADs system (top row) and on the other hand acquired in situ at SLO with Geometrics’ MetalMapper. The geometric mean curves derived from the data acquired with the two systems are virtually identical when viewed logarithmically.....	97
Figure 7.23: Scatter plots comparing composite “Betas” or P_0 ’s as acquired from SLO seed target objects with the TEMTADs system in free-air and the MetalMapper system with in situ measurements of the targets as buried at SLO.....	98
Figure 7.24: Polar plot of horizontal platform and target position estimates for the SLO static calibration data points.....	101

Tables

Table 2.1: Table highlighting differences between the MetalMapper (MM) and two competing advanced EMI metal detection technologies.	11
Table 3.1: Global SLO Classification Study Performance Objectives	13
Table 3.2: MetalMapper-Specific Performance Objectives for the SLO Project	14
Table 5.1: Acquisition parameters used during MetalMapper demonstrations	30
Table 6.1: Statistics and min/max values for each of the 3 blind areas at the APG test site.	54
Table 6.2: The 6 targets of interest (TOI) at the APG demonstration site. The “X” designates that targets of the indicated type have been seeded in a particular area.	55
Table 6.3: Parameter values for figure of merit function M_a	61
Table 6.4: Table summarizing the statistics of the 4 MOI’s of interest at SLO. We use this table to define the range of target sizes that may be munitions.	62
Table 6.5: Table of scalar target parameters extracted from static data sets acquired with the MetalMapper.....	66
Table 6.6: TOI Statistics	67
Table 6.7: Clutter statistics	68
Table 6.8: Correlation matrix for the 9 scalar parameters (features) selected for use in discrimination at SLO.	68
Table 6.9: Results of ANN (and other) parameter selection.....	69
Table 7.1: Summary of footprint coverage for the 13 sub-areas comprising the 11.8-acre (4.78 ha) SLO study area. The instrument footprint was assumed to be 0.75m.	75
Table 7.2: Summary statistics for repeated surveys over the 10 targets seeded in the test strip at SLO. All position errors are given in meters. The peak amplitude values are in units of μ T/s. Note that the local Y coordinate is along the survey track. The columns relevant to repeatability performance objectives are highlighted in blue.	77
Table 7.3: Summary statistics for repeated surveys over the 10 targets seeded in the test strip at SLO. All position errors are given in meters. The peak amplitude values are in units of μ T/s. These statistics are based on line by line picking of targets and more extensive editing than those shown in Table 7.2. The columns relevant to repeatability performance objectives are highlighted in blue.	78
Table 7.4: Local coordinates for target locations in the test strip at SLO.	79
Table 7.5: Table comparing TEMTADs “Betas” to “Betas” recovered by MetalMapper for seed targets at SLO. The table shows that we are able to recover primary “Betas” (P0x) with errors less than $\pm 15\%$ which is well under our performance objective.	99
Table 7.6: Table showing dynamic survey productivity at SLO.	100
Table 7.7: Dynamic survey productivity at APG.....	100
Table 7.8: Summary statistics for static repeatability at SLO. The top table section speaks to the ability to repetitively re- position the platform over the same point. The bottom section contains the statistics for the estimates of target position and size.	101
Table 7.9: Static-mode survey productivity at Camp SLO.....	102
Table 7.10: Static-mode survey productivity at APG.....	103
Table 8.1 Cost Model for a MetalMapper Deployment.....	104
Table 8.2: Major components comprising a MetalMapper system.....	105

Executive Summary

The MetalMapper is an advanced time domain electromagnetic (TEM) system for application towards the detection and characterization of UXO. The antenna configuration includes 3 orthogonal transmitter loops and 7 tri-axial receiver loops. The system can be deployed in mapping (or detection configuration) wherein it acquires data along profiles while the antenna platform is in motion. However, the most important benefit of the elaborate antenna configuration is that it permits us to characterize a buried metallic target from measurements at a single spatial point located (approximately) above the target. This system is being commercialized by Geometrics, Inc (San Jose, CA).

In 2008, the MetalMapper was demonstrated at the Standardized UXO Technology Demonstration site located at APG. In 2009 and 2010, the MetalMapper participated in live site demonstrations at the former Camp San Luis Obispo (SLO), and the former Camp Butner. The performance objectives of these demonstrations were to demonstrate the capabilities of the MetalMapper when operating both in its mapping mode (target detection) and in its static mode (cued ID target identification).

The system has a detection “foot print” of approximately 1 m^2 , similar to that of the EM61. In detection mode surveying, the MetalMapper surveyed along parallel profiles with a nominal offset of 0.75m. We acquired data at an average survey speed of less than 0.5m/s in order to maximize data quality. At those speeds our average survey production was slightly more than 1 acre/day.¹ Our detection scores show that at these speeds we can detect all targets down to a depth of 11 times the target diameter. Static mode survey productivity is very much a function of terrain, navigation software, and deployment platform. Over the course of our three full demonstrations (APG, SLO, and Camp Butner), the productivity of the MetalMapper in the static mode doubled from approximately 200 pts/day to over 400 pts/day reflecting improvements both in our navigation software and in our deployment platform.

Our performance improved from one demonstration to the next. We attribute this improvement not to improvements in overall data quality but to improvements in our ability to identify and extract the important discrimination features from our static target data and in an improved understanding of the technology of decision theory and pattern recognition. At APG, for example, we achieved a discrimination score at our operating point of a Probability of Detection (Pd) of approximately 90% at a Probability of False Positive (Pfp) of approximately 10% where the low Pd primarily represented deep targets that were not detected by the MetalMapper.² In contrast, at SLO discrimination scores were based only on detected targets. At SLO, the Geometrics’ discrimination score at the operating point was Pd=98% with a Pfp≈5%. Using the same data, other “Data Processing Demonstrators” generated similar results thus showing that discrimination performance is not tied to a particular discrimination methodology. At Camp Butner, our discrimination scores were good, while those of some other demonstrators were

¹ Sample rate is typically 10 Samples/sec and the MetalMapper survey speed can be easily doubled or tripled with a corresponding diminution of data quality and spatial sample density.

² To preserve the ground truth, the Aberdeen Test Center (ATC) scores provide only a depth range. Most of the targets not detected at APG lay in the depth range “8x to 12x” the object diameter.

nearly perfect. We conclude that the data quality gathered by the instrument is very high, and sufficient to support further work in processing of the targets for discrimination.

The estimated cost of deploying the MetalMapper based on the demonstrations we have conducted is high, 2 or 3 times what it would cost to deploy commercially available systems such as the EM61. These estimated costs are high because our demonstrations were conducted by-and-large with high-cost personnel and we conducted field operations to maximize data quality rather than productivity. We project that the cost per crew day will drop substantially when the MetalMapper is routinely deployed and the labor costs drop. As it is now, the MetalMapper costs approximately \$10K/ha when used in the detection mode and \$20/target when deployed for cued ID. Detection mode productivity is about 0.5 ha/day; however, at normal survey speeds (~1m/s), the detection mode productivity would be 1ha/day. Cued ID mode survey productivity is 300 targets/day.

Higher costs and lower productivity in the detection mode can only be justified when we can demonstrate that through more advanced detection methods the MetalMapper can eliminate many superfluous targets such as small surface clutter. So far, however, we have not developed or applied advanced physics-based target detection principles and therefore we cannot justify any claims of superior target detection performance relative to simpler systems.

The demonstrated advantage of deploying the MetalMapper lies with its ability to discriminate targets and thus to produce a prioritized dig list. With regulatory acceptance, the use of a prioritized dig list would reduce the number of digs by 50% or more (depending on how conservative the dig policy was set). This would result an overall cost savings of 30-40% in the cost of geophysical surveying plus digging. Therefore, the high cost for the deployment of the MetalMapper is justified on the basis that it can substantially reduce the cost of digging. However, routine deployment of the MetalMapper will require not only broad regulatory acceptance of this advanced EMI technology but also that it or other advanced systems be specified for use in upcoming UXO remediation projects.

The MetalMapper is now a commercially available product from Geometrics, Inc (San Jose, CA). Geometrics is able to provide not only the basic hardware, but also the software to support the data interpretation, as well as training and field support.

1. INTRODUCTION

1.1. BACKGROUND

There are millions of acres of land located at formerly used defense sites (FUDS) and military installations closed under the base realignment and closure (BRAC) program. Much of this land has been contaminated with unexploded ordnance (UXO). These lands must be decontaminated and restored before they can revert to civilian use. With present technology, the cost of the decontamination is estimated to be on the order of 10's of billions of dollars. The high cost for decontaminating these sites is driven by the need to visually identify all metal targets detected with current metal detecting technology. However, only a few percent of these targets are actually UXO. Because of the potential danger, these digs must be conducted by explosive ordnance demolition (EOD) technicians resulting in digging costs in excess of \$100/target. At many sites, the target density can exceed 100 targets/acre. Development of technology that can reliably classify metal targets at a cost that is substantially less than the cost to dig can therefore substantially reduce the overall cost for decontaminating these sites by reducing the number of required digs [2].

The MetalMapper is an advanced electromagnetic induction system (EMI) configured for the detection and characterization of UXO. This technology represents a significant departure from existing commercially available EMI technology (e.g., the Geonics EM-61). Although the MetalMapper can be used in the survey or mapping mode for target detection, its most important application is for use as a system for "Cued-ID" target characterization. In the cued ID mode, data are acquired at one or more locations in close proximity to the target. Precision static measurements at these locations permit the calculation of the target characteristics. For isolated targets, a measurement at a single field point suffices. These target characteristics may be used to generate a prioritized dig list that can be used to identify targets that can with high confidence be left in the ground because they are not ordnance.

1.2. OBJECTIVE OF THE DEMONSTRATIONS

The over-arching objective of the demonstrations described in this report is to gain acceptance of MetalMapper system by the UXO community – including regulators. To achieve this objective, we must show by participating in blind demonstrations that the MetalMapper can indeed be used to "reliably" prioritize target lists for digging and thus reduce the number of false positive (i.e., non ordnance) items that need to be identified through excavation.

1.3. REGULATORY DRIVERS

There are no regulatory barriers to applying the technology embodied in advanced EMI systems such as the MetalMapper. Such systems represent an evolution of already well established and accepted EMI systems such as the Geonics EM-61 that are being routinely applied for target detection in UXO. The real problem is to convince the regulators of the reliability of the discrimination information that the MetalMapper can provide. The ESTCP program office (PO) is addressing this issue by conducting a series of blind live-site tests in which promising new technologies such as the MetalMapper are invited to participate. The demonstrations at Camp San Luis Obispo (SLO) and Camp Butner were two of these tests. To gain regulator acceptance, the PO has involved regulators in the site selection and other aspects of the test design.

2. TECHNOLOGY

The MetalMapper was employed in full demonstrations at the Standardized UXO Technology Demonstration site at Aberdeen Proving Ground (APG), at the former Camp San Luis Obispo (SLO), and most recently at the former Camp Butner. A description is given in this section. Further details on this technology are available from reports pertaining to the AOL projects that we cite in section 2.2.

2.1. TECHNOLOGY DESCRIPTION

Geometrics is commercializing an advanced electromagnetic induction (EMI) system for UXO detection and characterization. Called the MetalMapper (MM), the new system draws elements of its design from advanced systems developed by G&G Sciences, Inc (supported by NAVSEA, SERDP, and ESTCP), and by the Lawrence Berkeley Laboratories (LBL) with support from SERDP and ESTCP. A block diagram of the hardware system is shown in Figure 2.1

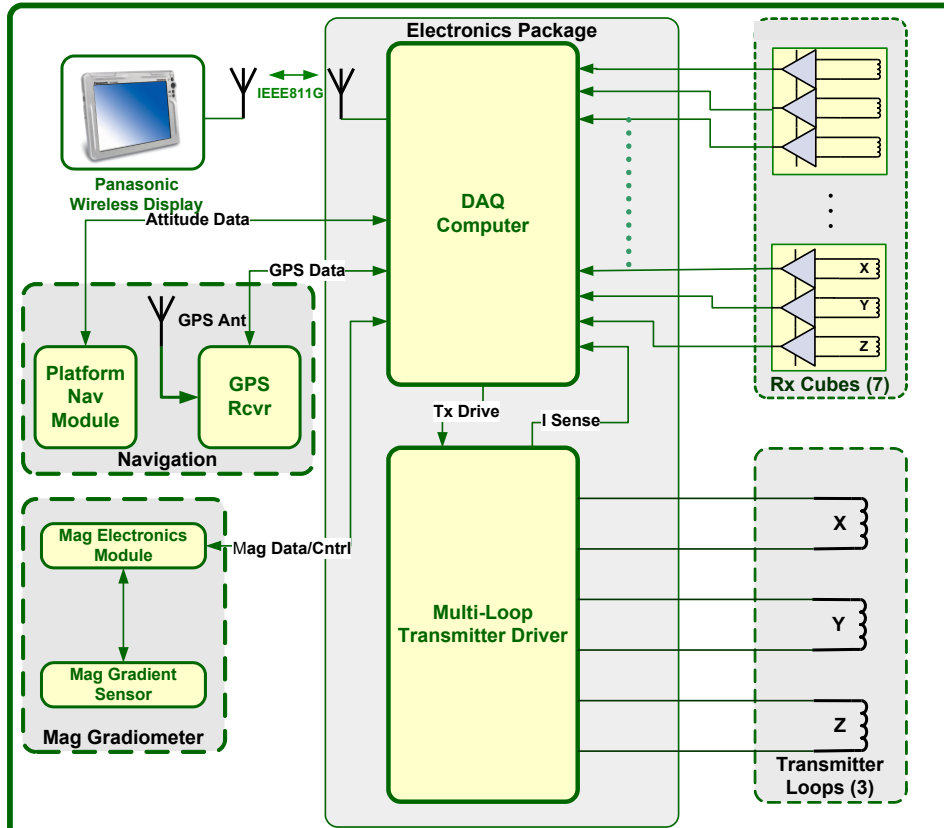


Figure 2.1: Functional block diagram of the MetalMapper of the showing the major components of the overall system.

2.1.1. MetalMapper Hardware

The MetalMapper system is unique and innovative in several respects:

1. **Multiple Transmitter Loops**³: The MM antenna platform includes 3 mutually orthogonal transmitter loops (see photo in Figure 2.2).
2. **3-Axis Sensor Array**⁴: The MM antenna platform includes a spatial array of 7 3-axis receiver antennas (21 independent measurements of the transient secondary magnetic field).
3. **Electronically Switched TEM Transmitter Loop Driver**: The MM system is unique in its ability to drive its transmitter loop array. Under control of the DAQ computer, the output of the transmitter can be directed to any single loop or automatically multiplexed between loops. There is also control of the fundamental waveform period, duty-cycle, and pulse polarity. Typically, however, the loops are driven with a classical bipolar pulse type TEM waveform (i.e., alternating pulse polarity with a 50% duty-cycle). Depending on the survey mode (e.g., Static/Dynamic), the fundamental frequency of transmission can be varied over the range $1.11 \leq f \leq 810$ Hz.

The photo of the MetalMapper shown in Figure 2.2 was taken during the demonstration that we conducted at the standardized UXO test site located at Aberdeen Proving Grounds (APG). During that demonstration, we towed the MetalMapper with a garden tractor in order to acquire dynamic data at a uniform survey speed. The system is normally deployed on skids to minimize platform movement over undulating terrain. The antenna platform including skids and optional wheels weighs approximately 160 lbs (72 Kg) and can be moved by hand when necessary. At APG, cued ID (static) data were also acquired with the antenna platform deployed as a towed system.

We envision the MM Production system to be a system that has a base configuration with two primary options. We will call option 1 a *Mapping* system, and option 2 a *Cued-ID* system. Both systems will employ the same data acquisition system although it will be tailored as needed. The Mapping system will be a subset of the Cued-ID system. It will consist of a single transmitting loop identical to the Z (horizontal) transmitter loop in the Cued-ID system. Moreover, the mapping system will employ the same tri-axial cube sensors but there may be fewer of them. The mapping system is intended to provide maximum ease of use in the field with some cost savings at purchase.

The prototype MetalMapper antenna platform is pictured in Figure 2.2. It has three Tx loops in the Z, Y, and X directions and it contains seven tri-axial sensors inside the Z (bottom) loop. We plan to offer it with optional hard/soft/large/small wheels and it will also be available with a skid/sled. The handle is adjustable in length and height to allow for operator preferences and for either machine-powered or man-powered surveys.

The data acquisition system (DAQ) is built around a commercially available product from National Instruments, NI. The DAQ, EM transmitter, and batteries for the entire system are packaged in an aluminum case that weighs approximately 43 lbs when all four batteries are

³ The 3 transmitter loops is a feature the MM has in common with the AOL2, LBL BUD, and the USGS ALLTEM systems.

⁴ The MM utilizes 3-axis receiver antennas, developed by G&G Sciences for the Navy's AOL system, to acquire measurements of the vector magnetic field. The antennas are small and approximate an observation of the field at a point.

installed. For surveying, the aluminum case can be mounted on a pack frame, on a separate cart such as a hand truck, or on a vehicle such as an ATV or lawn tractor (see Figure 2-2). At SLO we mounted the MetalMapper in a skid connected to the front-end loader of a compact Kabota tractor. This deployment method improved our productivity for static data acquisition since it was easier to precisely locate the MM antenna over a static target site.

In addition to the Panasonic terminal shown in Figure 2.1 A, the instrumentation package includes two external modules that provide RTK GPS and platform attitude (i.e., magnetic heading, pitch, and roll). These modules are connected to the DAQ through serial RS232C ports. The NI data acquisition system is a full-featured PC running Windows XP. It contains disk storage, serial and USB input/output ports, and more. It is interfaced to analog-to-digital converters and to digital input/output devices through its internal PCI bus. It is packaged in an industry standard PXI configuration that is intended for industrial applications. It contains a wireless link that allows the operator console to be remote from the DAQ. The Panasonic Toughbook touch-screen terminal is used as a *dumb* wireless terminal that does no processing. Figure 2.1 B is a functional block diagram of the DAQ instrument package. The DAQ is also interfaced with a GPS unit and a precision attitude module through two RS232 serial ports.

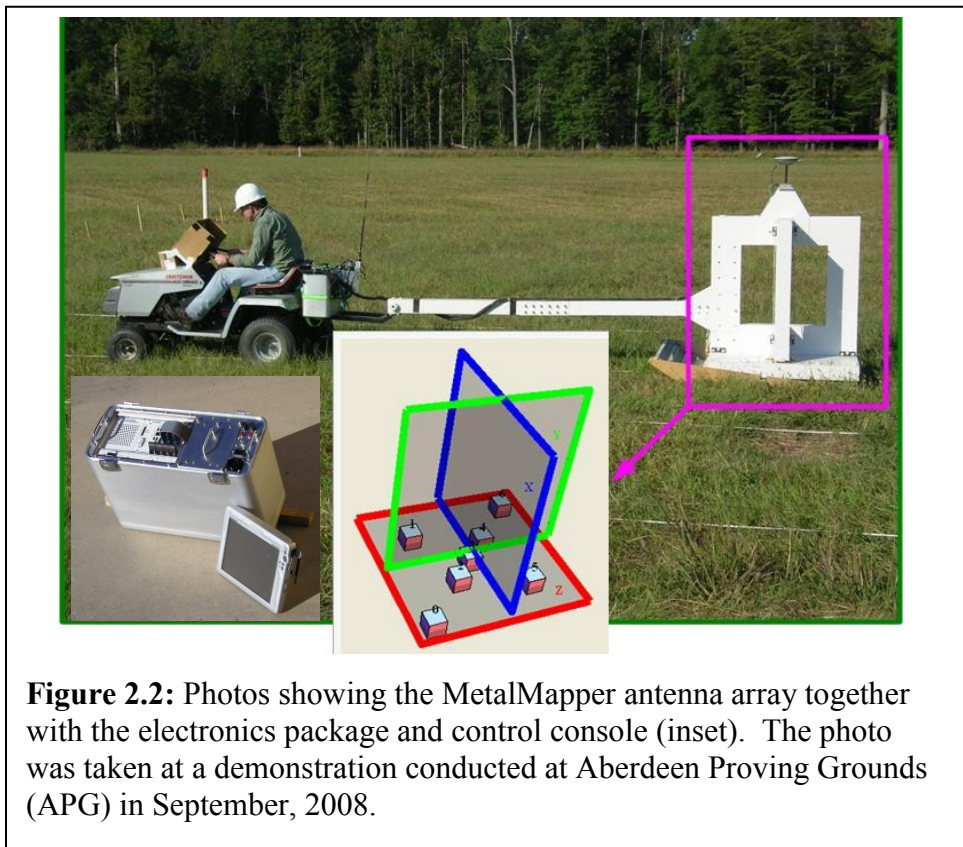
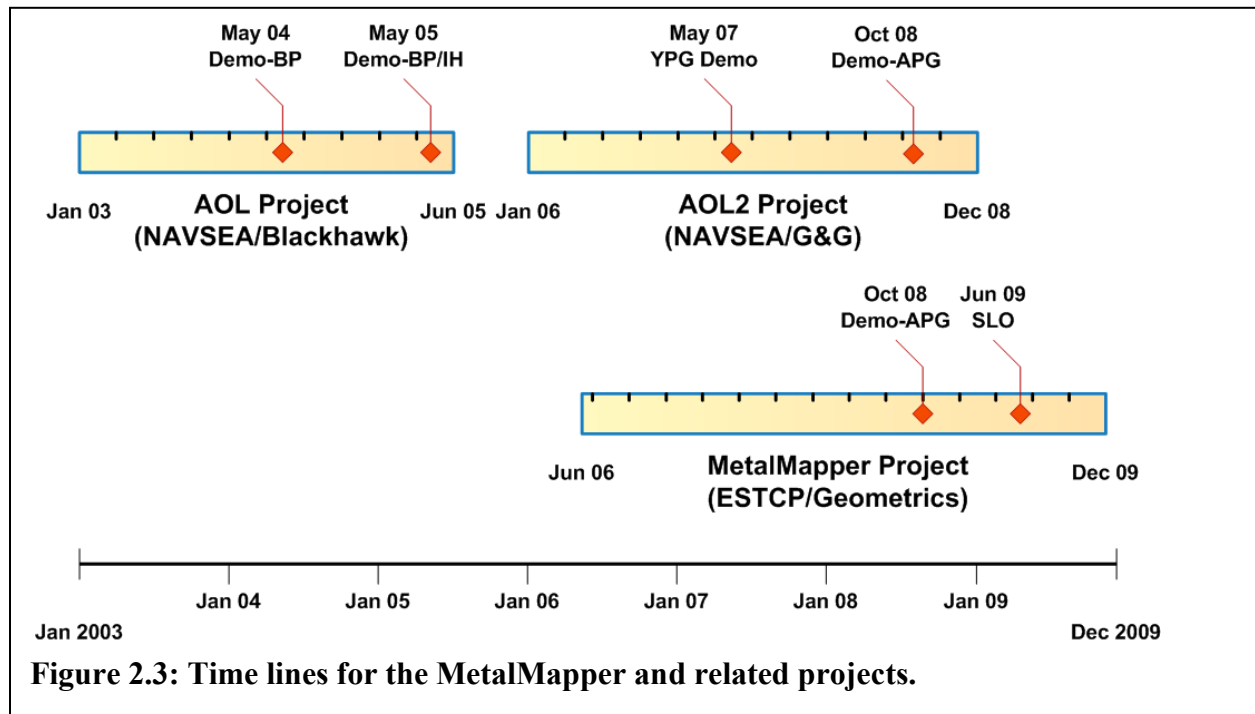


Figure 2.2: Photos showing the MetalMapper antenna array together with the electronics package and control console (inset). The photo was taken at a demonstration conducted at Aberdeen Proving Grounds (APG) in September, 2008.

2.2. TECHNOLOGY DEVELOPMENT

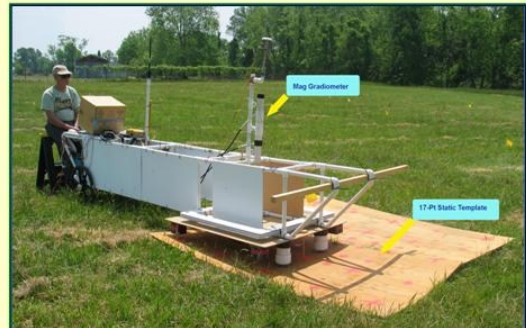


The MetalMapper uses 3rd generation technology whose development began in 2003 with support from NAVFODTECHDIV (Indian Head, MD). A follow-on project, awarded to G&G Sciences (Grand Junction, CO) and supported by NAVFODTECHDIV, continued hardware development but was primarily aimed at the perfection of field procedures and methodology to make deployment practical. And finally, with support from ESTCP, Geometrics (San Jose, CA) undertook to develop the 3rd generation hardware and conduct more comprehensive demonstration in anticipation of commercializing the technology. Figure 2.3 shows the timelines for each of the 3 projects. In the following sections, we summarize the results of the two AOL projects. The system described in section 2.1 has the same capabilities as the AOL2 system together with an improved and much more portable electronics package, improved acquisition software, and an improved antenna platform.

2.2.1. AOL System (2003-2005)

The AOL project (NAVEA Contract No. N00174-03-C-0006) began in 2003 with Blackhawk Geosciences, Inc (Golden, CO) as the lead contractor with G&G Sciences, Inc and Geometrics as sub-contractors. The first AOL system, pictured in Figure 2.4 (upper left), was assembled as a “proof-of-concept” system. It was “uneasily portable”. It is significant, however, that the designs for the tri-axial receiver cube and its preamplifiers, the transmitter, and the data acquisition system and software were completed under this project. In the follow-on (AOL2) project and in the MetalMapper project many incremental improvements were implemented. However, the MetalMapper is based on the same fundamental design and technology elements as its 2 predecessors. Details on the original AOL system can be found in the two demonstration reports submitted by Blackhawk Geosciences, Inc (now Zapata/Blackhawk Division) during the original AOL project [3, 4].

2.2.2. AOL2 System



AOL1 System – Blossom Pt (2004/2005)



AOL2 System – YPG (2007)



MetalMapper System – APG (2008)



Metal Mapper System – SLO (2009)

Figure 2.4: Photos that illustrate the evolution of the MetalMapper from the AOL(1) system deployed at Blossom Pt (2004) to the MetalMapper deployed at San Luis Obispo and Camp Butner.

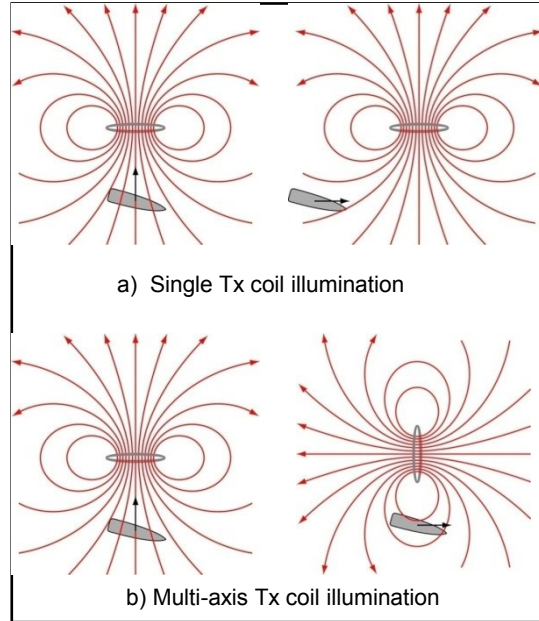
The contract for the AOL2 project was awarded to G&G Sciences (Grand Junction, CO). The objective of the project was to develop procedures and methodologies for practical deployment of the AOL technology by conducting demonstrations at YPG, Indian Head, and APG. However, the achievement of those objectives necessitated the development of a 2nd generation antenna platform, and the development of a new transmitter circuit design that permits the selective energizing of 3 different transmitter loops. The AOL2 system used the same data acquisition hardware that was used with its predecessor. Along with the obvious changes in the hardware, the AOL2 project provided an opportunity to overhaul and improve the data acquisition software. The resulting “AOL2” system is pictured in Figure 2.4 (upper right) during its deployment at the YPG test range. The AOL2 project included 3 demonstrations conducted, respectively, at YPG, Indian Head, and APG. The demonstrations at YPG and APG were conducted at the Standardized UXO Technology Demonstration Sites and therefore were scored by the Aberdeen Test Center (ATC) [5, 6]. Reports describing the activities and results from the 3 demonstrations conducted with the AOL2 system contain details about the system [7, 8, 9].

2.2.3. Other Advanced EM Systems

There are two other advanced EM systems that incorporate some or all of the technology developed as a result of the two AOL projects:

1. Man-Portable Vector (MPV) TEM System (CRREL)
2. TEMTADS (NRL)[1]

Each of these systems has their own unique antenna array. However, the respective instrumentation packages and sensors were assembled by G&G Sciences, Inc and, at a fundamental level, are based on common technology.



2.3. ADVANTAGES AND LIMITATIONS OF THE TECHNOLOGY

The principal advantages of the MetalMapper system over existing commercially available EMI system are two-fold:

1. Multi-Transmitter Target Illumination:

Because the MetalMapper has 3 orthogonal transmitter loops, it is able to illuminate or stimulate a target with primary fields from 3 independent directions from a single spatial field point. In contrast, single transmitter coil systems require the transmitter (and receivers) to be relocated to other field points so that the primary field will stimulate the target from a different direction. The concept is illustrated in Figure 2.5.

2. **Multiple Multi-Axis Receivers:** The MetalMapper employs multiple receivers. The MetalMapper receiver array consists of 7 tri-axial receiver cubes measuring 10cm on a side. With this array, the MetalMapper is able to sample the transient secondary vector field at 7 unique spatial points. The positions of the receiver array are provided in Figure 2.6. The receivers are positioned so that they traverse profiles 13-cm apart along a survey line.

Figure 2.5: Figure contrasting the difference between single coil and multi-axis coil transmitter illumination[1].

The MetalMapper shares two fundamental characteristics with other advanced systems: LBL BUD, USGS ALLTEM, and NRL TEMTADS. All these systems use receiver antenna arrays and transmit multiple fields from a fixed position to energize the target in different directions. The other systems have important similarities with the MetalMapper, yet they also have important differences. These differences serve to distinguish one from another.

In Table 4, we have tabulated a number of important characteristics of 4 advanced EMI systems and highlighted characteristics where there are important differences. These systems differ from the MetalMapper as follows:

1. **Transmitter Waveform:** The MetalMapper and TEMTADS use a conventional 50 percent duty-cycle bipolar waveform (see Figure 2.7). By contrast, the BUD system employs a half-sine bipolar transmitter waveform with a duty-cycle of about 25%. The ALLTEM system employs a triangular waveform. The advantage of the conventional waveform is that it approximates the measurement of the impulse response of the target. The ALLTEM (triangular current waveform), approximates measurement of the step response of the target. And BUD's half-sine transmitter waveform, a pulse width on the order of 350 μ s, approximates a response to equal and opposite sign impulses separated by about 350 μ s. It is significant that the BUD system is operated at a base frequency of 270Hz and the resulting transient is only measured out to approximately 1300 μ s after the turn-off of the 350 μ s transmitter pulse. Both the BUD and ALLTEM systems operate at a fixed base frequency (270Hz, and 90 Hz, respectively). Unlike the MetalMapper and TEMTADS, which can be operated any one of a range of user-selectable base frequencies, the BUD system requires hardware modifications to be operated at a different frequency.

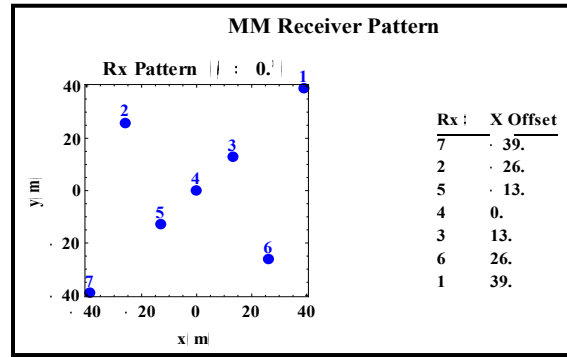


Figure 2.6: MetalMapper receiver locations. All 7 receivers are in the plane of the horizontal transmitter (Z) loop.

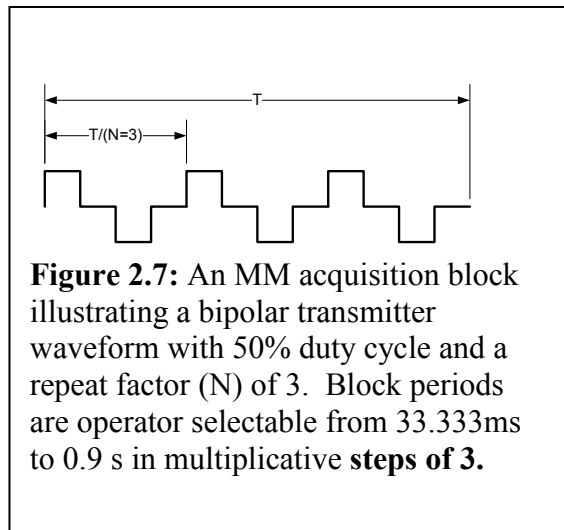


Figure 2.7: An MM acquisition block illustrating a bipolar transmitter waveform with 50% duty cycle and a repeat factor (N) of 3. Block periods are operator selectable from 33.333ms to 0.9 s in multiplicative **steps of 3**.

Table 2.1: Table highlighting differences between the MetalMapper (MM) and two competing advanced EMI metal detection technologies.

		MM	BUD	ALLTEM	TEMTADS
Tx	Multi-Axis	3	3	3	25
	Waveform	Conventional	Half-sine	Triangle	Conventional
	Programmable	Yes	No	Yes	Yes
	Moment	~120	600	504	24
	Base Frequency	Variable (30,90,270)	270	90	Variable (30,90,270)
Rx	Receiver Loops	21	16	10	25
	Multi-Axis Rx	7	0	0	0
	Differential Rx	0	8	7	0

- Transmitted field geometry:** The MetalMapper, ALLTEM, and BUD use three transmitting loops⁵: a Z-axis located at ground level, and two horizontal axis loops just above. For a target exactly beneath the center of the array, the three transmitted B fields are perfectly orthogonal. TEMTADS uses an array of 25 transmitter loops, each 35 cm square, spaced on a 40 cm grid. The target is illuminated in different directions depending on the geometry between a particular transmitting loop and the target. If nine or sixteen transmitting loops are sufficiently close to the target to cause a measurable target response, the target will be illuminated in nine or sixteen independent directions.
- Receivers** – All systems employ multiple dB/dt receiver loops. The difference in the system is in the receiver organization. The MetalMapper uses seven 3-component receivers that measure an approximation of the **vector** dB/dt at each of the seven points. By contrast, the ALLTEM and BUD systems use pairs of receiver loops that are geometrically null-coupled to the primary field. ALLTEM requires this null coupling fundamentally – it is a ‘primary-subtraction’ method. BUD implemented this null coupling to improve receiver performance. One advantage of using receiver loop pairs is that they can reduce common-mode noise (i.e. uniform B-field noise). A disadvantage is that these receiver pairs sense a finite difference field that usually is reduced in amplitude. TEMTADS uses twenty-five receiving loops, each 25 cm square, oriented in the vertical (Z) direction. Using small tri-axial receivers arrayed in a horizontal plane near the ground, as in the MetalMapper, maximizes the signal and provides horizontal field components. These components are very useful for near-surface (< 0.5m) and medium ($0.5 \leq z \leq 1.0$ m) depth targets and often have larger field magnitudes than the vertical component. Further, they sense field direction that can be used to assist the user in field operations. They are less useful, giving a smaller signal, for targets deeper than 1m, but none of the systems reliably detect smaller targets deeper than 1m.

⁵ Although both BUD and ALLTEM, in some cases, use a balanced pair of transmitting loops, the effect is the same as discussed here so an imperfect comparison is made for the purpose of a general description.

The MetalMapper, BUD, and ALLTEM have been designed to detect and characterize targets within a radius of approximately 1m from the center of the horizontal (vertical axis) transmitter. The TEMTADS array is 2m on a side overall. Experiments we have conducted together with our experience in the field with the system demonstrate that the MetalMapper will sometimes detect targets located at lateral distances up to 2m. Therefore, in areas of high target density we can predict that the performance in the discrimination stage will degrade due to the presence of interfering anomalies. This is a likely explanation for the degradation in MetalMapper performance between the Blind Grid and the Indirect/Direct Fire areas at APG. In the case of both fire areas, the target density was often quite high and frequently anomalies were closer than 2m.

In both the YPG and APG demonstrations we have deployed the MetalMapper as a vehicular-towed system with the tow-vehicle being a small tractor. However, the system was designed so that it can also be deployed as a human-powered cart. As a human-powered cart the MetalMapper has limitations similar to but perhaps more severe (due to greater weight) than those that apply to more conventional cart systems such as the EM61 MkII. At SLO, we again deployed the MetalMapper as on the front end loader of a tractor for both dynamic mode and static mode surveys. Our experience at Aberdeen taught us that a vehicular powered system has significant advantages compared with human-powered systems any time that the terrain permits the use of a suitable tow vehicle. At SLO, we used a better tractor in order to improve maneuverability. That tractor had four wheel drive to handle difficult terrain and it has the ability to lift the cart to allow short-radius turns. Its front end loader allowed for rapid positioning of the array over the target.

3. PERFORMANCE OBJECTIVES

We have conducted three full demonstrations (APG, SLO, Camp Butner). The objectives we outlined and explained in the APG demonstration plan are basically a subset of those we have listed here from our SLO demonstration plan. To avoid duplication, therefore, we include here only the objectives from the SLO demonstration plan. In section 7 of this report, we will use results from the APG demonstration where appropriate to demonstrate that we have been able to meet our performance objectives for both demonstrations. Those performance results from APG also serve as a sort of benchmark against which we can measure similar performance at SLO.

The ESTCP Study Plan (Section 3.0 Performance Objectives, Table 3.1) lists and describes seven quantitative objectives for the classification study at SLO. We have duplicated that table here for convenience as Table 3.1. In addition to those objectives, we included a few additional performance objectives shown in Table 3.2 that either supplement or expand the objectives in Table 3.1.

Table 3.1: Global SLO Classification Study Performance Objectives

Performance Objective	Metric	Data Required	Success Criteria
Data Collection Objectives			
Complete coverage of the demonstration site	Percentage of valid points Gaps in survey coverage	• Mapped survey data	No more than 1% of data points have spurious sensor or GPS readings. No coverage gap larger than 75 cm
Repeatability of calibration strip measurements	Amplitude of EM anomaly Measured target locations	• Twice-daily calibration strip survey data	Amplitudes $\pm 15\%$ Down-track location ± 25 cm
Detection of all munitions of interest	Percent detected of seeded items	• Location of seeded items • Anomaly List	At least 98% of seeded items detected
Analysis and Classification Objectives			
Maximize correct classification of munitions	Number of targets-of-interest retained.	• Prioritized anomaly lists • Scoring reports from IDA	Approach correctly classifies all targets-of-interest

Maximize correct classification of non-munitions	Number of false alarms eliminated.	<ul style="list-style-type: none"> Prioritized anomaly lists Scoring reports from IDA 	Reduction of false alarms by > 30% while retaining all targets of interest
Specification of no-dig threshold	Probability of correct classification and number of false alarms at demonstrator operating point.	<ul style="list-style-type: none"> Demonstrator - specified threshold Scoring reports from IDA 	Threshold specified by the demonstrator to achieve criteria above
Minimize number of anomalies that cannot be analyzed	Number of anomalies that must be classified as “Unable to Analyze.”	<ul style="list-style-type: none"> Demonstrator target parameters 	Reliable target parameters can be estimated for > 90% of anomalies on each sensor’s detection list.
Correct estimation of target parameters	Accuracy of estimated target parameters.	<ul style="list-style-type: none"> Demonstrator target parameters Results of intrusive investigation 	$\beta_s \pm 20\%$ $X, Y < 15 \text{ cm } (1\sigma)$ $Z < 10 \text{ cm } (1\sigma)$ size $\pm 20\%$

Table 3.2: MetalMapper-Specific Performance Objectives for the SLO Project

Performance Objective	Metric	Data Requirements	Success Criteria
Quantitative Performance Objectives			
Dynamic Mode Survey Productivity	Area surveyed per day	Field production log	>1.2 acre/day @ 0.75m Lane spacing
Repeatability of parameter estimation	Recovered target parameters	Daily calibrations over canonical target (sphere)	$\pm 10\%$ on $\text{RMS}(P_0)$
Static-Mode Survey Productivity	Static Pts/day	Daily production logs	Pts >30/hr or Pts >200/day

3.1. OBJECTIVE: COMPLETE COVERAGE OF DEMONSTRATION SITE

The reliability of the survey data depends on the extent of coverage of the site. This objective concerns the ability of the demonstrator to completely survey the site and obtain valid data.

3.1.1. Metric

The metrics for this objective are the percentage of valid data points and the maximum coverage gap in the final, mapped data.

3.1.2. Data Requirements

A mapped data file will be used to judge the success of this objective.

3.1.3. Success Criteria

This objective will be considered to be met if at least 99% of the mapped data points have valid sensor and GPS readings and if the maximum coverage gap is no more than 75 cm.

3.2. OBJECTIVE: REPEATABILITY OF CALIBRATION STRIP MEASUREMENTS

The reliability of the survey data also depends on the proper functioning of the survey equipment. This objective concerns the twice-daily confirmation of sensor system performance.

3.2.1. Metric

The metrics for this objective are the amplitude and down-track position of the maxima obtained from each of the twice-daily surveys of the calibration strip.

3.2.2. Data Requirements

The survey data will be used to judge this objective.

3.2.3. Success Criteria

This objective will be considered to be met if the measured amplitudes for each object are within 15% of the mean and the down-track position of the anomaly is within 25 cm of the known location.

3.3. OBJECTIVE: DETECTION OF ALL ITEMS OF INTEREST

Quality data should lead to a high probability of detecting the munitions of interest at the site.

3.3.1. Metric

The metric for this objective is the percentage of seed items that are detected using the specified anomaly selection threshold.

3.3.2. Data Requirements

Each demonstrator will prepare an anomaly list. IDA personnel will score the detection probability of the seeded items.

3.3.3. Success Criteria

The objective will be considered to be met if at least 98% of the seeded items are detected.

3.4. OBJECTIVE: MAXIMIZE CORRECT CLASSIFICATION OF MUNITIONS

This is one of the two primary measures of the effectiveness of the classification approach. By collecting high-quality data and analyzing those data with advanced parameter estimation and classification algorithms we expect to be able to classify the targets with high efficiency. This objective concerns the component of the classification problem that involves correct classification of items-of-interest.

3.4.1. Metric

The metric for this objective is the number of items on the master anomaly list that can be correctly classified as munitions by each classification approach.

3.4.2. Data Requirements

Each demonstrator will prepare a prioritized dig list for the targets on the master anomaly list. IDA personnel will use their scoring algorithms to assess the results.

3.4.3. Success Criteria

The objective will be considered to be met if all of the items-of-interest are correctly labeled as munitions on the prioritized anomaly list.

3.5. OBJECTIVE: MAXIMIZE CORRECT CLASSIFICATION OF NON-MUNITIONS

This is the second of the two primary measures of the effectiveness of the classification approach. By collecting high-quality data and analyzing those data with advanced parameter estimation and classification algorithms we expect to be able to classify the targets with high efficiency. This objective concerns the component of the classification problem that involves false alarm reduction.

3.5.1. Metric

The metric for this objective is the number of items-of-interest on the master dig list that can be correctly classified as non-munitions by each classification approach.

3.5.2. Data Requirements

Each demonstrator will prepare a prioritized dig list for the targets on the master anomaly list. IDA personnel will use their scoring algorithms to assess the results.

3.5.3. Success Criteria

The objective will be considered to be met if more than 30% of the non-munitions items can be correctly labeled as non-munitions while retaining all of the targets-of-interest on the dig list.

3.6. OBJECTIVE: SPECIFICATION OF NO-DIG THRESHOLD

In a retrospective analysis as will be performed in this demonstration, it is possible to tell the true classification capabilities of a classification procedure based solely on the prioritized dig list submitted by each demonstrator. In a real-world scenario, all targets may not be dug so the success of the approach will depend on the ability of an analyst to accurately specify their dig/no-dig threshold.

3.6.1. Metric

The probability of correct classification, P_{class} , and number of false alarms, N_{fa} , at the demonstrator-specified threshold are the metrics for this objective.

3.6.2. Data Requirements

Each demonstrator will prepare a ranked anomaly list with a dig/no-dig threshold indicated. IDA personnel will use their scoring algorithms to assess the results.

3.6.3. Success Criteria

The objective will be considered to be met if more than 30% of the non-munitions items can be correctly labeled as non-munitions while retaining all of the targets-of-interest at the demonstrator-specified threshold.

3.7. OBJECTIVE: MINIMIZE NUMBER OF ANOMALIES THAT CANNOT BE ANALYZED

Anomalies for which reliable parameters cannot be estimated cannot be classified by the classifier. These anomalies must be placed in the dig category and reduce the effectiveness of the classification process.

3.7.1. Metric

The number of anomalies for which reliable parameters cannot be estimated is the metric for this objective.

3.7.2. Data Requirements

Each demonstrator that estimates target parameters will provide a list of all parameters as part of their results submission along with a list of those anomalies for which parameters could not be reliably estimated.

3.7.3. Success Criteria

The objective will be considered to be met if reliable parameters can be estimated for > 90% of the anomalies on each sensor anomaly list.

3.8. OBJECTIVE: CORRECT ESTIMATION OF TARGET PARAMETERS

This objective measures the accuracy of the target parameters that are estimated in the first phase of the analysis. Successful classification is only possible if the input features are internally consistent. The obvious way to satisfy this condition is to estimate the various target parameters accurately.

3.8.1. Metric

Accuracy of estimation of target parameters is the metric for this objective.

3.8.2. Data Requirements

Each demonstrator that estimates target parameters will provide a list of all parameters as part of their results submission. IDA analysts will compare these estimated parameters to those measured during the intrusive investigation and determined via subsequent in-air measurements.

3.8.3. Success Criteria

The objective will be considered to be met if the estimated β s are within $\pm 20\%$, the estimated X, Y locations are within 15 cm (1σ), the estimated depths are within 10 cm (1σ), and the estimated size is within $\pm 20\%$.

3.9. OBJECTIVE: DYNAMIC-MODE SURVEY PRODUCTIVITY

Operating in a vehicle-towed configuration, we surveyed the entire test area with the MetalMapper operating in its dynamic acquisition mode using a lane spacing of 0.75m and a survey speed of 0.5m/s (30m/min). Our objective was to complete the dynamic survey at a rate of 1 acre per day or more.

The reviewers of this plan will no doubt note that we propose to perform our dynamic data collection with 0.75m lane spacing. On the face of it, therefore, it appears that we are ignoring

the overall performance goal stated in 5 of having no survey gaps greater than 0.75m. However, the MetalMapper antenna array contains 7 tri-axial receiver cubes positioned so that each receiver cube tracks independent parallel profiles with an offset of 13cm. Therefore, the data from a single profile acquired with the MetalMapper can be split into 7 profiles covering a cross-track swathe of 0.92m for the purposes of generating a detection map. The detection maps in Figure 3.1 were derived from the same MetalMapper data acquired over the Blind Grid at YPG in June 2008. The area was surveyed with a lane spacing of 1m. The map on the left was compiled by averaging a measure⁶ of the secondary field amplitude of cube receivers 2 through 6 (see Figure 3.1) and thus simulates a map that might be compiled from an EM-61 (1m x 1m) acquiring data with 1m lane spacing. The map on the right was compiled by splitting the cube receivers into separate profiles and again mapping the amplitude of the secondary magnetic field. The inset to the Split Cube map shows the survey tracks followed by each of the individual cubes. Note the there are noticeable gaps between groups of 7 survey tracks. These gaps are representative of the theoretical 16cm gap due to the fact that our survey was conducted with 1m (nominal) profiles while the swathe coverage of the MetalMapper antenna array is 92cm. When viewed in this context (i.e., Split Cube map coverage), our survey with 0.75m lane spacing easily meets the stated performance objective for data gaps.

⁶ We use a composite time gate representing an average of the gates spanning the interval $100 \leq t \leq 900 \mu\text{s}$.

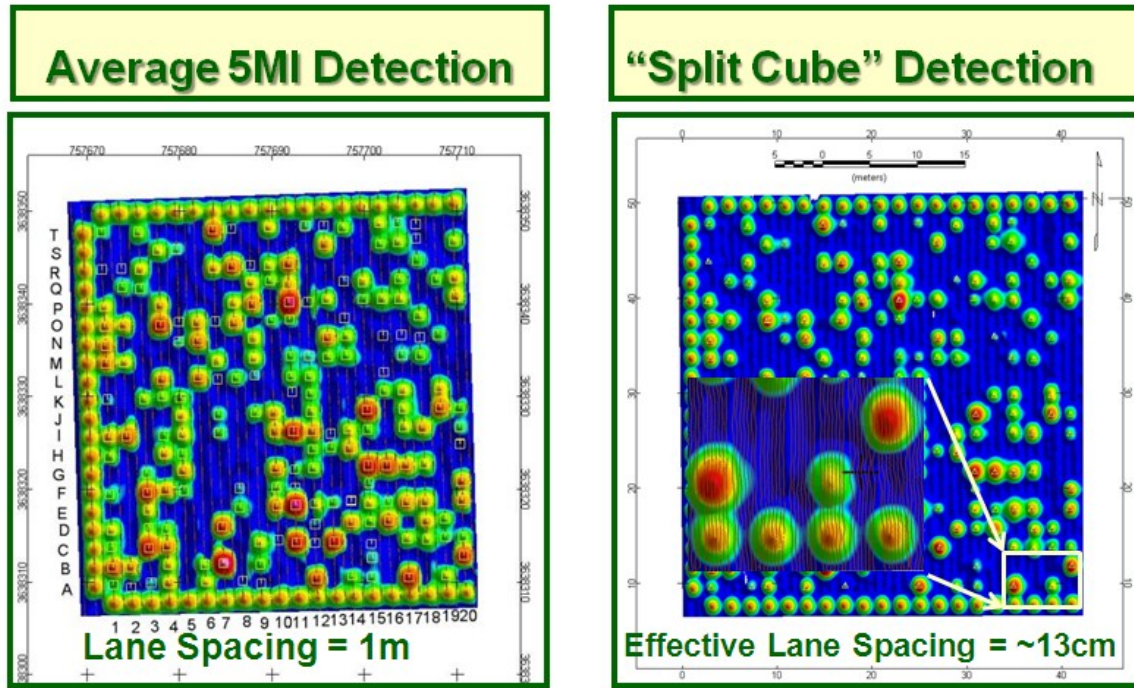


Figure 3.1: Detection maps derived from the same MetalMapper data set acquired over the Blind Grid at YPG. The data were acquired with a lane spacing of 1m. The average 5MI detection map (left) is similar to the map that would be derived from an EM61 survey. The Split Cube map (right) maps the amplitude of the secondary field of each triaxial cube receiver independently. The result is a detection map with an effective Lane spacing of 13cm. The inset shows the path of the (split) cube receivers

3.9.1. Metric

The metric for dynamic-mode survey productivity will be the average area covered per day.

3.9.2. Data Requirements

The data files representing dynamic survey lines or static points are tagged with both a time and a date. The file name itself is constructed of a unique text identifier to which is appended a 5-digit index that increments for each successive data file. We index those files daily on a spreadsheet which provides us with a production log that documents the time it takes to cover any particular segment of the survey area as well as the total time for completing the survey. Thus, we will be able to estimate both an average productivity for the whole survey and on a daily basis.

3.9.3. Success Criterion

At APG, we surveyed approximately 1.2 acres/day in the dynamic mode. The conditions at SLO will be different and perhaps more challenging due to the topography at SLO. We are planning modifications in our antenna platform, our tow vehicle, our navigation software, and our field procedure with the goal of exceeding the productivity we achieved at APG.

3.10. OBJECTIVE: REPEATABILITY OF PARAMETER ESTIMATION

This objective speaks to our goal to demonstrate that the response of MetalMapper system remains stable over time. It includes stability of the MetalMapper hardware as well as stability and robustness of parameter-extraction processing. This objective is slightly different from the global objective “Correct Estimation of Target Parameters” (Section 3.7) in that our static calibration measurements re-acquire the same target each time. So this MetalMapper-specific objective supplements that global objective.

3.10.1. Metric

We use a robust parameter extracted from the principal polarizability transients (the RMS value of the three integrated polarizability transients (P_{0x} , P_{0y} , P_{0z}) estimated with our physics-based model. This measure of system response is independent of minor variations in platform attitude and position relative to a calibration target.

3.10.2. Data Requirements

The required data will be acquired as part of routine dynamic-mode and static-mode measurements over the Calibration Strip established at SLO. As indicated in the ESTCP Study Plan one of the seeded targets will be a sphere.⁷ Our QC plan requires us to visit the calibration strip two or more times per day. In addition, we will have the ground-truth from the training data set (the first 5 30m x 30m blocks excavated) and, eventually, from the rest of our survey. Using the available ground-truth we will develop retrospective statistics relating to the reproducibility of the principal polarizability transients for each of the target types of interest.

3.10.3. Success Criteria

We have set our success criterion to $\pm 10\%$ based on our experience from repeated static calibrations at YPG and at APG. In the case of the latter, we acquired a total of 35 static calibration measurements on our calibration target over a period of 18 days. The mean and standard deviations for the $\text{RMS}(P_0)$ extracted for those measurements was $2369 \pm 85 \text{ cm}^3$. Thus, the success criterion allows almost 3 standard deviations assuming that the variations in the parameter are Gaussian. Therefore we expect that all of our calibration measurements will fall within this range.

3.11. OBJECTIVE: STATIC-MODE SURVEY PRODUCTIVITY

When operating in the *Cued ID* or static survey mode our objective is to maximize the number of sites visited per day consistent with maintaining data quality. Data quality is primarily a function of two variables in the field. First it is necessary to position the center of the antenna platform as nearly as possible to the desired target point. Second, data quality depends on the stacking time—longer stacking time means better data. Improving productivity therefore means decreasing both the time for target reacquisition and minimizing the stacking time.

⁷ We assume that the sphere will be located at a depth that provides good SNR ($>40\text{dB}$). If not, we will implant our own “Calibration Sphere.”

3.11.1. Metric

For static-mode surveys, the metric will be *targets/hr.*⁸

3.11.2. Data Requirements

The data required for measuring productivity comes directly from our field notes and our index of data files. The data files representing dynamic survey lines or static points are tagged with both a time and a date. The file name itself is constructed of a unique text identifier to which is appended a 5-digit index that increments for each successive data file. We index those files daily on a spreadsheet. Measuring productivity over any period of time is simply a matter of counting the number of (good) dynamic or static data files over a given period of time.

3.11.3. Success Criteria

Our criterion for success for productivity in the static survey mode is 30 targets/hr. We achieved that level of production both at Yuma and at APG. With the modifications we plan in our procedures and navigation software as well as in the way we mount the antenna platform to survey vehicle, we hope to improve on the productivity we achieved in our other demonstrations.

⁸ We are adopting an hourly rate rather than a daily rate here because field days can vary significantly because of site access.

4. SITE DESCRIPTION

Over a one-year period, we have conducted demonstrations at the Standardized UXO Technology Demonstration Sites located at Yuma Proving Ground (YPG), Aberdeen Proving Ground (APG), the Former Camp San Luis Obispo in California and most recently at Camp Butner in North Carolina. This Final Report focuses mostly on the results of YPG, APG, and SLO, since the Camp Butner analysis was ongoing at the time this was written.

4.1. SITE SELECTION

4.1.1. Standardized Demonstration Sites (APG and YPG)

The UXO test sites at APG [11] and YPG [12] were specifically developed by the U.S. Army Environmental Command (USAEC) for the testing of all technology relating to the detection and classification of UXO. Each of the sites include an area for calibration and training (Calibration Lanes) where various types of inert ordnance of interest have been seeded and the ground truth is made available to demonstrators. These sites include other areas that have been seeded wherein no ground-truth is provided. Two types of demonstration areas are provided: 1) grid; and 2) open field areas.

1. **Blind Grid:** In the blind grid, targets have been seeded at the centers of a uniform 40x40 grid with grid centers at 2m intervals. Not all grid cells are occupied. The blind grids are designed to test an instrument's sensitivity for target detection and discrimination under conditions where interference from adjacent targets (located a minimum of 2m away) is minimized. Moreover, in a seeded cell the nominal (X-Y) location of the target is known. We conducted demonstrations and were scored by the ATC over the Blind Grids at both YPG and APG.
2. **Open Field Areas:** In these areas, the targets are seeded randomly with the same standard targets seeded in the Calibration Lanes and the Blind Grid. The MetalMapper did not demonstrate over the Open Field area at YPG. In 2008 and before our demonstration, the Open Field Area at APG was reconfigured into two smaller areas designated as the "Direct Fire" (DF) area and the "Indirect Fire" (IF) area. Considerable effort was made to seed the areas with munition types (and clutter) that simulate the spatial distribution and target depths found in direct and indirect fire impact zones. It is significant, that the new areas at APG were seeded with only 3 types of munitions. The DF was seeded with 25mm M792 (including brass casing), 37mm M63M1 projectile, and 105mm M456 (HEAT) projectiles. The IF was seeded with 60mm M49A3 and 81mm M374 mortar rounds, and the 105mm M60 artillery projectile.

4.1.2. Camp San Luis Obispo (SLO)

The former camp San Luis Obispo, located near San Luis Obispo, CA was carefully selected by the ESTCP program office as the demonstration site for classification study to be conducted in 2009. The MetalMapper was one of 3 advanced electromagnetic systems to participate in that study. The 12-acre study area is a former mortar and 2.36-in bazooka rocket range. There site contains 4 munitions types of primary interest: 2.36-in rockets, 60mm mortars, 81mm mortars, and 4.2-in mortars. In contrast with the standardized UXO test areas at YPG and APG, the SLO demonstration area is situated on a hill and as such presents a significant challenge for survey in both detection or survey mode acquisition and in cued ID or static mode acquisition.

4.2. SITE HISTORY

The standardized sites program is a multi-agency undertaking being coordinated by the U.S. Army Environmental Command with support provided by the Aberdeen Test Center (ATC), and the Army Corps of Engineers. Funding is provided by the Army Environmental Quality Technology Program (EQTC), ESTCP and SERDP. The standardized sites at APG and YPG were constructed at two major army testing facilities at either end of the country. Each of these installations has a long history of use for the testing and evaluation of military munitions. Each site meets other requirements for siting of a UXO Demonstration area that have been enumerated in a “handbook” that outlines the procedure for selecting and constructing such demonstration sites [13]. The sites at APG and YPG were completed in 2002. Since then each site has hosted dozens of partial or full demonstrations [14].⁹ The APG site has been reconfigured 3 times, most recently in 2008. The YPG site is currently on its second reconfiguration.

Camp San Luis Obispo was established in 1928 as a facility for the California National Guard. It was used extensively during World War II as a training facility and again during the Korean conflict. The facility was inactive after the Korean conflict. At the present time, approximately half of the original land has been transferred to Cal Poly State University and Cuesta College and the other half has been retained by the California National Guard.

4.3. SITE GEOLOGY

4.3.1. Standardized Sites

The soil at the APG site consists of low permeability poorly drained soil with relatively high moisture content (20%-30%). Topography is “flat” with maximum slopes of 1%-2%. The soil at YPG is typical alluvium characteristic of basin and range pediment to be found throughout the desert southwest. The soil has low moisture content (typically < 7%). Moisture increases with depth and moisture levels greater than 3% are only found at depths greater than 1m. These soils have relatively low magnetite content with volume magnetic susceptibilities typically around 100 SI. As with the APG, the general topography is flat.

4.3.2. San Luis Obispo

In contrast to the standardized test sites, topographic relief over the 12-acre SLO site is in excess of 200 ft with slopes sometimes exceeding 15%. Soil textures and thicknesses range widely. Thick sandy alluvium is found adjacent to washes and drainage channels. Thin to thick mountain terrace soils typically overlay crystalline metamorphic bedrock and are usually comprised of sandy to silty loam with a thin veneer of silty clay near the surface. Moisture levels vary seasonally. At the time of our demonstration (May-June 2009), the soils were very dry.

⁹ A partial demonstration is here defined as conducting a minimal survey consisting of the Calibration Lanes plus the Blind Grid. A full demonstration requires a survey over the Open Field area.

4.4. MUNITIONS CONTAMINATION

4.4.1. Standardized Sites

The YPG site has been seeded with a diverse set of inert munitions ranging from 20mm M55 projectiles on the small end to 155mm M483A1 projectiles on the large end. The munitions types include a number of common submunitions. The calibration lanes have also been seeded with a few (uncommon) non-munition targets such as shot puts, steel disks, and shorted conducting loops. A complete description of munitions types to be found at YPG and APG can be found by following appropriate links located on Standardized UXO Technology Demonstration Program web site [10].

The APG demonstration site was reconfigured in early 2008. As part of that reconfiguration, the open field was sub-divided into a “Direct Fire” (DF) area, and an “Indirect Fire” (IF) area. Each of these areas has been seeded with 3 munitions types that are appropriate to the type of range they simulate. The DF contains 3 types of direct fire munitions: a) 25mm rounds; b) 37mm projectiles; and c) 105mm HEAT projectiles. Similarly, the IF contains 3 types of indirect fire munitions: a) 60mm mortars; b) 81mm mortars; and c) 105mm artillery projectiles. The newly reconfigured Blind Grid at APG contains 6 munitions types, the 3 types seeded in the DF area and the 3 types seeded in the IF area. The Calibration Lanes at APG contain more than the 6 munition types seeded in the Blind Grid, DF, and IF. However, the target density has been significantly decreased in an effort to reduce interference between targets. So there are fewer targets overall and the main emphasis has been to provide demonstrators with opportunities to characterize the 6 munition types that have been buried in the Blind Grid, the IF, and the DF.

4.4.2. San Luis Obispo

The San Luis Obispo site is a live site. A preliminary dig of two small 50 ft x 50 ft grids in the 12-acre area of interest revealed 4 types of munitions: 2.36-in rockets, 60mm mortars, 81mm mortars, and 4.2-in mortars.

5. TEST DESIGN

5.1. CONCEPTUAL EXPERIMENTAL DESIGN

Each of the field demonstrations was conducted in 3 phases:

1. Dynamic-mode survey for target detection
2. Static-mode survey for “Cued-ID” discrimination
3. Post-acquisition analysis

The Gantt charts in Figure 5.1 and 5.2 provide time-lines for each of the demonstrations and also serve as an outline for the various activities involved.

5.1.1. Target Detection (Mapping Survey)

In the first phase of each field demonstration, the MetalMapper is operated in its dynamic (mapping) mode in order to generate a detection map. In its dynamic mode, only the horizontal (Z) transmitter loop is energized. Data are acquired along a series of parallel profiles. These data are compiled into a detection map wherein the mapped parameter indicates a peak centered directly over any metallic target within range. Peaks are chosen (i.e. “detected”) either manually using the computer mouse or automatically using an automatic peak detector that operates on a data grid. In all cases where an automatic peak detector is employed, it is necessary to edit the resulting peaks in order to remove or “merge” multiple target picks on the same anomaly. The resulting edited target list is used during the next (Cued ID) phase of the demonstration.

5.1.2. Cued ID (Static Survey)

The target list generated from the mapping survey “cued” (sequenced) so that each target can be efficiently reacquired.

Reacquisition requires that the antenna platform be nominally centered over the anomaly of interest. Once a target is reacquired, the MetalMapper is activated to acquire a single static data set. For static data acquisition, each of the three transmitter loops is energized while data

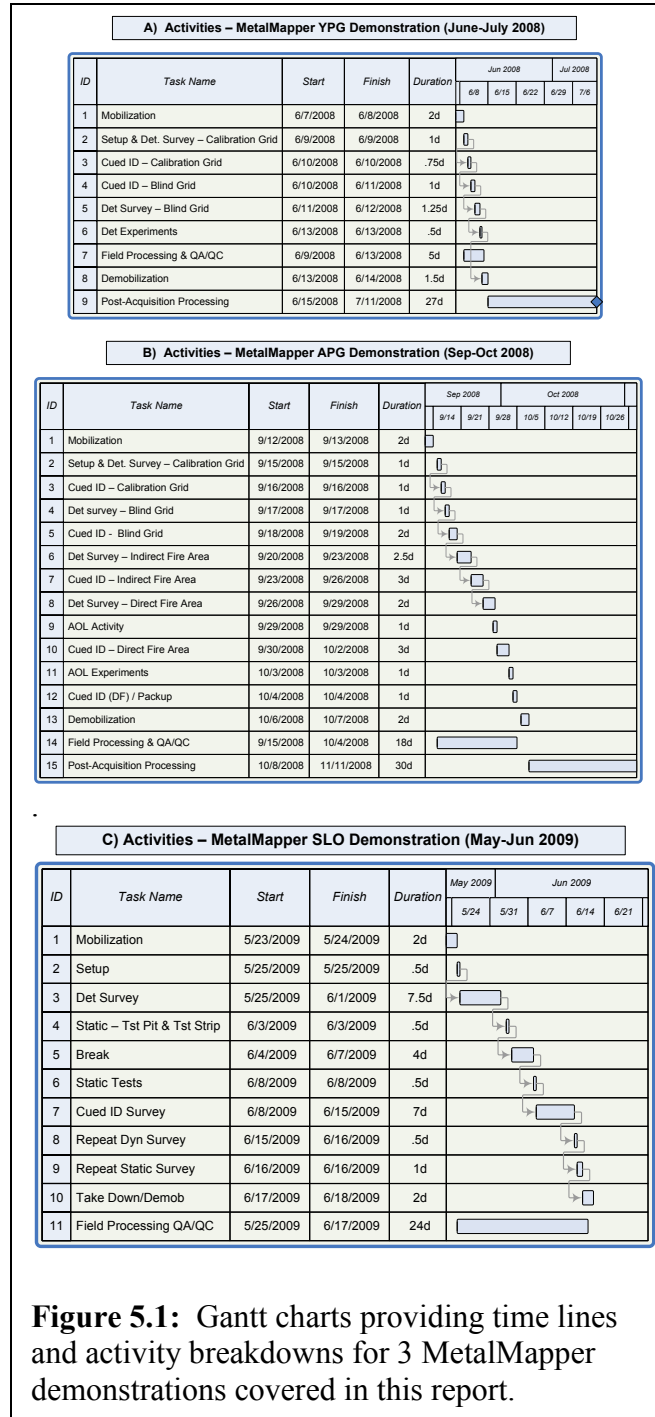


Figure 5.1: Gantt charts providing time lines and activity breakdowns for 3 MetalMapper demonstrations covered in this report.

transients are measured from the 7 triaxial cube receivers (21 transients). Because the antenna platform is motionless, each receiver transient can be repetitively stacked over many cycles of the transmitter thus significantly reducing incoherent random noise. A complete data set that includes the results from energizing each of the three transmitter loops takes 25-50 seconds depending on the stacking parameter.

5.1.3. Post-Acquisition Analysis

Preliminary data processing for the purpose of generating detection maps and for QA/QC purposes is carried out throughout the course of the field demonstration. However, most of the data processing required to assemble a target list for scoring occurs after the field activities have been completed (post-acquisition). Post-acquisition processing includes the following steps:

1. **Target Association:** Static data points are associated with a particular target site on the basis of proximity. When there is more than one static data point associated with a particular target site, a decision is made as to whether the files are associated with a single target or multiple targets.
2. **Feature Selection:** Statistical analyses including scatter plots, principal component analysis, and trial and error are performed to help select a set of features (*feature vector*) associated with the targets that we think best identifies the targets of interest from clutter.
3. **Library Matching:** Generate a library of “type” polarization curves representing the munitions types known to exist in the area of interest. Match the polarization curves extracted from each of the unknown targets with those in the type library. Select the target type with the best matching score.
4. **Neural Network Training:** Using feature vectors corresponding to targets for which ground truth is available (e.g., from free-air static measurements, test lanes and instrument verification strips, and training digs), train a neural network.
5. **Neural Network:** Apply feature vectors from each target in the test set (i.e., all unclassified targets) to the neural network trained in step 4. The neural network output represents the primary classifier.
6. **Target List Assembly:** In the final processing step, the results from both library matching and neural network analysis are merged to form a single classification score. Visual QC is performed on the prioritized list using cataloged polarization curves.

5.2. SITE PREPARATION

The standardized UXO sites have been “sanitized” and then seeded with inert munitions according to procedures reported in a handbook assembled as part of the Standardized UXO Demonstration Program [13]. Unlike the standardized test sites at APG and YPG, Camp San Luis Obispo is a live site. Preliminary investigations included a magnetometer transect survey and an EMI survey over a larger area to assist in selecting a smaller site suitable for the discrimination study. In addition, 2 small 50ft x 50ft grids were dug in order to identify the munition types that would likely be encountered during the SLO study. Finally, additional munitions of the type expected at SLO were seeded in order to improve the ratio of targets-of-interest to clutter items.

5.3. SYSTEM SPECIFICATION

The prototype MetalMapper conforms to our present vision of the *Cued ID* system. Since the Mapping system is a subset of that, we are also able to use the Cued-ID system for mapping.

5.3.1. Antenna Platform

The MetalMapper's three transmitting loops are positioned as follows:

- Z transmitter (coil axis vertical): 1m x 1m, center is ~15cm above ground level. The center of the Z loop is taken to be the local origin of coordinates for the cart.
- Y transmitter (coil axis horizontal in direction of travel): 1m x 1m, centered 0.56m above the origin.
- X transmitter (coil axis horizontal, clockwise from Y): 0.98m x 0.98m, centered 0.56m above the origin.

The MetalMapper's seven receivers are positioned as shown in Figure 2.6. Note that the seven receivers traverse profiles that are 13cm apart in the cross-track (x) dimension.

5.3.2. Signals and Timing

The MM system is, by design, a very flexible system for acquisition of time domain EM (TEM) data. It is beyond the scope of this document to fully describe that flexibility. Simply stated, data are acquired in time blocks that consist of a fixed number of transmitter cycle “Repeats”. Both the period (T) and the repeat factor (N) are operator selectable and are varied in multiplicative factors of 3.¹⁰ The MM also averages an operator-specified number of acquisition blocks (NStack) together before the acquired data are saved to disk.

The transmitter is energized with a bipolar waveform as illustrated in Figure 2.7. Therefore the alternating decay transients received during the off times must be synchronously rectified and stacked (averaged). Decay transients in each acquisition block are first rectified and stacked and then averaged with other the resulting stacked transients from successive acquisition blocks (assuming the operator has selected NStack greater than one). The resulting data are saved as a *data point*. All GPS readings received during the acquisition period are averaged together. If no GPS readings are acquired during that period, the most current GPS position and the platform attitude angles (magnetic heading, pitch, and roll) are used. GPS points are non-synchronously acquired at 20 points per second. Therefore, depending on relative timing, GPS coordinates that are stored with the data are either the most recent fix, or the average of fixes received during the data point collection interval. By varying the block period (T) and the repeat factor (R) settings, we can set the sample rate as high as 30 data-points/sec or as low as desired (e.g. ~1 data-point per minute typically for static data points).

Timing of all EM signals including transmitter switching and receiver sampling is controlled by hardware that is under the control of the acquisition software. The MetalMapper collects data in

¹⁰ The options for N (3,9,27,...) and T = (0.0333, 0.1, 0.3, 0.9s) are such that the resulting fundamental transmitter frequency and its odd harmonics do not coincide with 60Hz and its odd harmonics.

a so-called *double-buffered* mode meaning that the data samples from a previously collected data point are processed and stored concurrently with acquisition of the next data point. If computer processing cannot maintain pace, one or more succeeding data points are skipped. For normal surveying activities, data points are rarely skipped.

The MM has two data acquisition modes: Single-Point-Mode and Continuous-Mode. Data collection and processing is the same for either mode. In single-point mode the system collects a data point as previously described and then terminates acquisition. The data are stored as a single data point in the output data file. In continuous mode, the system initiates collection of a new data point concurrently with completion of the previous data point and continues until the operator intervenes. All of the data points are stored to the same output data file.

Once acquired, the decay transients in a data point are decimated into a set of logarithmically spaced time gates. Received signals are sampled at a rate of 250 KS/s. After initiating turn-off of the transmitter, the system initiates a time delay (e.g., 100 μ s) determined by the *HoldOff* parameter. Thereafter, digital samples falling within a specific time gate are averaged and become the value of the signal for that time gate. The widths of the gates are specified by the *GateWidth* parameter. Gate width is specified as a percentage. A gate width parameter of 10%, for example, will generate a gate of width 60 μ s for a delay time of 600 μ s. The minimum gate width is one data sample (4 μ s).

5.3.3. Data Acquisition: Dynamic Data

To collect dynamic data, the MM is operated in Continuous mode and all data from a single survey line are stored in a single file

5.3.4. Post-Acquisition Data Processing: Dynamic Data

Data are stored as binary formatted files. The processing software includes the capability to export the data to a Geosoft Oasis Montaj data base and/or to text files. For dynamic surveys, Oasis Montaj is used for display, QC, map compilation, etc.

As we indicated in Section 3 of this report, we follow a two-step approach to target characterization. The first step is target detection and for that we conduct a dynamic survey. Using a custom Geosoft eXecutable (GX), the data from the dynamic survey are imported into a Geosoft data base (GDB). Other custom GX's have been developed to process the transient data to a point where they can be further processed and displayed using standard capabilities within the Geosoft Montaj software package. The end products of the post-acquisition processing of the dynamic data are target detection maps and profiles and a list of detected targets along with their respective X-Y coordinates. In Figure 5.2, we show the detection

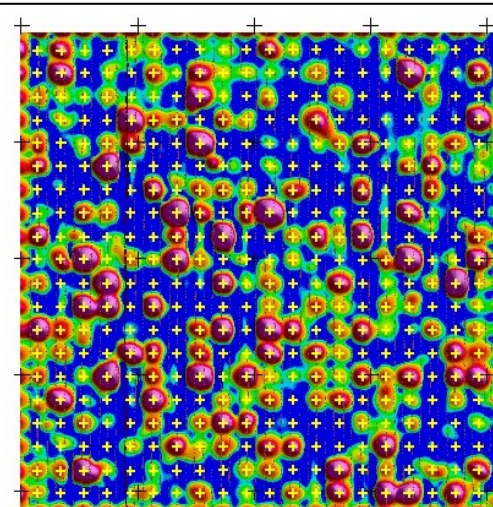


Figure 5.2: Target detection map – Blind Grid. MetalMapper demonstration at APG (Sep '08). The “+” symbol denotes the center of a 2m x 2m cell.

map that we generated from dynamic data acquired over the Blind Grid at APG.

5.3.5. Post-Acquisition Processing: Static Data

Static data points are acquired with the MetalMapper platform located over each of the targets identified using the dynamic data as described above. These data files are processed with our physics-based modeling program MM/RMP to extract target-specific parameters. An example of the resulting polarizability plot is shown in Figure 5.3.

5.4. CALIBRATION ACTIVITIES

Calibration checks of the MetalMapper system were performed at least two times per day as part of our routine QA/QC procedure. At YPG and APG, these checks were conducted over a calibration sphere (“CalBall”) buried in an area having low background response. At SLO, the dynamic calibration was performed over the Calibration Strip. A check on the static measurement was performed using a steel sphere located in the calibration pit. The calibration procedure is enumerated below:

1. Acquire a static background data set over a designated “background” point (typically a designated point at the beginning/end of the Calibration Strip). Acquisition parameters are set at values for static (*Cued ID*) data acquisition (section 5.5, Table 7).
2. Acquire dynamic data over calibration profile in reciprocal directions using our standard dynamic survey acquisition parameters (see Section 5.5).
3. Acquire a static data set with the antenna platform centered over a designated Calibration Target.¹¹

The calibration procedure provides all the data required to perform a variety of QA/QC checks that document that the instrument is functioning correctly. Moreover, the resulting data will be used to establish the long-term stability of the instrument response.

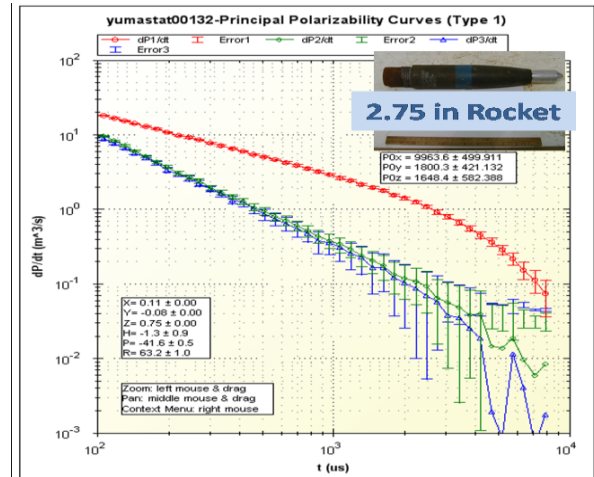


Figure 5.3: Principal polarizability transients output from MM/RMP.

¹¹ We use a steel sphere buried in an area of low background. At YPG and APG, the Calibration Sphere was used for both static and dynamic calibration. At SLO, we used the Test Strip for dynamic calibration. A steel sphere located in the Test Pit at SLO was used for static calibrations.

5.5. DATA COLLECTION

The MetalMapper DAQ has two modes of data collection, *dynamic* and *static*. Data collected in dynamic mode results in data files containing many data samples. Generally speaking, dynamic mode data are collected while the antenna platform is in motion.¹² Static mode data collection is employed for *Cued ID* surveys. As its name implies, the antenna platform remains static or motionless during the period of data acquisition. Depending on the acquisition parameters (i.e., sample period, and stacking parameter) it can take 10's of seconds to complete a static measurement. The results of the static measurement are written into a binary data file containing only a single data point representing the average (stacked) result usually over 10's or even 100's of repetitions of the transmitter's base frequency. In Table 5.1 below, we tabulate the acquisition parameters that we used during the bulk of the demonstration. The 5 shaded columns relate to parameters that can be set by the operator. Those 5 parameters relate to more universally understood acquisition parameters such as base frequency, transient decay length, and sample period/rate. We will describe the following in terms of the more familiar unshaded columns. These parameters were chosen with the benefit of some experimentation over the course of our demonstrations at YPG and APG in 2008. At SLO, we decided to acquire our static data with 8,333 μ s decay transients based on the premise that the improved data quality arising from stacking 3 times more transients was preferable to acquiring poorer quality transients over an extended time bandwidth (8,333 μ s versus 25,000 μ s). Note that the Sample Period shown in the table is for the stack constant shown – for static data, the sample period can be adjusted as desired by choosing a different stack constant. At YPG and APG we used a stack constant of 20 resulting in a sample period of 54 seconds. At SLO, we chose a stack constant of 10 because most targets were shallow and, in general, the signal-to-noise ratio was always high.

Table 5.1: Acquisition parameters used during MetalMapper demonstrations

Mode	Hold-Off Time (us)	Block Period (s)	Rep Fctr	Dec Fctr (%)	Stk Const	Base Freq (Hz)	Decay Time (us)	No. Gates	Sample Period (s)	Sample Rate (S/s)
Dynamic	50	0.1	27	5	1	270	926	58	0.1	10
Static	50	0.9	27	10	10/20	30	8333	50	27/54	N/A

YPG Demonstration

The objective of the YPG demonstration was to assess our readiness to conduct a full demonstration at APG later that year. Consequently, we only allocated 5 field days to the effort and confined our survey activities to the Calibration Grid and Blind Grid areas (see Figure 5.1A). These activities included both dynamic and cued ID surveys and allowed us to submit the Detection Stage and Discrimination Stage target lists required by the ATC as a condition of access to the site.

¹² We also use dynamic-mode data collection when we want to study noise statistics for statically acquired data.

APG Demonstration

The demonstration at APG was our first full demonstration. Both standardized demonstration sites (APG and YPG) are operated under the same rules. And therefore, we were required to survey the Calibration Lanes and the Blind Grid. In any case, these surveys were necessary and desirable because the APG site had been reconfigured earlier in 2008 and the reconfiguration reduced the targets of interest to 6. In addition to the Blind Grid, we also surveyed the newly configured “Indirect Fire” and “Direct Fire” areas. These two areas each cover approximately 1 ha and are located within the confines of the former “Open Field” area. For budgetary reasons, we did not survey the remainder of the Open Field (now referred to as the “Legacy” area).

SLO Demonstration

We surveyed the entire 11.8 acre study area at SLO with the MetalMapper operating in detection mode. Using maps from these data, we selected 2178 targets for cued ID measurements. We also repeated cued ID measurements over 314 of these targets based on inversion results that indicated that the horizontal offset of these targets was greater than 0.4m. During post-acquisition processing, we were able to reduce the number of target picks that we submitted to the program office for the following reasons:

1. **Target Detection Threshold Adjustment:** The SLO dynamic survey was conducted using two different platform deployment methods: wheel-mounted, and skid-mounted. The antenna height above ground level for wheel-mounted deployment was 8cm higher than for skid-mounted deployment. The detection threshold was originally set for the wheel-mounted deployment and was not changed when we reverted to skid-mounted deployment. When we adjusted the target detection threshold upward for areas surveyed, we were able to remove approximately 300 targets from our target list.
2. **Removal of Targets Falling within Defined Areas:** At the direction of the program office, all targets falling within the two defined areas were removed: a) Vehicle Only Area; and b) Vehicle Access Road. These areas and the targets falling within them were removed in order to reduce the total number of targets to be dug for validation.
3. **Target Merges:** We had several requests from the IDA to examine target groups in order to determine whether they related to a single buried item or multiple buried items. Moreover, our own post-acquisition analysis identified other target groups. This processing allowed us to merge a number of closely spaced target picks into a single pick with 2 or more associated MM static data files. There were 314 repeated measurements that fall in this class. But there were also double picks (i.e., 2 peaks on the same anomaly) and picks on the same anomaly at the boundary of adjacent sub-areas.
4. **Targets Picks with No Associated MM Static File:** There were 21 targets on the detection list that we submitted to the program office with no associated MM static file. With one exception, these targets were targets near their associated detection thresholds. They are present as a result of the need to re-grid the dynamic survey and re-pick the targets after IDA noted a systematic offset bias between the location of our target picks and the location of seeded targets. After some investigation, we found that the bias was the result of a bug in the GX that computed the slope correction.

We ended up submitting a detection target list containing a total of 1638 target picks. We were able to associate at least one MM static file with 1617 picks.

5.5 VALIDATION

The YPG and APG test sites are seeded sites that have been constructed and reconfigured from time to time using protocols that have been documented by ATC [13]. Each demonstrator is required to submit target lists for both detection and discrimination. In conformance with the ATC protocol, we have submitted target lists for those areas surveyed with the MetalMapper at both YPG and APG. ATC has issued formal scoring reports for both of those submissions [15, 16].

Camp SLO is a live site. Detected items have been dug by Parsons, Inc under contract with the ESTCP. Parsons utilized standard procedures for digging UXO live sites. In addition, the position, depth, approximate attitude, and a photograph of the resulting target found were recorded. The results of the first 5 30m x 30m survey blocks were provided to all data processing demonstrators for use as training data. The remainder of the dig results were held in confidence by the program officer and IDA and used for the purpose of scoring discrimination target lists prepared by the demonstrators according to protocols described in a scoring memorandum prepared by the IDA and distributed to the demonstrators [16].

6. DATA ANALYSIS AND PRODUCTS

6.1. PREPROCESSING

6.1.1. Dynamic Survey Data

The dynamic survey data consists of parallel profiles acquired with 0.75m offsets. Each profile is recorded to a separate binary data file. From these data, we will compile detection parameter maps of the surveyed area or sub-area. The detection map is based on the magnitude of the secondary fields measured at each of the 7 tri-axial receiver sensors. The following processing steps, accomplished using Geosoft Oasis Montaj (OM), are required:

1. MetalMapper data are recorded as binary files. These data are imported directly into an OM database where simple editing is performed (e.g., editing line numbers, deselecting duplicate lines, trimming and deleting bad data or stops, etc). All other steps are accomplished from within OM using its standard editing and processing capabilities supplemented where necessary with custom Geosoft Executables (GX's) and Geosoft Scripts (GS's) and Geosoft mathematical expression (EXP) files.
2. Convert Lat/Lon to UTM coordinates
3. Make a true heading channel from the UTM coordinates
4. Edit and filter pitch and roll channels.
5. Compute corrected UTM coordinates according to heading, pitch, and roll.
6. Compute detector gate values for each of the 21 receiver channels. The detector gate value is the value of the recorded transient integrated optionally with an exponential weighting function over a selected time interval.
7. Compute transmitted current by gating (windowing) the transmitted current transient.
8. Normalize detector gate values by transmitter current.
9. Select background and remove background (leveling).
10. Generate vector magnitude channels for each of 7 tri-axial receiver cubes
11. Split each profile into 7 separate profiles, corrected for heading and offset distance from the platform measure point (generates 7 parallel profiles with 13cm offsets).
12. Grid the resulting amplitude data.
13. Apply grid smoothing filters if necessary.

Steps 1-9 in the above enumeration constitute preprocessing steps that result in data that can be exported for delivery to the Program Office and/or to analysis demonstrators.

6.1.2. Static Data

As we stated previously, raw static data files are input directly into MM/RMP together with an appropriate background file and a file containing RMS noise estimates for each channel and time gate. What we have heretofore termed “preprocessing” (e.g. location correction, background removal, etc) is performed within MM/RMP during the parameter extraction process. Preprocessed data were only required during the SLO demonstration. During that demonstration, there were several organizations that needed these data to independently prepare discrimination

target lists. We modified MM/RMP so that it can output preprocessed static data files in comma separated values (CSV) format as specified by the program office. The data files were delivered to the program office and subsequently distributed to other demonstrators.

6.2. TARGET SELECTION FOR DETECTION

Our target procedure for target selection has evolved over the course of the three demonstrations covered in this report. We highlight the evolution through examples.

6.2.1. Detection at YPG

At YPG, we only surveyed the Blind Grid. In the Blind Grid at both YPG and APG, we know exactly where to look for a target since whenever a target is present it has been seeded at the nominal center of a 2m x 2m grid square. The detection maps for the Blind Grid at YPG are in Figure 3.1. The left panel of that figure is the detection map that results when the magnitude of the field (averaged over a 900 μ s detection gate) is compiled into a map. The map has a spatial resolution similar to that of a standard EM61. The maps in Figure 3.1 are based on N-S profile measurements on 1m centers and every other profile traverses over the center points of the grid squares. The 2nd panel in Figure 3.1 represents what we call the “split-cube” map wherein we split out the response of each cube into independent profiles. Thus 1 MetalMapper profile generates a set of 7 independent profiles on 13cm centers. One can get a sense of the improved resolution that results from the split cube map by comparing the two panels. In Figure 6.1 we illustrate how the split cube map (6.1B) or profiles can be helpful in detecting a target that is not manifested as a true peak in the EM61-like Avg5IM1 detector (6.1A). At YPG all targets were picked manually from profiles using DIGITPROFOPT.GX available in Oasis Montaj with the standard license. Dynamic data noise thresholds are well below 0.1 μ T/s.

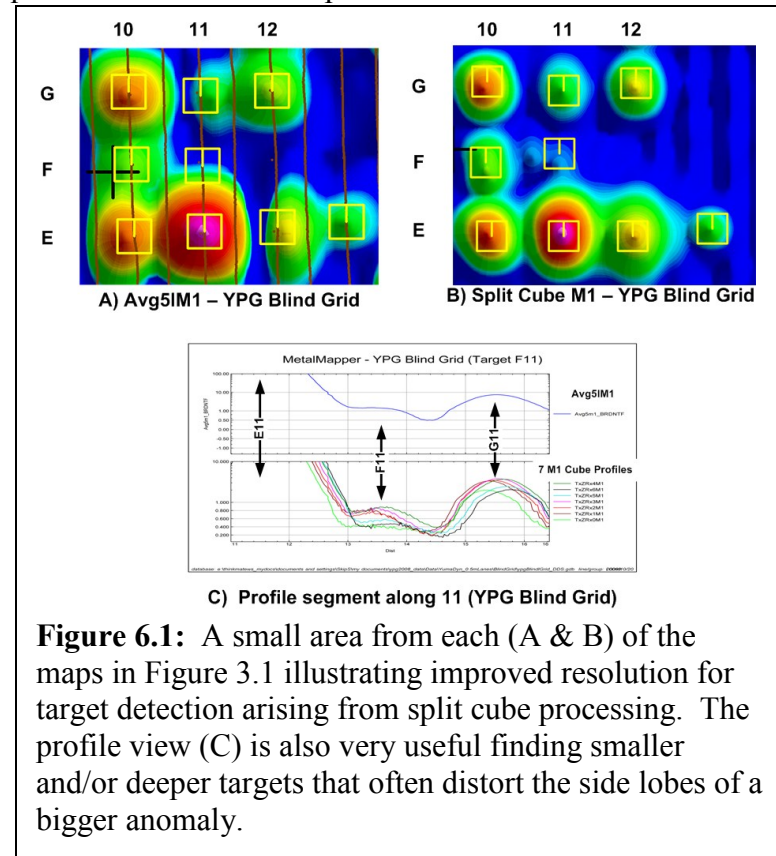


Figure 6.1: A small area from each (A & B) of the maps in Figure 3.1 illustrating improved resolution for target detection arising from split cube processing. The profile view (C) is also very useful finding smaller and/or deeper targets that often distort the side lobes of a bigger anomaly.

We benefitted substantially from the scoring record for the AOL2 system (essentially identical to the MetalMapper) for a similar survey over the Blind Grid at YPG in 2007. In that demonstration, we achieved an overall detection score of 95% with most of the undetected

targets arising from those buried at depths greater than 1m.¹³ Upon revisiting YPG with the MetalMapper, we carefully examined the dynamic profiles over the center of every grid center to make sure that we picked even the slightest low-level distortion if it appeared. As a result, we had a number of target picks with response stage amplitudes on the range $0.1 \leq \text{Response} \leq 1$ nT/s. Although we do not know which of our low-level response stage picks were actually detections, our overall detection score improved from 95% to 100% and our score for deep targets (>1 m) improved from 70% to 85% .

6.2.2. Detection at APG

At APG, we surveyed the blind grid with 0.75m profile offsets rather than with 1m centers as we did at YPG. This change was needed because many of the plastic disks used to mark the corners of the grid squares in both the Calibration and Blind grids were not visible (at YPG, these “Red” disks were mostly visible and provided excellent navigation cues). The Blind Grid detection map at APG is shown in Figure 5.2. Using the grid centers as a guide, we manually examined the composite profile “Avg5M1” (see Figure 6.1C) and the 7 M1 profiles (see Figure 6.1C). If we saw a peak or distortion on the side of a much larger anomaly as in Figure 6.1C we assumed the presence of a target. As with the YPG surveys, the noise level was very low ($<<0.1$ nT/s) all targets were well above that noise level. Our detection score for the Blind Grid was perfect [16].

The Direct Fire (DF) and Indirect Fire (IF) areas at APG are in the Open Field and closely simulate real target areas used for munition types seeded. Each of these areas was surveyed with the MetalMapper using parallel profiles on 0.75m centers. With the exception of an E-W trending drainage ditch in the DF, neither of these areas had any real topographic features to contend with. However, both areas had standing water in some areas that we had to contend with. As a result, there are some places where the line spacing is not as uniform as we would have liked. Detection maps for the two areas are shown in Figure 6.2 and Figure 6.3. In both cases, we manually digitized peaks using Oasis Montaj and DIGITPROFOPT.GX. We examined the profiles for questionable peaks. A strict amplitude threshold was not used. Rather, we examined the profiles on all low-level target prospects and if we had 6 or 7 cubes responding, we picked the peak.

6.2.3. Detection at Camp SLO

Target detection at SLO was managed in a completely different manner than we have described for the previous 2 demonstrations. Guidance from the ESTCP demonstration plan for the SLO Classification Study required that all targets be picked on the basis of anomaly threshold. The applicable detection threshold was to be determined by studying the predicted and measured response for the 4 principal targets of interest (TOI) at SLO, which are the 60mm/81mm/4.2-in mortars plus the 2.36-in (bazooka) rocket. We were asked to set our detection threshold based on the predicted response of the smallest of the 4 TOI when placed in its least favorable orientation (horizontal) when buried at a depth of interest of 45cm below ground.

¹³ Our ATC score was subsequently confirmed independently by IDA with the comment that all undetected ordnance items were deeper than 11X.

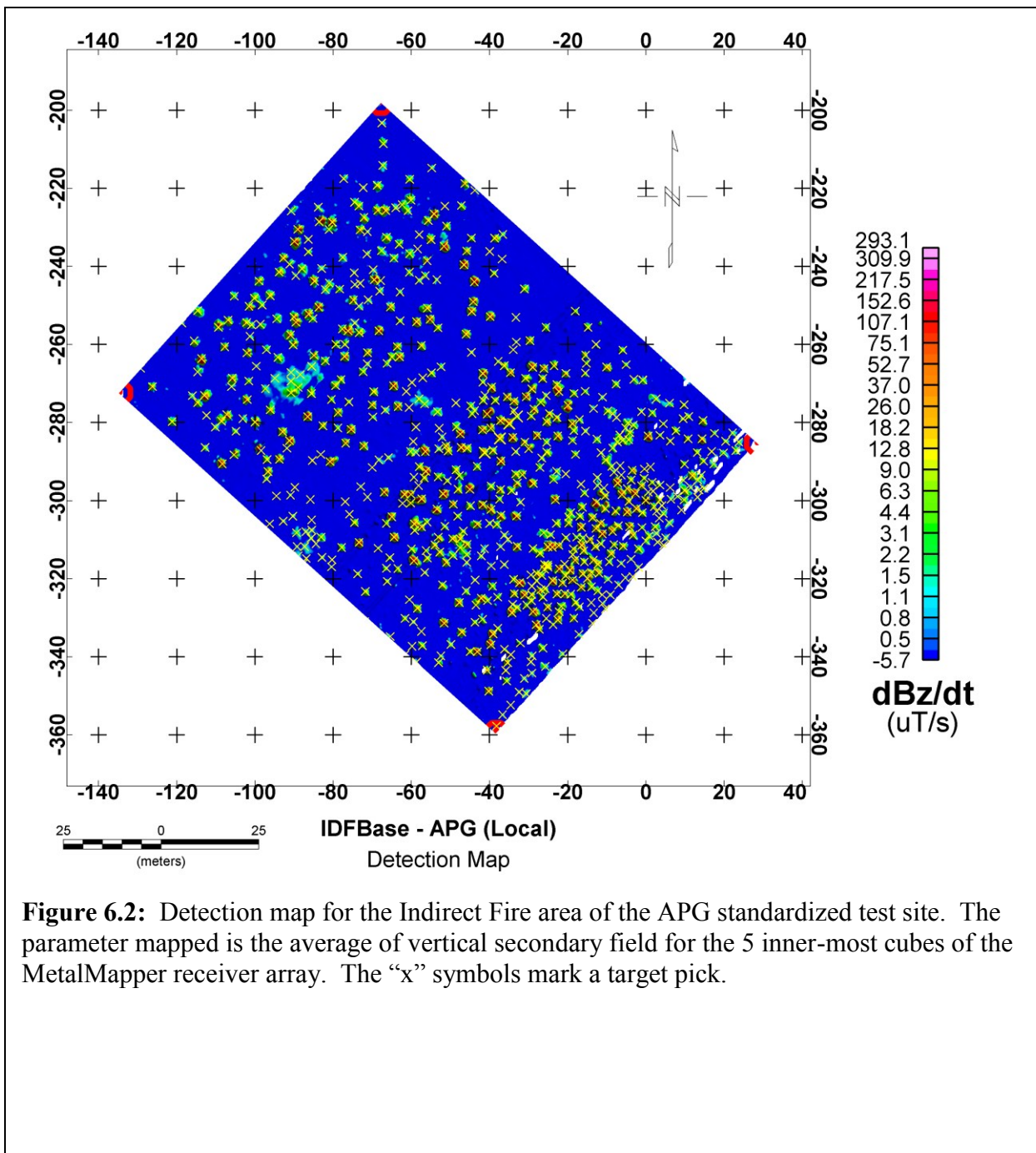


Figure 6.2: Detection map for the Indirect Fire area of the APG standardized test site. The parameter mapped is the average of vertical secondary field for the 5 inner-most cubes of the MetalMapper receiver array. The “x” symbols mark a target pick.

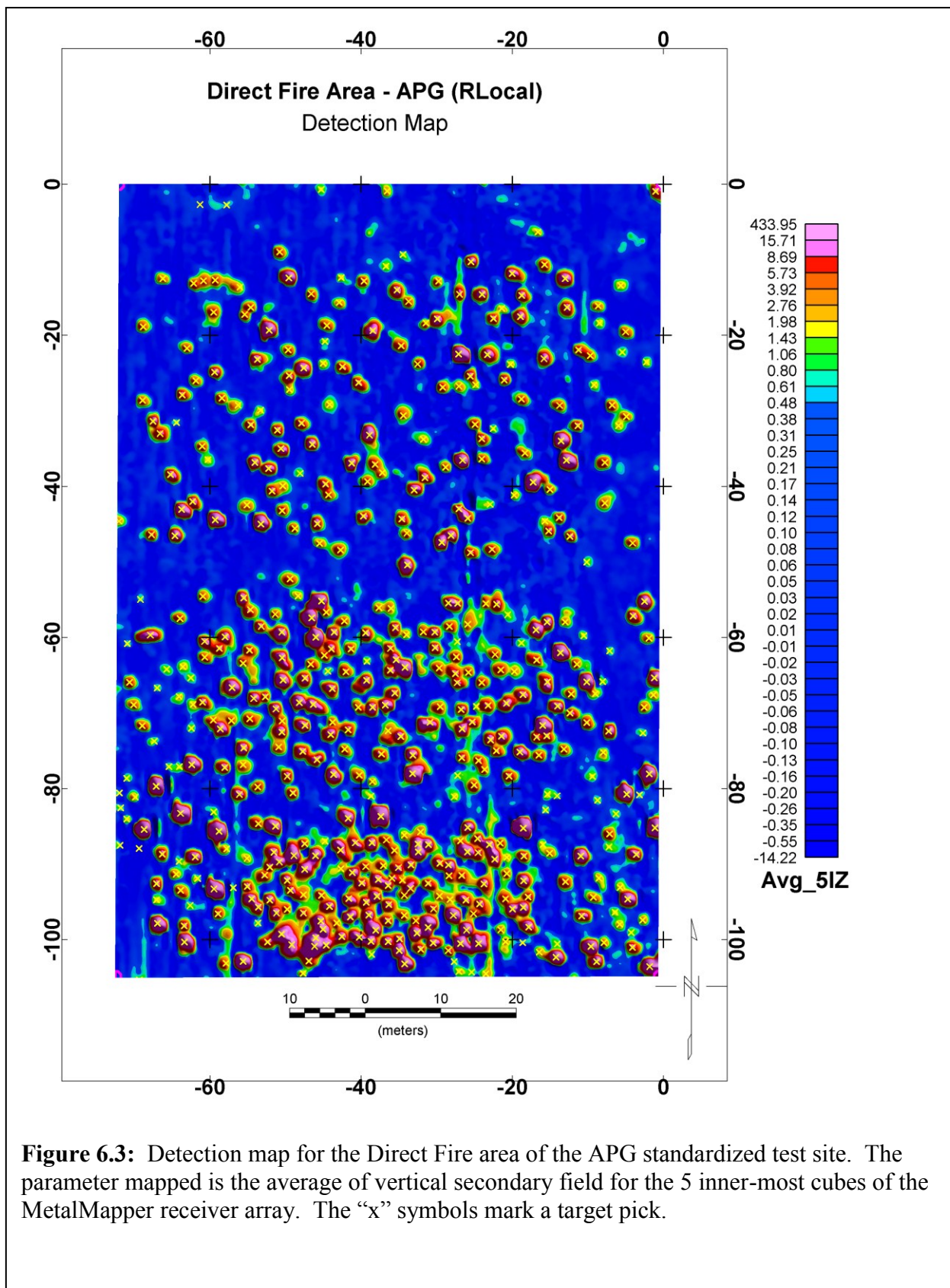


Figure 6.3: Detection map for the Direct Fire area of the APG standardized test site. The parameter mapped is the average of vertical secondary field for the 5 inner-most cubes of the MetalMapper receiver array. The “x” symbols mark a target pick.

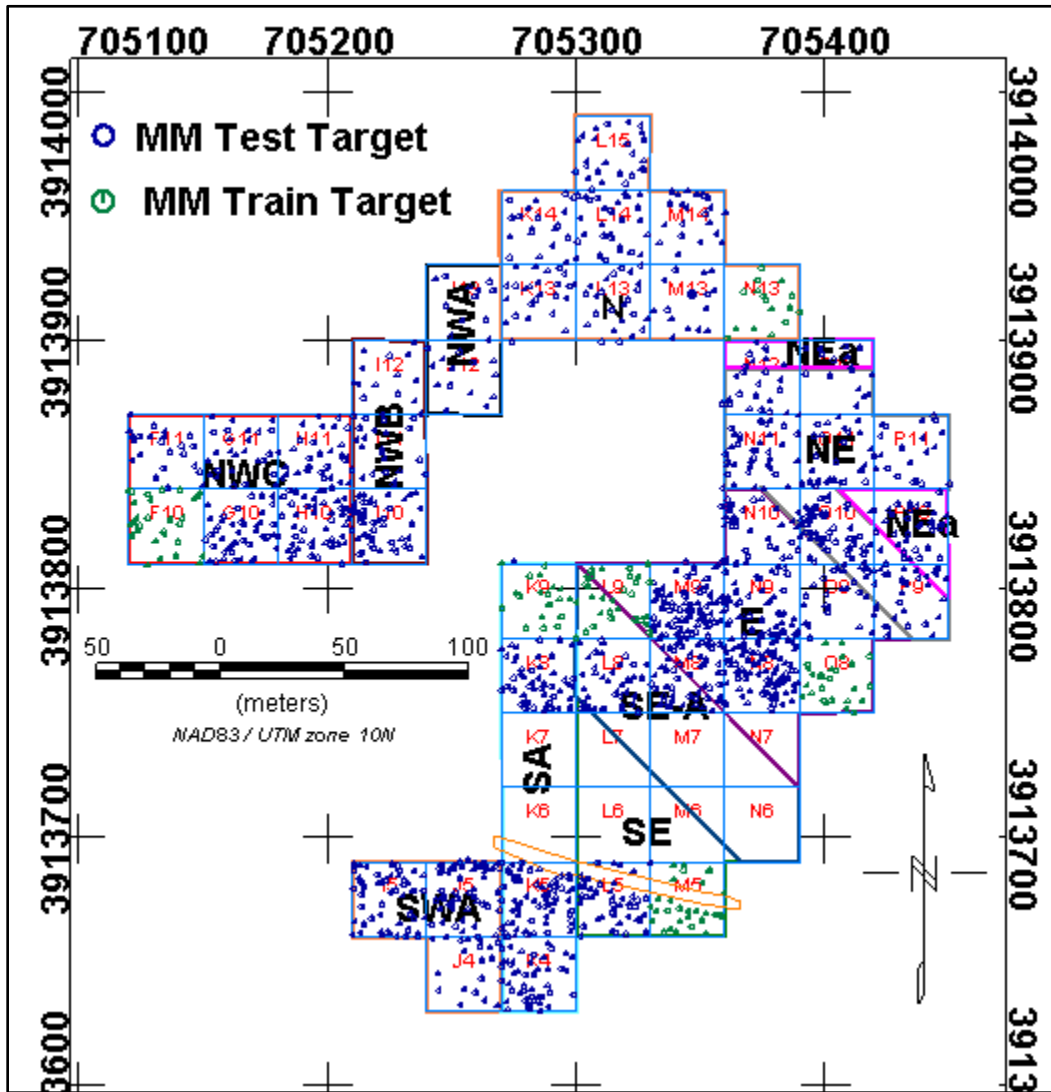
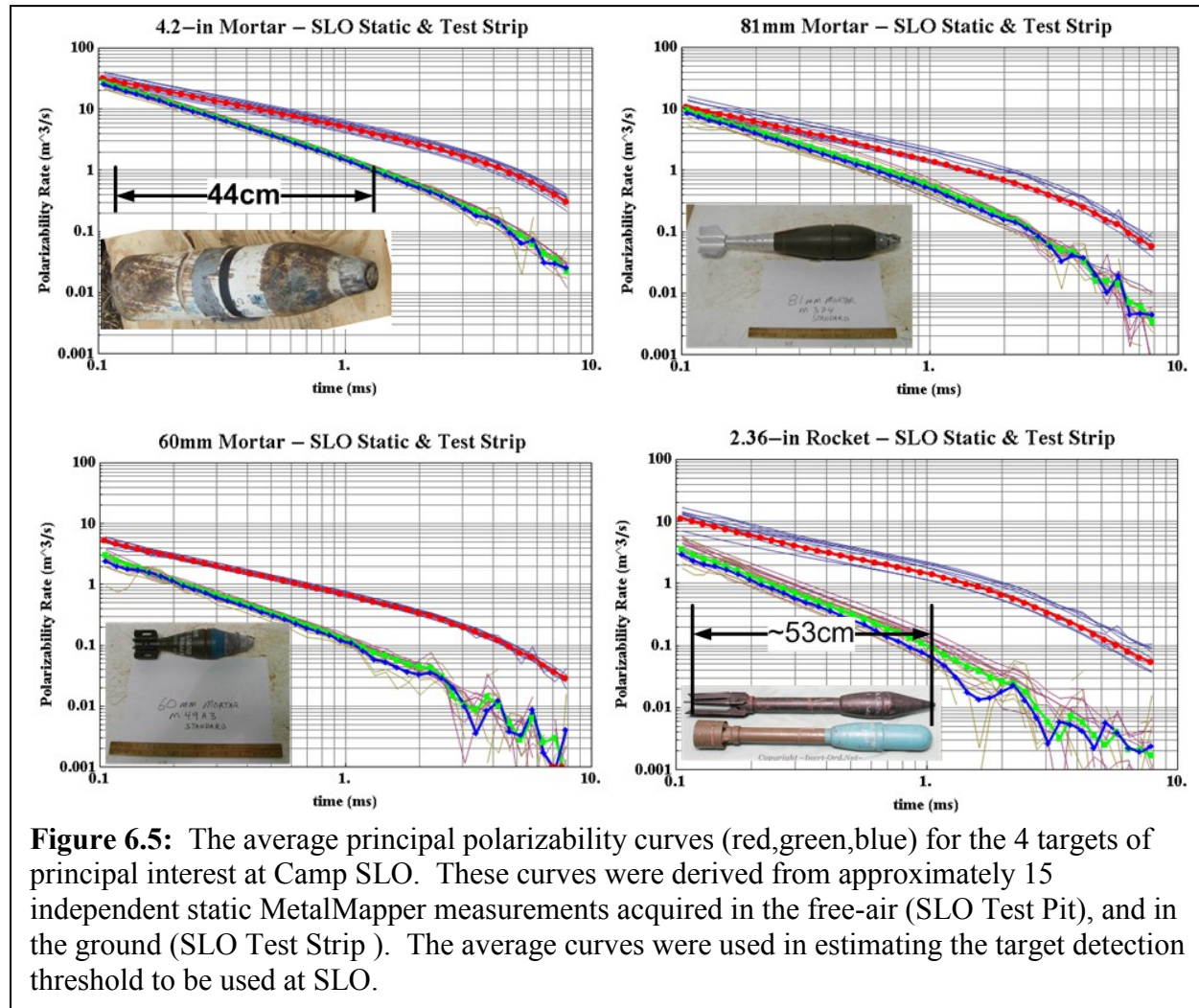


Figure 6.4: Base map of the 11.8-acre study site at Camp San Luis Obispo. The map shows the subdivision of the area into 54 survey blocks (30m x 30m), and 11 sub-areas. Also shown are the target picks based on the MM dynamic survey. Picks marked in green comprise the picks for which ground-truth was supplied to all data processing demonstrators. The blue picks represent targets for which demonstrators submitted a prioritized dig list. The 8 blocks in the rectangular area K6-N7 plus the narrow strip outlined in orange are areas that were excluded from the study for budgetary reasons.

We generally followed the methods and rationale developed by Nelson, et. al. [17] in determining the threshold to apply for target detection at SLO. First, we computed average polarizability transients for the 4 targets of interest. We computed these averages using static data sets that we measured with the MetalMapper over the 4 targets of interest. We were able to use data from YPG and APG for the 60mm and 81mm mortars. We augmented those data with static free-air measurements of the 4 TOI available to demonstrators at SLO for use in the test pit and with static measurements over other targets buried in the test strip. We ended up with approximately 15 data sets for each target type representing a range of depths and orientations with respect to the antenna platform. The results are shown in Figure 6.5. From these curves, we are able to estimate the gated principal polarizability values (i.e. the “betas”) for the time gate ($100 \leq t \leq 900 \mu\text{s}$) that we used in processing the dynamic data to generate a detection parameter. These “betas” were used in modeling the MetalMapper response to each of the 4 targets for a range of depths when positioned directly beneath the antenna platform. Two target attitudes were modeled: vertical, and horizontal. The results of the modeling exercise for the 4 targets for the case of “split cube” processing is shown in Figure 6.6. The Figure suggests that the smallest detection threshold will be about 3 nT/s for the horizontal 2.36-in rocket at a depth of 0.66m below the platform (0.45cm below ground level).



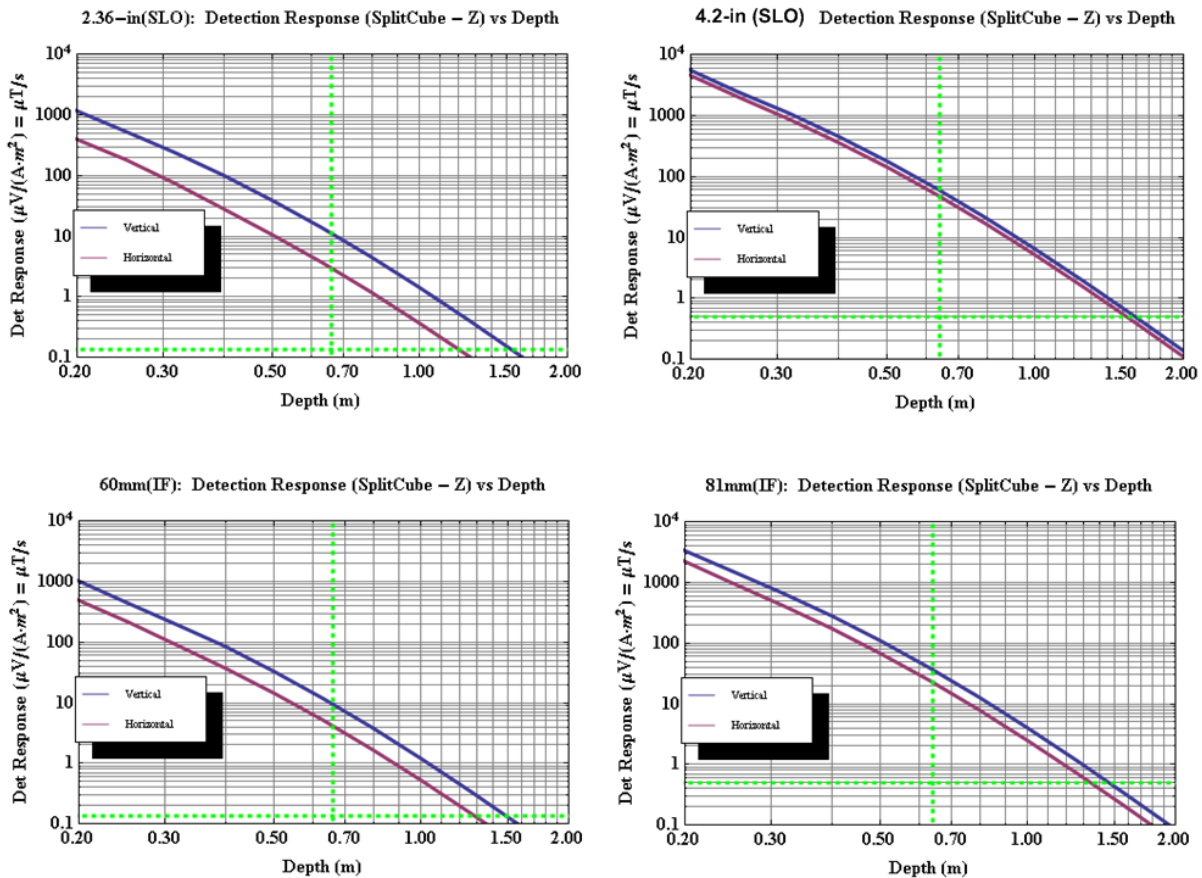


Figure 6.6: Detection plots for the 4 targets of interest at SLO. The curves represent the peak response as a function of depth below the antenna platform for two target attitudes: vertical, and horizontal. The MM platform when deployed on skids is 21 cm above ground level. The dashed vertical green line has been placed at a depth of 66cm (45cm below ground level). The noise floor (shown correctly for the 60mm and 2.36-in targets is around 0.1 nT/s.

During our dynamic survey at SLO, we surveyed the test strip a minimum of twice a day. Each survey of the test strip calls for acquiring data along the test strip in reciprocal directions. As a result, we acquired a total of 60 profiles over the test strip, 30 in each direction. We used these data to experimentally verify the modeling results shown in Figure 6.6. So that the peak amplitudes mimic so far as possible the same amplitudes that we would measure during a dynamic survey over an area, we processed the repeated test strip profiles as if they were an area. We did that follows:

1. Perform steps 1 & 2 as specified in section 6.1.1.
2. Translate coordinate system so that the origin is located at target T-001 (705417.00E,3913682.00N).
3. Rotate coordinates clockwise through an angle of 32.4712° . This aligns the local Y axis with the direction of a line extending from target T-001 to T-010 of the test strip.
4. Offset each profile in the local X direction by a distance $(n-1)*1\text{m}$ where n is the profile number. This creates a series of parallel profiles offset from its neighbor by a nominal offset of 1m.
5. Continue the normal sequence of dynamic processing (step numbers 3-13; section 6.1.1)

The modified processing steps produce a “pseudo-map” of the calibration data as we illustrate in Figure 6.7. We completed the processing by running a threshold peak picker and then editing out the spurious peaks. The resulting target list is easily sorted by rows and allowed us to measure the mean and standard deviation of the peaks.

The astute observer will notice that the pseudo-map shown Figure 6.7 can be divided into 3 vertical zones (A,B,&C). The basis for this sub-division is the fact that we changed from surveying on skids to using wheels and then back to skids at the end of the survey. We used the wheel deployment during the roughest part of the survey. The wheel deployment raises the MetalMapper antenna platform an additional 8.5cm above the ground level and the result of that higher platform elevation produces a noticeable change in the texture of the map. We

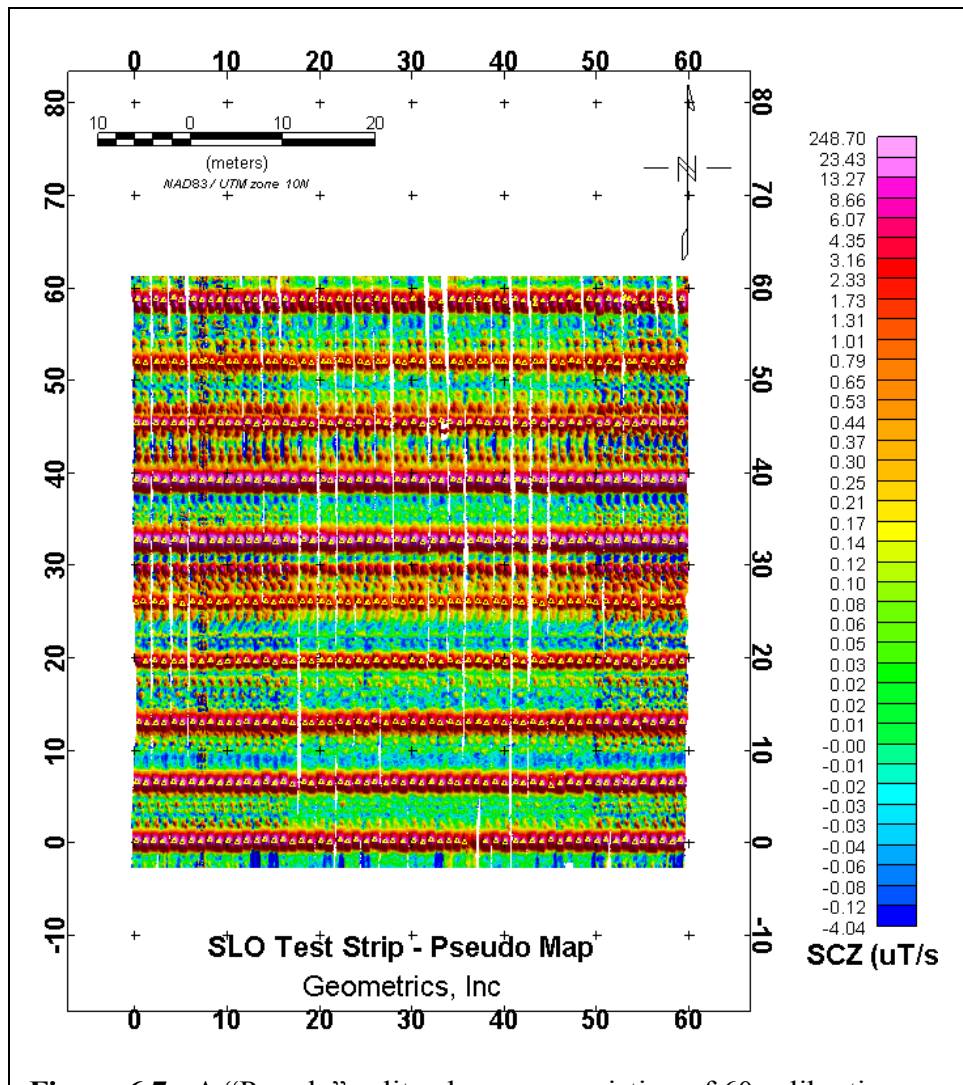


Figure 6.7: A “Pseudo” split cube map consisting of 60 calibration profiles acquired over a period of approximately 3 weeks. Each profile has been offset from its neighbor by 1m. There are 10 calibration targets (rows) at approximately 6m intervals starting at 0m. There are also several spurious “uninvited” targets the most obvious of which is the one that forms the row at about 30m.

computed the statistics for each of the 10 targets in the test strip for each of the configurations. When we adjust for platform height, the target depths with respect to the platform are 51cm (skid deployment) and 60cm (wheel deployment). In Figure 6.8, we have plotted the mean target amplitudes as obtained from the repeated test strip profiles for each of deployment configurations. The plotted experimental points are very close to the model curve for the 2.36-in rocket. The measured responses are a bit low for the mortar. In any case, these results suggest that a threshold of 3 $\mu\text{T/s}$ is appropriate for the MetalMapper when deployed on skids while the threshold must be lowered to 2 $\mu\text{T/s}$ when it is deployed with wheels. We used thresholds of 3 and 2 for detecting peaks.

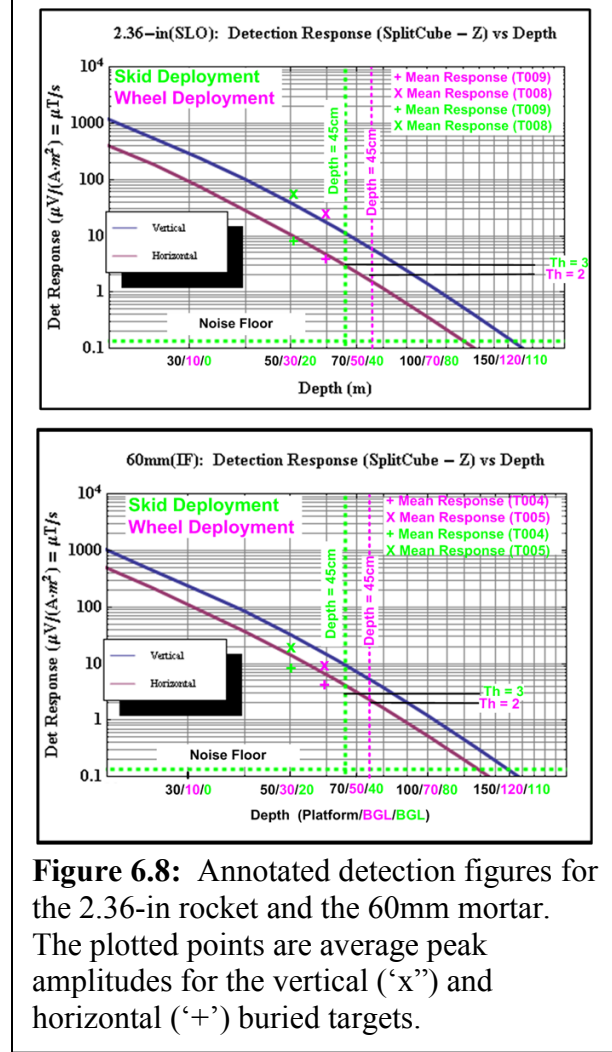


Figure 6.8: Annotated detection figures for the 2.36-in rocket and the 60mm mortar. The plotted points are average peak amplitudes for the vertical ('x') and horizontal ('+') buried targets.

6.3. PARAMETER ESTIMATES

The conceptual processing flow is illustrated in Figure 6.9. The figure shows the 63 transients comprising a data set on the left. The panel on the right are plotted the three principal polarizability rate transients. We call the computer program that accomplishes this transformation **MM/RMP**. The basis of MM/RMP is the ubiquitous point dipole model approximation for approximating the EMI response of a small conducting and magnetically permeable object. Byproducts of this modeling process are estimates of the target position and

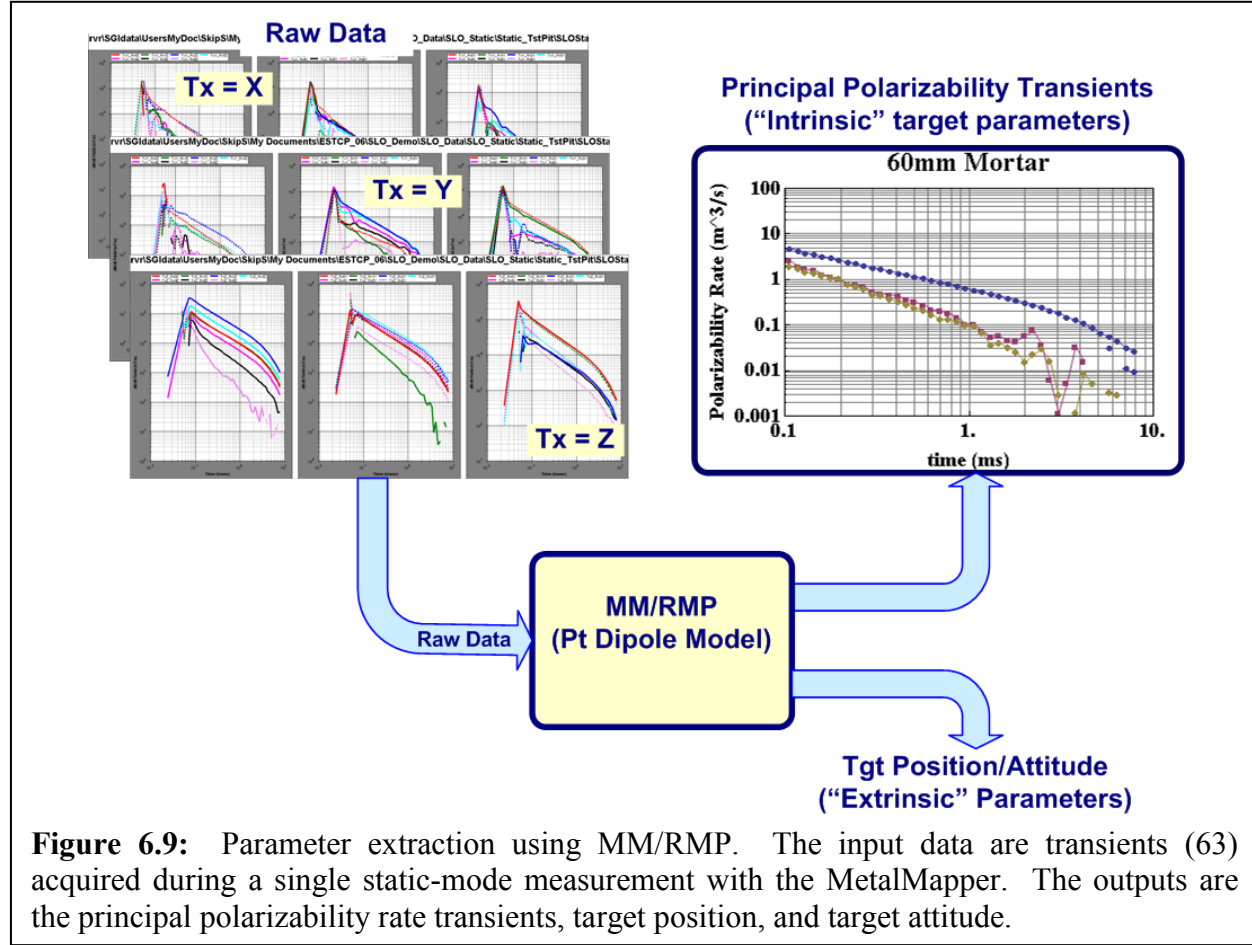


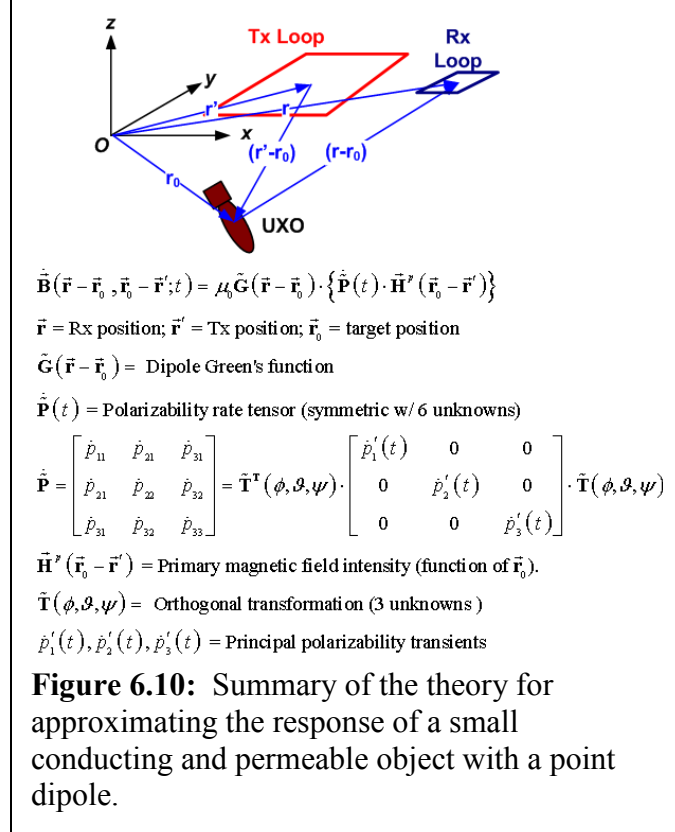
Figure 6.9: Parameter extraction using MM/RMP. The input data are transients (63) acquired during a single static-mode measurement with the MetalMapper. The outputs are the principal polarizability rate transients, target position, and target attitude.

attitude angles. The dipole model approximation is widely used within the UXO community for interpreting UXO [19-23]. A particularly thorough and systematic treatment of the theory can be found in chapter 2 of Leonard Pasion's PhD thesis [24]. The algorithm used in MM/RMP was developed by Torquil Smith at Lawrence Berkeley Labs (LBL) [25]. The basic theory for the dipole approximation of EMI response for small objects is summarized in Figure 6.10. We outline the essential elements of the theory below:

1. We assume that the target is dimensionally small as compared with the distances between the target and the transmitter loop(s) and the receiver loop(s). We also assume that the conductivity of the host medium is low compared with the conductivity of the target object and therefore can be neglected (i.e., "free-space" approximation).

2. To the extent that the assumptions in 1 are valid, we can approximate the behavior of the target as a point dipole characterized with a time- or frequency varying **polarizability tensor (\mathbf{P})**.
3. The primary magnetic field (\mathbf{H}^p) “illuminates” the target object, which is assumed to be very highly conducting and (possibly) permeable. In Figure 6.10, the primary field is generated by transmitter loop (red) carrying a time varying current.
4. Time variations in the primary field induce eddy currents to flow in the target. At any particular time or frequency, the magnitude and direction of the resulting dipole moment is approximated as the tensor product of the primary field vector with the polarizability tensor ($\mathbf{M} = \mathbf{P} \cdot \mathbf{H}^p$).

5. Given the dipole moment vector \mathbf{M} at any particular time or frequency, the value of the secondary field at the receiver loop is determined by computing the tensor product between well-known dipole Green’s functions and the moment ($\mathbf{B} = \mu_0 \mathbf{G} \cdot \mathbf{M}$).
6. As suggested in Figure 6.10, the polarizability tensor \mathbf{P} is a 2nd rank symmetric tensor having 6 independent elements. In such cases, there exists a coordinate system called the “principal axes” coordinate system in which the polarizability tensor is diagonal with only 3 elements. The “principal axes” coordinate system and the observation coordinate system are related by means of an orthogonal transformation (\mathbf{T}). The orthogonal transformation can be expressed in terms of 3 elementary rotation angles (ϕ, θ, ψ) sometimes called the “Euler Angles”. At any particular time or frequency, the response at the receiver is a function of 9 parameters: 1) the 3 coordinates of the target position, 2) the 3 Euler Angles, and 3) the 3 diagonal elements of the polarizability tensor evaluated at a particular time or frequency.
7. Given sufficient independent measurements of the secondary field \mathbf{B} one can estimate the 9 unknown parameters enumerated in 6 using well-known principles of non-linear and/or linear inversion. It is beyond the scope of this report to delve into the details of that process. One can view the inversion process as simply removing the effect of spatial dispersion produced when the source dipole (\mathbf{M}) is convolved with the dipole Green’s function \mathbf{G} . Such a “deconvolution” results in an estimate of the dipole moment vector (\mathbf{M}). \mathbf{M} is the tensor product between the primary field \mathbf{H}^p and the unknown polarizability tensor (\mathbf{P}). Thus finding the 6 unknown components of the polarizability tensor becomes a linear problem if the position of the target is known. Likewise, spatial “deconvolution” requires knowledge of target position so that the Green’s function \mathbf{G} can



be computed. Thus, the essential problem in extracting parameters ultimately reduces to estimating the 3 unknown coordinates of target position.

6.3.1. Implementation Issues

Figure 6.11 is a very much simplified flow diagram of the inversion process as it has been implemented in MM/RMP. In the first step, an optimal position is estimated (a non-linear problem) and then for each time gate the 6 independent elements of the polarization tensor (in

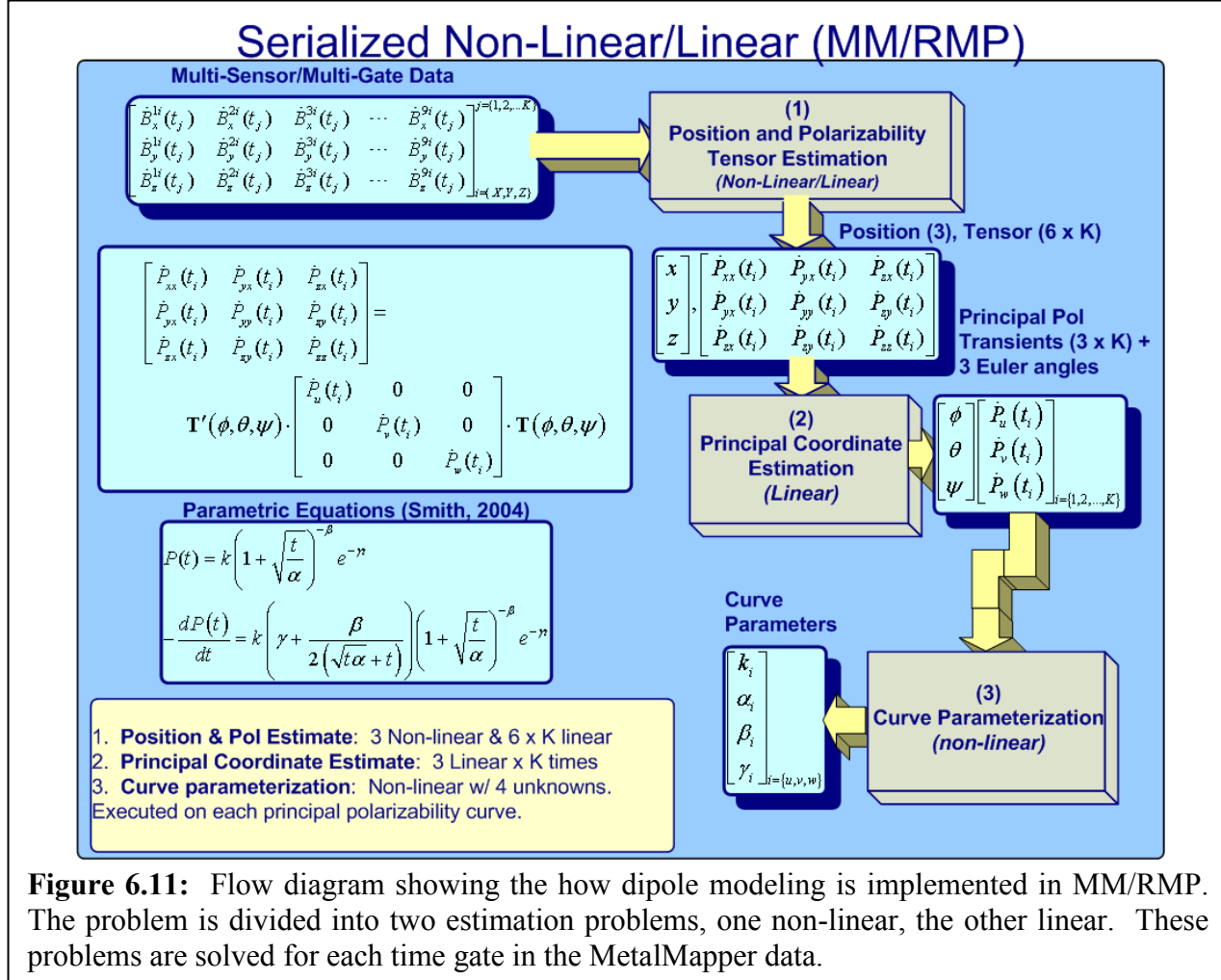


Figure 6.11: Flow diagram showing the how dipole modeling is implemented in MM/RMP. The problem is divided into two estimation problems, one non-linear, the other linear. These problems are solved for each time gate in the MetalMapper data.

the observation coordinate system) are estimated. The latter problem is a series of N linear estimation problems with N being the number of time gates analyzed. And finally, the last step is the estimation of the principal coordinate system. The results of the last step provide estimates of the polarizability rate at each time gate plus the Euler Angles specifying the relationship between the observation coordinate system and the principal coordinate system (a target-fixed coordinate system). This problem is linear. However, there are at least two ways to undertake it:

- 1. Time-Varying Attitude Angles (Type 0):** In this case, attitude angles are computed at each time gate. This method permits the attitude to vary with time. Usually, the electromagnetic attitude remains the same over time. However, there are certain target types where the apparent attitude changes with time (Figure 6.12).

2. **Fixed (Average) Attitude Angles (Type 1):** In this case, we assume that the target attitude is a constant in time and can be determined by computing the Euler Angles based on a time-averaged polarization tensor. Using these angles, the polarization tensor at each time gate is transformed into the principal coordinate system. The diagonal elements of these tensors are assumed to be the values of the principal polarizability transients.¹⁴

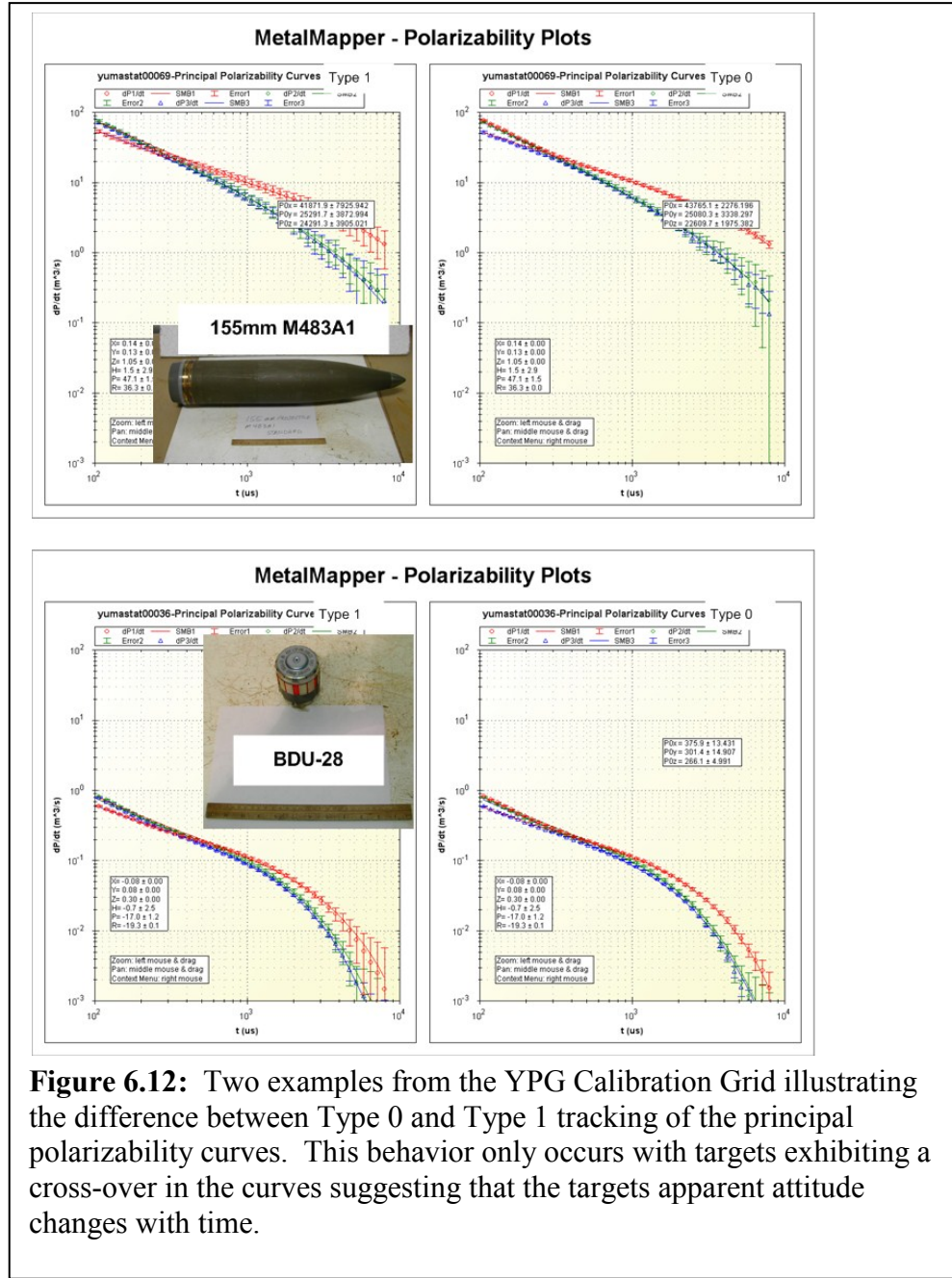


Figure 6.12: Two examples from the YPG Calibration Grid illustrating the difference between Type 0 and Type 1 tracking of the principal polarizability curves. This behavior only occurs with targets exhibiting a cross-over in the curves suggesting that the targets apparent attitude changes with time.

¹⁴ By convention, we order the principal polarizabilities in descending order. This means that the axis of maximum principal polarizability is the target x-axis. For UXO-like bodies, the axis of symmetry will always correspond to the x-axis.

In most UXO types, the principal polarizability curves for the two processing methods come out remarkably alike. And in these cases, the Type 1 method seems to produce better polarizability curves. That is to say that the electromagnetic attitude remains roughly constant with time. However, there are cases where the attitude angles change in time and the two different methods (i.e., Type 0 and Type1) produce different results. Two examples from YPG that illustrate the problem are shown in Figure 6.12.¹⁵ These curves were extracted from a 155mm M183A1 (6.12-top) projectile and a BDU-28 submunition. In the figures, the plotted symbols represent the principal polarizability values estimated at each time gate. The solid lines represent the fit of a 4-term parametric relation to each of the 3 principal polarizability transients. The transients have been colored according to the convention that red is the major (i.e. largest) curve and corresponds to the x-axis of the principal coordinate system. The Green and Blue curves are in decreasing size and are, respectively, the curves for the y-axis and z-axis. In the Type 1 curves on the left, note how points of a particular color (e.g., red) track through the cross-over point and link logically with points of the same color on the opposite side of the cross-over. Now look at the corresponding Type 0 curves (right) for the same target. In both examples, the blue points to the left of the cross-over point appear to link logically with red points to the right. This is an artifact caused by the fact that Type 0 curves are produced by computing the principal coordinate system independently for each time gate. Part of the process of computing the coordinates is to sort the resulting eigenvalues (i.e., principal polarizability elements) in decreasing order. As we pass a cross-over therefore the principal polarizability values are sorted into a different order so that the largest principal polarizability remains with the x-axis of the principal coordinate system. This does not happen in the case of Type 1 curves because the principal coordinate system is only computed once using average principal polarizabilities. Our discrimination techniques are all based on Type 1 polarizability curves or from meta-parameters derived from them.

6.3.2. Meta-Parameters

Parametric Curve Fits -The three principal polarizability curves such as those shown in Figure 6.12 contain all the information available about the target. For the three demonstrations discussed in this report, each curve consists of 42 points spaced logarithmically in time over the range $105 \leq t \leq 7912 \mu\text{s}$. Many authors have noted that the principal polarizability transients are often well described by parametric functions of time or frequency as appropriate with as few as 3 or 4 parameters [26-28]. As a standard operation during the processing of data through MM/RMP, we parameterize each curve using a form of the parametric relation proposed by Smith [28]. It has the form

$$-\frac{dP(t)}{dt} = k \left(\gamma + \frac{\beta}{2(\sqrt{t\alpha} + t)} \right) \left(1 + \sqrt{\frac{t}{\alpha}} \right)^{-\beta} e^{-\gamma t} \quad (6.1)$$

The equation (6.1) has 4 parameters (k, α, β, γ). Each of these parameters has a physical interpretation.

¹⁵ An error in the plotting routine incorrectly labels the dual polarizability plots in Figure 6.12. We have corrected the labels. However, Type 1 plots appear on the left rather than on the right.

1. **k** – this parameter has units of cm^3 when time is expressed in units of μs and dP/dt is in units of $\text{cm}^3/\mu\text{s}$ (equivalent to m^3/s). This parameter approximates the polarizability at the so-called “inductive limit” ($P_0=P(t=0)$).
2. **α** – Smith [28] relates this parameter to transition zone between the early time and intermediate time. With MetalMapper data, this parameter is not very useful. Typically our fits estimate values for α in the range $1 \leq \alpha \leq 100 \mu\text{s}$. Although we sometimes measure time gates earlier than $100 \mu\text{s}$ we have found with MetalMapper data that these early time data are overwhelmed by the amplitude of the background signal. Consequently, we start our analysis of transient decays at $100 \mu\text{s}$.
3. **β** – This is the intermediate power-law decay rate. Typically it takes values in the range $0.5 \leq \beta \leq 2.5$.
4. **γ** – This is the principal late-stage decay rate. The transient fields arising from eddy currents in a conducting body all degenerate at late time to a single exponential decay[29]. For many targets, however, the amplitude of the signal at late time is simply too low to see the late-stage decay much less to estimate it.

We have found that our efforts to parameterize the principal polarizability transients by fitting them to parametric relations such as 6.1 often fail. Probably this is due to a lack of sophistication on our part with regard to robust fitting since others seem to have had success in such parameterization. In any case, we have not used these parameters in our efforts to discriminate UXO targets. Instead, we use the transients directly.

Scalar Meta-Parameters – Many have found success with target discrimination using scalar parameters derived from much simpler instruments. Moments of the principal polarizability transients are easy to compute numerically and very robust with respect to noise. We have benefitted from the insight on the relationship of moments to meaningful target features provided in a paper by Smith and Jones [30]. Mathematically, the n^{th} moment of the polarizability is defined as

$$P_n = \int_0^\infty t^n P(t) dt ; \text{ where } P(t) \text{ is a polarizability rate transient.} \quad (6.2)$$

We calculate the 0^{th} and 1^{th} moments for each of the 3 principal polarizability transients thereby producing 6 scalar “meta-parameters” ($P_{0x}, P_{0y}, P_{0z}, P_{1x}, P_{1y}, P_{1z}$) where the subscripts ($x, y, \text{ and } z$) denote the principal axes coordinates.

For each of these scalar parameter sets (i.e. P_0, P_1) we calculate four additional scalar values two of which relate to target shape:

1. **Transverse Target Polarizability:** $P_{iT} = \frac{\sqrt{P_{iy}P_{ix}}}{P_{ix}}; i = 0, 1$ - This parameter is the normalized geometric mean of the polarizability moments transverse to the axis of maximum polarizability moment.
2. **Target Aspect:** $P_{iR} = \frac{P_{ix}}{P_{ir}}; i=0,1$ - This is a measure of the aspect or elongation of the target. Values of $P_{iR} > 1$ suggest rod-like targets while $P_{iR} < 1$ suggest flat targets

3. **Target Eccentricity:** $P_{iE} = \frac{(P_{iy} - P_{iz})}{P_{ix}}$; $i = 0, 1$ - This is a measure of the eccentricity of the target. A target with good symmetry with respect to the principal x axis will have $P_{0E} \ll 1$.

4. **Target Time Constant:** $\tau_j = \frac{P_{1j}}{P_{0j}}$ - This parameter has the dimensions of time. If the

transient involved were a true exponential decay, then the ratio of the first and second moments can be shown to be equal to the time constant. For UXO targets this will never be the case. However, we can view the parameter as a measure of the time persistence of the transient with higher values meaning longer decays. For the MetalMapper demonstrations discussed here, the time constant values maximize at around 5000 μ s for large munitions (e.g., 81mm, 105mm, 4.2-in, etc). Time constants values for clutter and munitions debris are typically in the range $\tau < 2000 \mu$ s.

6.4. CLASSIFIER AND TRAINING

Our efforts to develop a process for discrimination reflects an evolution over the course of demonstrations at YPG, then at APG, and finally at San Luis Obispo. We believe that the ATC and IDA scoring records reflect the fact that with each demonstration we have improved not only on our scores but also in our ability to effectively discriminate.

Discrimination starts with the estimation of target-related parameters from our data. As we have recounted in section 6.3, we approximate the target with a point dipole-model which results in the extraction of the principal polarizability curves (see Figure 6.9). Our view of a UXO and the behavior of its principal polarizability transients focus (perhaps too narrowly) on shape. When viewed in the principal coordinate system, the polarizability of a UXO will manifest itself by exhibiting a single large (major) polarizability transient over two smaller (minor) transients. Such behavior is illustrated in Figure 6.5, Figure 6.9, and Figure 6.12. Likewise, clutter-like objects do not exhibit such symmetry properties (see Figure 6.13).

When we look at scalar parameters, we see much the same thing. Figure 6.14 is a categorized scatter plot using scalar meta parameters defined in sections 6.3. The static data are from the Calibration Grid at APG. All data points plot above the line $P_{0x} = P_{0T}$ suggesting that all targets are elongate. The BLU-26, BDU-28, Calibra_Ball, and 105mm(DF) plot very close to the line suggesting that they are equi-dimensional (sphere-like). Each munition type clusters together on the plot. However, the points representing clutter are scattered over a broad range.

In theory, the 0th moment parameter (i.e., P_{0i}) has the units of volume and is related to target size. We do not have volumes for the targets at YPG and APG, but we do have their weights. In Figure 6.15, we have plotted the RMS(P_{0i}) against the target weights in order to demonstrate the direct relation between P_0 and target size. We have color-coded the points according to three categories (small, medium, and large) that have been defined by ATC. This

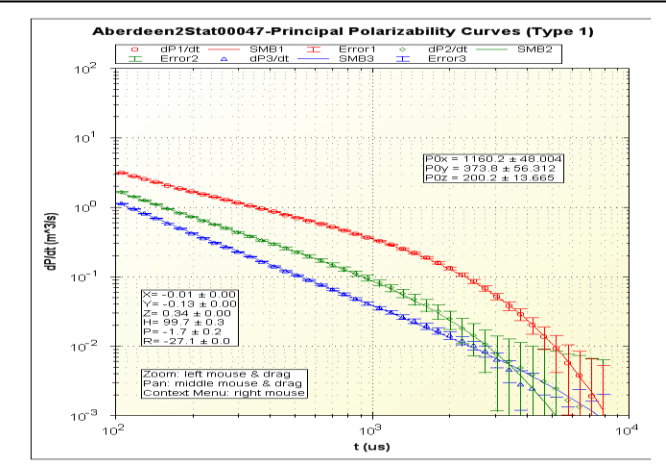


Figure 6.13: Example of principal polarizability curves for a clutter object. The object does not exhibit the symmetry characteristic of UXO. This object is buried in the Calibration Grid (cell D2) at APG.

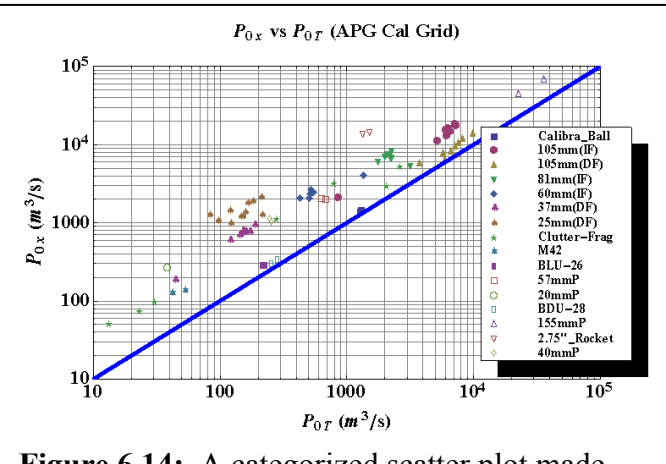


Figure 6.14: A categorized scatter plot made with two scalar parameters extracted from data taken over the calibration grid at APG.

Figure provides us with excellent empirical evidence that any measure of integrated polarizability can be directly related to target size.

6.4.1. Discrimination at YPG

We have used several plots of the principal polarizability transients to illustrate various points (see Figures 5.3, Figure 6.5, Figure 6.12, and Figure 6.13). With good data, an interpreter can easily discriminate between items that are most likely targets of interest (TOI) and items that are most likely clutter. The visual (and numerical) clues are:

1. **Object Size** – Size as suggested by the 3 scalar values (P_{0x} , P_{0y} , P_{0z}) can be used to narrow the possibilities to one of three size classes (see Figure 6.15).
2. **Symmetry (Eccentricity)** – In most cases, the principal polarizability curves should indicate a rod-like body having a large major polarizability curve and 2 smaller minor polarizability curves of roughly the same size and shape. This is the case for all examples we have shown thus far. It is important to be aware, however, that the target may not always exhibit perfect symmetry.¹⁶ Note the symmetry or eccentricity property is a function of time.
3. **Aspect Ratio** – The ratio of the major curve to the geometric mean of the minor curves. This ratio is a function of time.
4. **Major Polarizability Shape** – The shape of the largest principal polarizability curve is often very distinctive.

For the Blind Grid target list at YPG, we used the polarizability plots from each of the target cells to decide whether the target was a “O” (Ordnance) or “C” (Clutter). The prerequisite for that decision was that the target exhibit symmetry and correlate (visually) with a catalog containing 19 “Type” polarization curves. This catalog included both the graphical behavior of the principal polarizabilities for each of the 19 ordnance types, and the values of the various scalar meta-parameters that are computed by MM/RMP and stored in the target database. As we suggest in Figure 6.16, the decision about whether the target is ordnance or clutter was made by the interpreter. In making the decision, the interpreter assigns a numerical “Grade” in the range (0,3) that indicates a rough confidence level in that decision. As a second stage, a decision metric (M_D) in the range (0,6) is computed according to the formulas shown in Figure 6.16. A

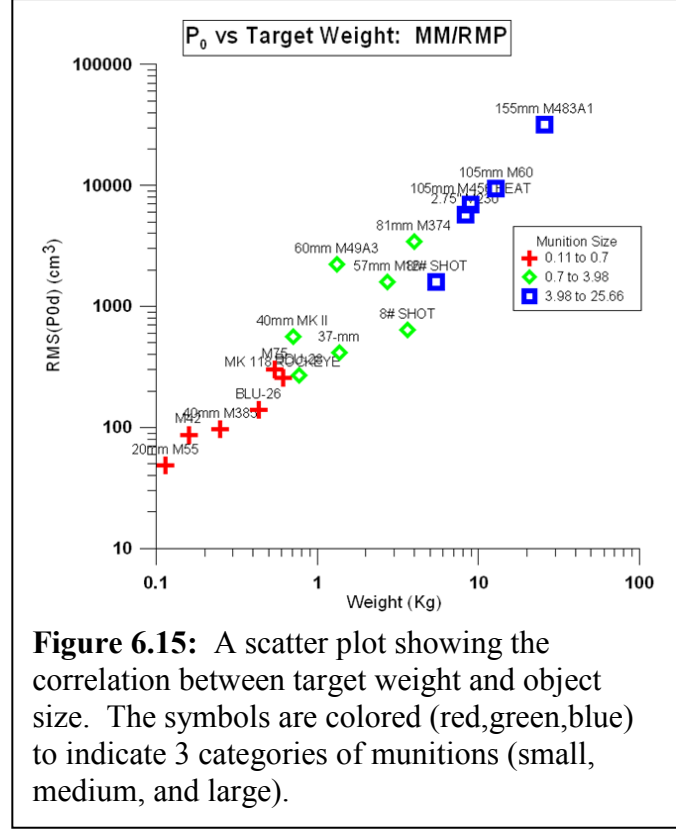


Figure 6.15: A scatter plot showing the correlation between target weight and object size. The symbols are colored (red,green,blue) to indicate 3 categories of munitions (small, medium, and large).

¹⁶ Symmetry properties of the principal polarizability curves are sometimes compromised by large lateral offsets between the target and the center point of the antenna array. Symmetry can also be compromised by pitch angles between 30° and 60°. A TOI may have some physical damage that changes its principal polarizability curves.

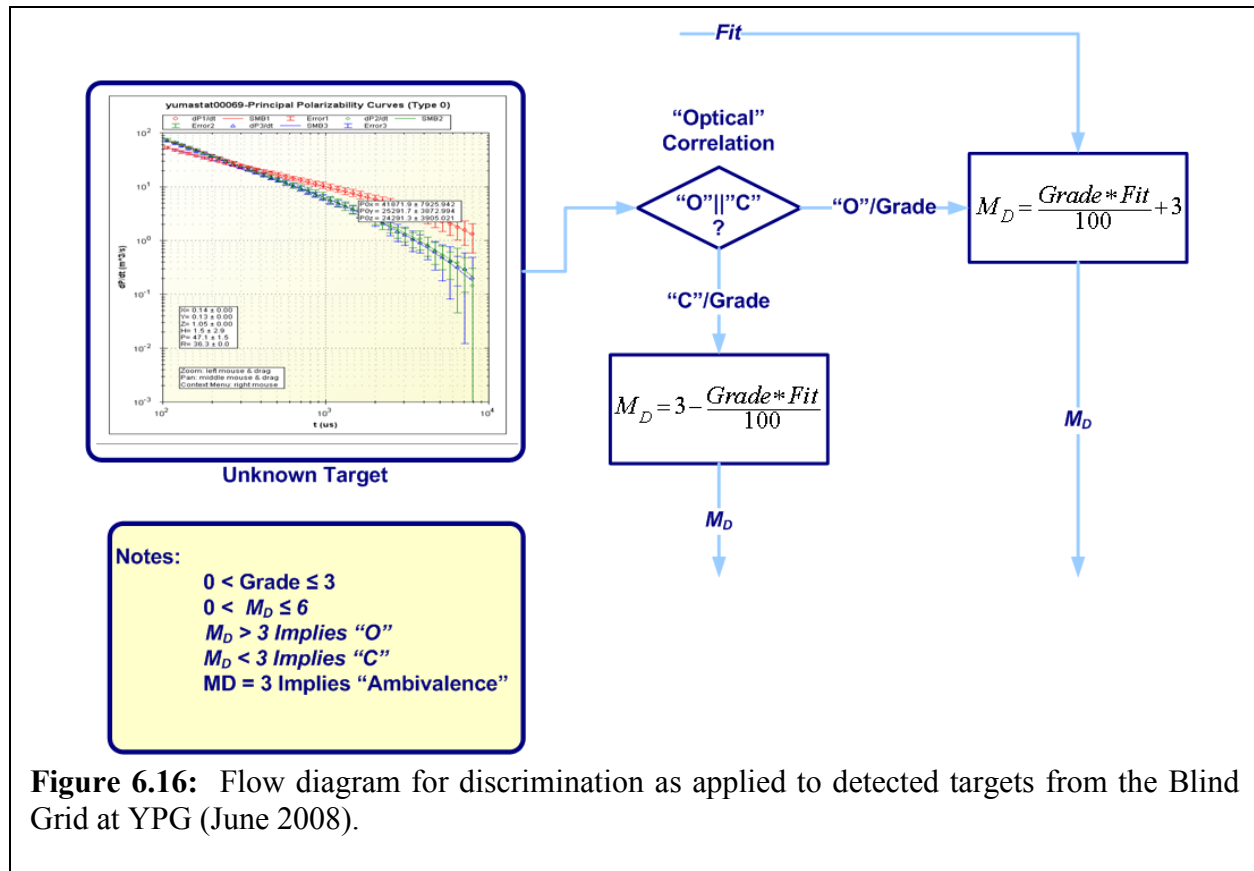


Figure 6.16: Flow diagram for discrimination as applied to detected targets from the Blind Grid at YPG (June 2008).

score of $M_D=6$ indicates highest confidence Ordnance, while $M_D=0$ indicates highest confidence clutter.

Admittedly, this was a crude and basically “unprincipled” method for preparing a target list. Nonetheless, we achieved a very respectable discrimination score of 100% (rounded to the nearest 5%) [15].

6.4.2. Discrimination at APG

In preparing our target lists for the APG demonstration, we were aided considerably by its reconfiguration completed early in 2008. As a result of that reconfiguration, the Blind Grid now contains only 6 ordnance types. And the Direct and Indirect Fire Areas each contain 3 types, which are mutually exclusive subsets of the 6 types seeded in the Blind Grid. Building on our experience at YPG, we tried to develop a more principled approach to discrimination. This approach was based on 3 levels of principled discrimination:

1. Data Quality
2. Rule-based Decisions
3. Library Curve Matching

A schematic flow diagram of the discrimination process we used for discrimination of our APG static data is shown in Figure 6.17 below.

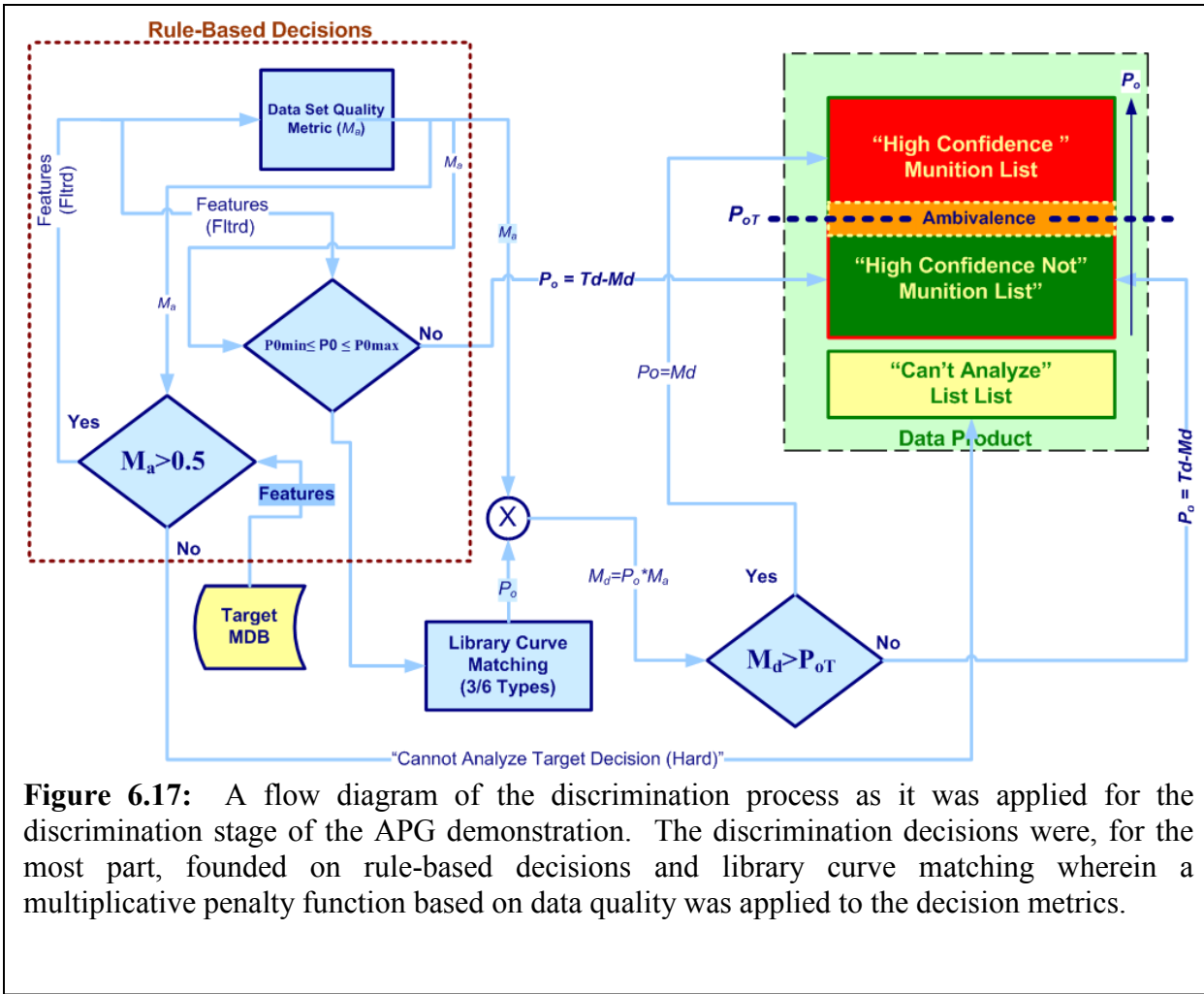


Figure 6.17: A flow diagram of the discrimination process as it was applied for the discrimination stage of the APG demonstration. The discrimination decisions were, for the most part, founded on rule-based decisions and library curve matching wherein a multiplicative penalty function based on data quality was applied to the decision metrics.

Data Quality

Our experience with MM/RMP indicates that if a static data set has an SNR > 10 and the target is an isolated object, we can nearly always expect the fit statistic resulting from a MM/RMP model fit to the data to be greater than 90%.¹⁷ Figure 6.18 is a 3D plot showing the SNR and the Fit from 79 seeded targets from the APG calibration grid. The third dimension (labeled M_a) is a “figure-of-merit” (FOM) value derived from SNR and Fit. We have also modulated the color of the plot points with M_a (warm colors for high M_a ; cool colors for low M_a). Only 4 points in the figure fall off the trend. Those points have $\text{SNR} \geq 20\text{dB}$ and $\text{Fit} \text{ statistics } 70 \leq \text{Fit} \leq 80\%$ and correspond with M42 and BLU-26 targets, small submunitions that for some reason are not fit well with a dipole model. We used the figure-of-merit parameter M_a as a measure of discrimination for measured data sets with regard to their analyzability. Based on our study of the APG cal lanes, a threshold value of $M_a \geq 0.5$ gets all the good analyzable data.

¹⁷ A perfect fit is 100%.

Rule-Based Decisions

The categorized scatter-plot shown in Figure 6.14 shows how the 6 targets of interest are separated and well grouped by two scalar parameters (P_{0x} and P_{pT}). The figure also illustrates that targets having values of $P_{0x} < 700 \text{ cm}^3$ are not targets of interest provided that we can believe the estimates of P_{0x} that are provided by MMRMP. We are able to make this statement because at APG, there are only 6 targets of interest. Based on the a priori knowledge about the TOIs, together with our knowledge of the relationship between SNR and Fit to the quality of the target parameters, we are able to apply a set of rule-based decisions that serve to classify many of the targets. As suggested Figure 6.17, the following rules are applied:

1. All targets with a value of $M_a < 0.5$ (i.e., low SNR and/or Fit) are designated as “Cannot Analyze.” These targets must be dug in order to preclude the possibility that some may be ordnance.
2. All targets with a value of $P_{0x} > P_{0xmax}$ or $P_{0x} < P_{0xmin}$ will be designated as clutter with a decision metric value of $M_d = M_a$ where M_a is the figure-of-merit factor indicating data quality.

Values for P_{0xmax} and P_{0xmin} are determined by computing the statistics (mean and standard deviations) for the scalar parameters associated with each of the target types of interest. For this purpose, we used the data sets we acquired over the Calibration Grid. In Table 6.1 we have tabulated the observed mean and standard deviations for the 6 TOI's together with the values for P_{0xmax} and P_{0xmin} . The minima were taken to be the mean minus two standard deviations for the smallest target. Likewise, the maxima were taken to be the mean plus two standard deviations for the largest relevant target. The standard deviation values are also required in our library target matching algorithm.

Table 6.1: Statistics and min/max values for each of the 3 blind areas at the APG test site.

Target	POX		Blind Grid		Direct Fire Area		Indirect Fire Area	
	Mean	S.D.	POX_Max	POX_Min	POX_Max	POX_Min	POX_Max	POX_Min
25mm(DF)	1443	395	N/A	N/A	N/A	653	N/A	N/A
37mm(DF)	700	226	N/A	248	N/A	N/A	N/A	N/A
105mm(DF)	9410	2783	N/A	N/A	14976	N/A	N/A	N/A
60mm(IF)	2582	670	N/A	N/A	N/A	N/A	N/A	1242
81mm(IF)	7041	783	N/A	N/A	N/A	N/A	N/A	N/A
105mm(IF)	13748	5216	24180	N/A	N/A	N/A	24180	N/A

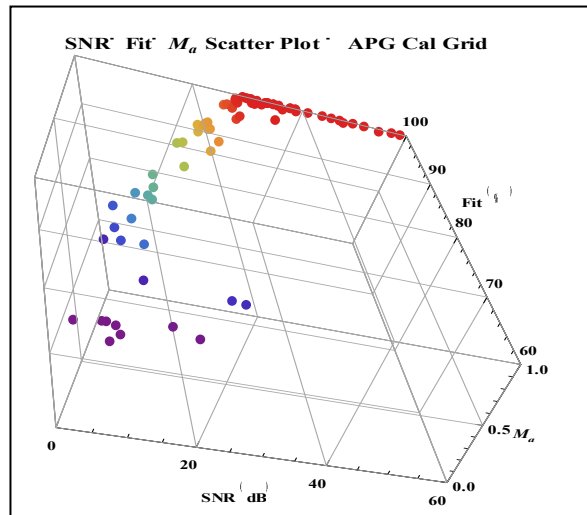


Figure 6.18: Scatter plot illustrating the relationship between static data SNR and Fit. The 3rd dimension is a figure-of-merit metric M_a that can be used as a penalty function for discrimination of data sets with low SNR and/or low Fit statistic. The data are from the cal lanes at APG. Color has been modulated by M_a .

Library Curve Matching

For completeness, we have included polarizability plots for each of the 6 ordnance types as Figure 6.19. In these plots, curves representing 5 or 6 different static data sets from the Calibration Grid are plotted. The targets were seeded at 2 depths and 2 or 3 different attitudes. Also included in the plots are the geometric average polarizability curves representing $P_x(t)$ and $P_T(t)$ (dashed turquoise and magenta curves, respectively). We used the 6 pairs of average “type” curves as library curves in a curve-matching algorithm for discrimination. Table 6.2 lists the 3 areas of interest at APG and the ordnance targets they contain.

Table 6.2: The 6 targets of interest (TOI) at the APG demonstration site. The “X” designates that targets of the indicated type have been seeded in a particular area.

Target Type	Blind Grid (BG)	Indirect Fire Area (IF)	Direct Fire Area (DF)
25mm M792	X		X
37mm M63M1	X		X
105mm HEAT M486	X		X
60mm Mortar M49A3	X	X	
81mm Mortar M324	X	X	
105mm M60	X	X	

Matching with library curves is performed in log space. Rather than match the 3 principal polarizability curves individually, we characterize the curve set with 2 transient curves, dP_x/dt and the gate by gate ratio $dP_x/dt/\sqrt{(dP_y/dt dP_z/dt)}$, and a scalar measure of the single-axis symmetry characteristic P_{OE} . A flow diagram of the process is illustrated in Figure 6.20. The process has 1 global parameter (n) plus 1 type-specific parameter (σ_i). We match the two transients derived from the 3 principal polarizability transients¹⁸ with similar transients derived from the **Target “Type” Library**. The matching function for dP_x/dt depends on amplitude as well as shape and thus delivers an estimate of the ratio of the amplitude of the two major polarizability curves. The second transient (labeled P_r in Figure 6.20) is a ratio of two polarizability rates and thus is independent of amplitude. Therefore, the matching simply provides an estimate of shape. The two shape matching results are, respectively, φ_x and φ_r . These outputs take a value of 1 when the shape is perfect. We use the amplitude ratio parameter (g) in a Gaussian penalty function to effectively diminish the value of φ_x when the amplitude ratio of the library type and the unknown type is different than 1. If there is a perfect match, $g = \varphi_x = \varphi_r = 1$. The behavior of the gain penalty function is controlled by two parameters (n , and σ). We choose the value n such that there is a substantial penalty on the output value (ϑ_i) when the principal polarizability curve set is outside the expected range of amplitudes. We chose the value of $n=2$ which penalizes a good shape fit by a factor of 0.6 when the gain is 2 geometric standard deviations away from the geometric mean. The value of σ is related to the standard deviations

¹⁸ The ratio transient $P_r(t)$ is the ratio of the 2 dashed curves shown in Figure 6.17.

reported in Table 6.1. The algorithm penalizes a match when the unknown target polarizability curves exhibit poor symmetry characteristics as quantified by the scalar parameter P_{OE} . P_{OE} is always in the range $0 \leq P_{OE} \leq 1$ and has the value 0 when the two minor principal polarizability curves are identical. So the penalty function $p=1- P_{OE}$ penalizes a good match when the unknown data set has poor symmetry.¹⁹

The methodology outlined above produced good discrimination scores [16]. The scores will be discussed in more detail in section 7.

¹⁹ P_{OE} for ordnance is typically less than 0.1. Many obvious clutter objects have P_{OE} values on the order of 0.2, so the penalty function $(1- P_{OE})^{n=1}$ is perhaps overly lenient. Perhaps the exponent should be 2? We have not tested this.

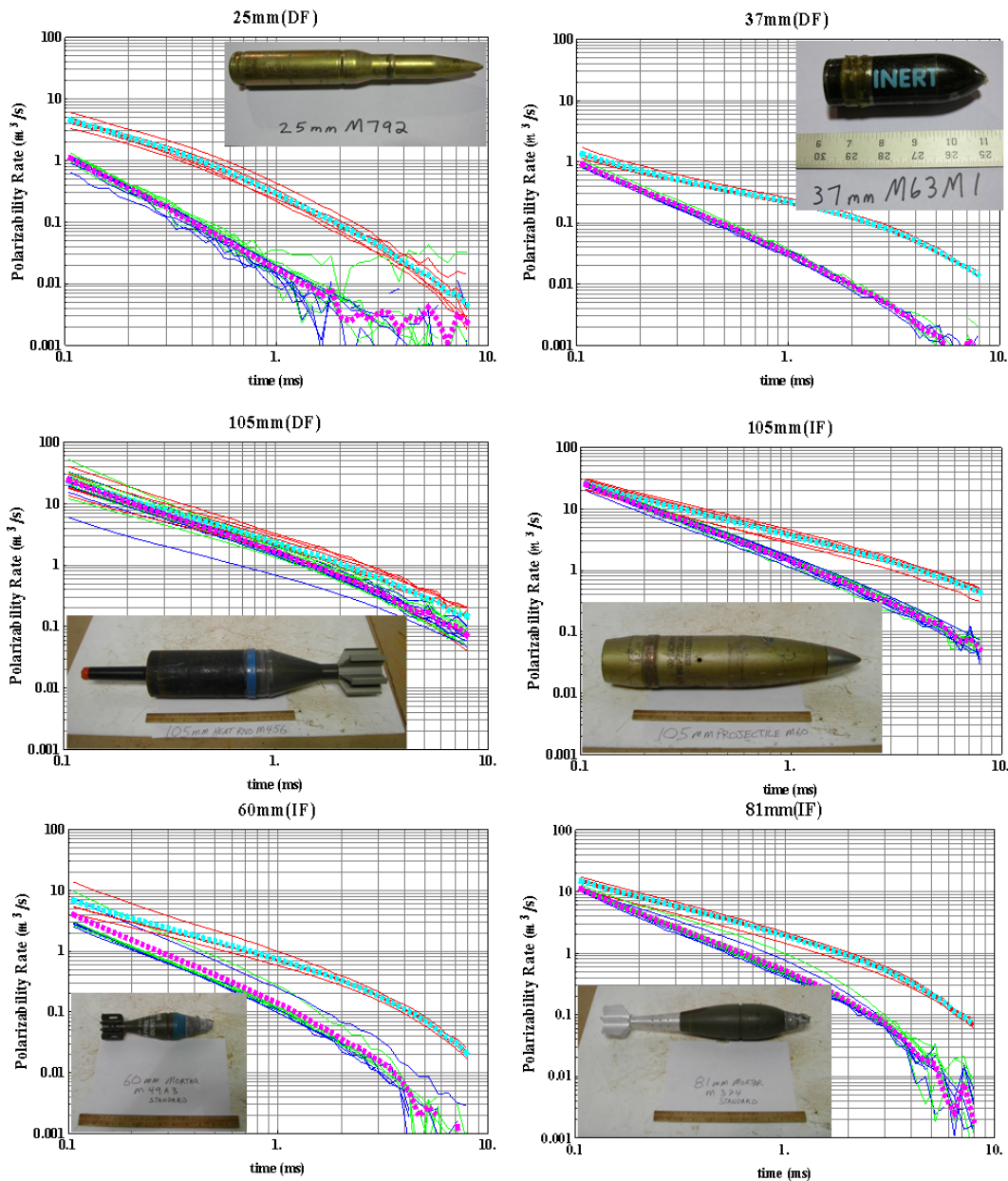


Figure 6.19: Polarizability plots of the 6 ordnance types of interest in the recently reconfigured UXO test area at APG. All 6 are present in the Blind Grid. The 3 types identified with an appended “(DF)” have been seeded in the “Direct Fire” area and likewise type names with an appended “(IF)” have been seeded in the “Indirect Fire” area. The heavy dashed curves represent the (geometric) average of a population of training polarization curves extracted from MetalMapper data acquired over the Calibration Grid at APG.

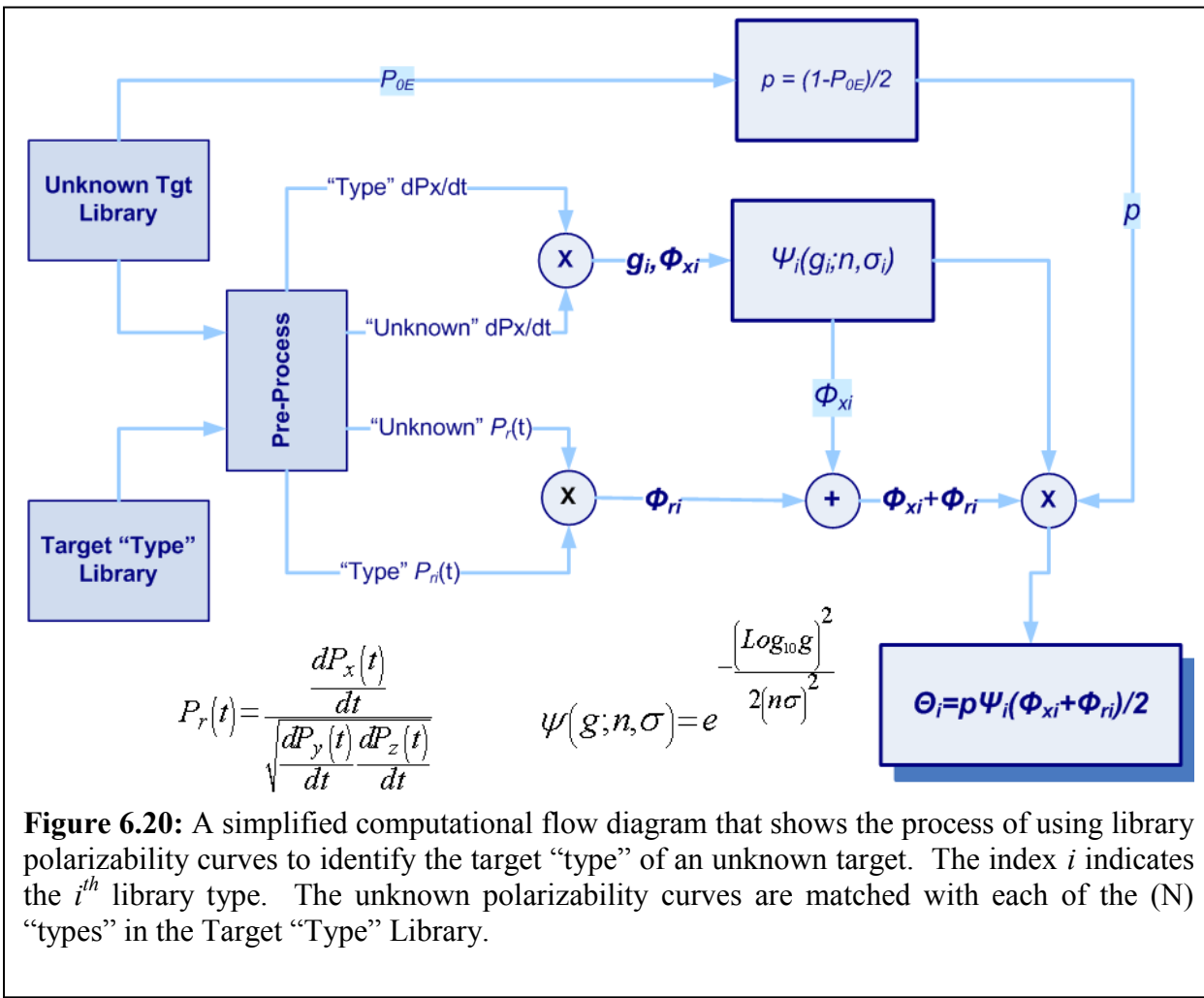


Figure 6.20: A simplified computational flow diagram that shows the process of using library polarizability curves to identify the target “type” of an unknown target. The index i indicates the i^{th} library type. The unknown polarizability curves are matched with each of the (N) “types” in the Target “Type” Library.

6.4.3. Discrimination at Camp San Luis Obispo

The discrimination at APG was decidedly more “principled” than the approach we described for YPG. The library matching does a good job of identifying targets of interest when the Fit is good. But, as the matching threshold is lowered so as not to miss targets that are obviously ordnance (based on visual correlation with polarizability curves), many false positive decisions appear. For the San Luis Obispo demonstration, we therefore added an automated neural network (ANN) to our discrimination algorithm. The discrimination flow diagram for SLO (Figure 6.21) is similar to the one for APG (Figure 6.17). However, we have now expanded our processing flow to include an ANN that operates on a set of 9 scalar features derived from the polarizability curves. The ANN assigns a binary decision (i.e. “TOI” or “Clutter”) to each data set not otherwise classified by rule-based decision. As a final step, we use the library matching algorithm as a means to identify TOI that elicit false negative decisions from the ANN.

In the following paragraphs, we expand on our use SNR and Fit parameters in deciding whether data are analyzable, and we review our rule-based decisions. Then we provide a thorough explanation of the ANN that we used and results from that training. With regard to library curve matching, there have been no substantive changes to the algorithm that we outlined in section 6.4.2. We used 5 library “type” curves in our matching. We present those library types and discuss their significance.

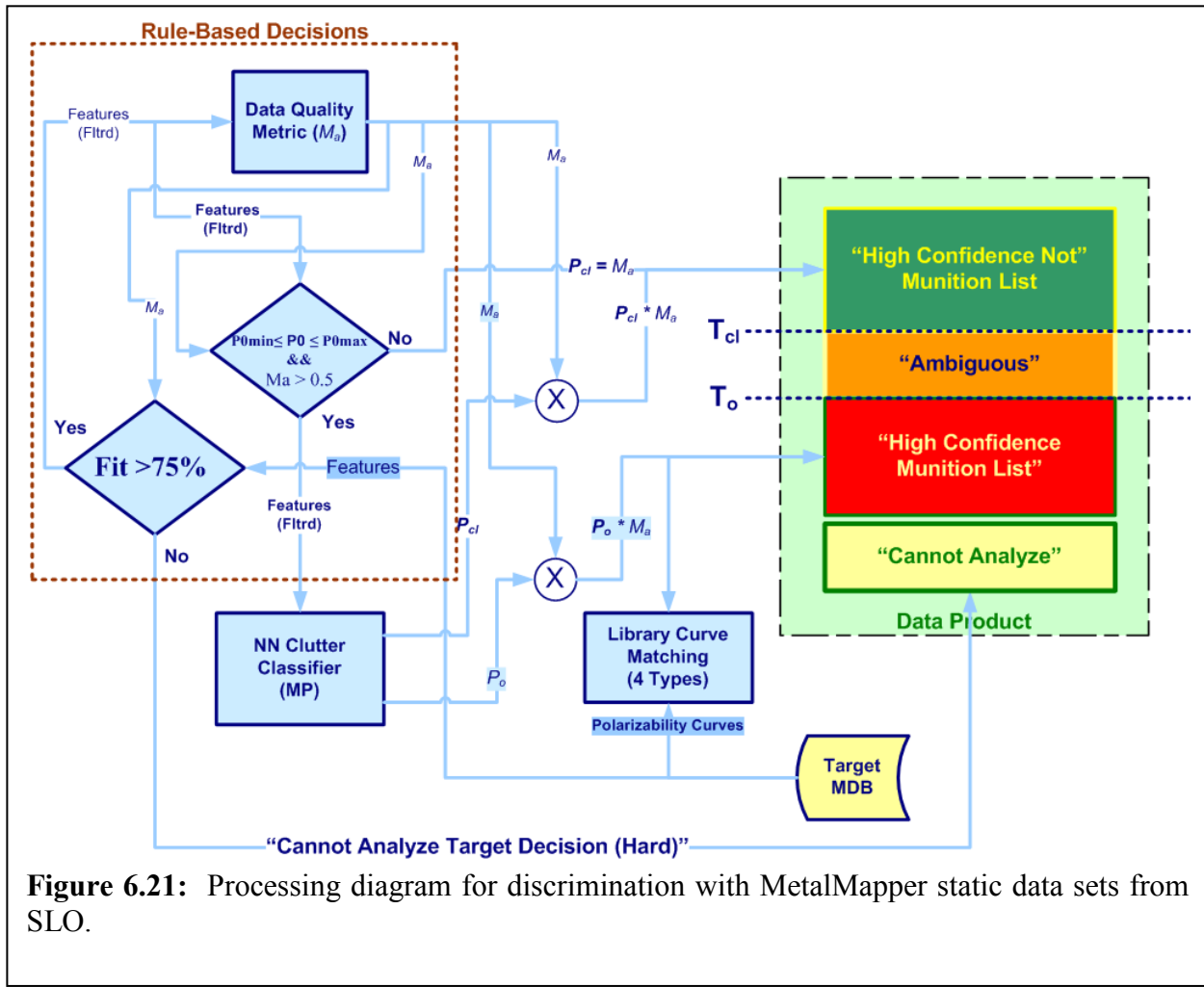


Figure 6.21: Processing diagram for discrimination with MetalMapper static data sets from SLO.

Data Quality and Rule-Based Decisions

The overriding objective for the rule-based decisions is to select static data sets that we believe can be analyzed. Assuming we have an analyzable data set, MMRMP provides reliable estimates of target position and target size (as expressed by the integrated principal polarizability values, P_{0x} , P_{0y} , P_{0z}). The size estimates can be used to eliminate those targets that are either too large or too small to be a target of interest (TOI). Our experience in the analysis of AOL2 and MM static data at YPG, and at APG suggest that we obtain reliable estimates of position and target size when the $\text{SNR} > 10$ and the $\text{Fit} > 85\%$ and our first inclination was to screen the data and designate all data sets for targets whose SNR and/or Fit falls below these thresholds. However, after examining polarizability curves and scalar meta-parameters (see section 6.3.2) for many data sets with Fit statistic values less than 85%, we are convinced that $\text{Fit} = 85\%$ more likely defines the upper end of a transition zone. In this zone, the reliability of the data certainly declines in an undefined but monotonic way. We believe that we can still rely on MMRMP to produce rough estimates of target position and size. A look at the distribution of the SNR and the Fit for the 2492 static data sets that we acquired is instructive (Figure 6.22). The SNR histogram (Figure 6.22-Top) that there are only 15 data sets with an SNR of less than 25dB. Thus at SLO, SNR by itself will be ineffective as a means of identifying “Cannot Analyze” data sets. Secondly, the distribution of Fit statistics indicates that a total of 771 data files have Fit

statistics falling below the 85% threshold. In an effort to minimize so far as possible the number of data points we place immediately into the “Cannot Analyze” category, we adopted a 2-stage approach to screening our data for analyzability at SLO. In the first stage, we simply screen for $\text{Fit} < 75\%$. Based on the distribution of Fit (Figure 6.22 bottom), this threshold classified approximately 4% of all targets as “Cannot Analyze”. The threshold (75%) is purposefully set to a level that is perhaps lower than our confidence in the data. However, in a second stage, we apply a figure of merit function that “penalizes” the output of our ANN for low levels of the Fit parameter. Likewise, we apply the same Figure of Merit (FOM) function to output metric from our library matching algorithm.

Figure of Merit Penalty Function (M_a)

In section 6.4.2, we introduced the FOM without explicitly defining it. We assume that the target is isolated from adjacent targets so that the secondary fields we measure are primarily due to the target of interest. Generally speaking, when the SNR is sufficiently high, the MetalMapper data acquired over an isolated target will always provide useful parameters and the Fit statistic will be greater than 85%. A data set with a high SNR and a low Fit statistic (i.e. <<85%) suggests that the field is not analyzable. Our figure-of-merit function (M_a) combines SNR and Fit into a parametric function defined by three parameters (snr_0, a, b). The mathematical formula we use is

$$M_a(snr, fit; snr_0, a, b) \equiv f(snr; snr_0)g(fit; a, b)$$

Where,

$$f(snr; snr_0) = \text{Max} \left[0.1 + \text{Min} \left[0, \log_{10} \left(\frac{snr}{snr_0} \right) \right] \right] \quad (6.3)$$

$$g(fit; a, b) = \frac{1}{1 + e^{(\frac{100-fit}{a}-b)}}$$

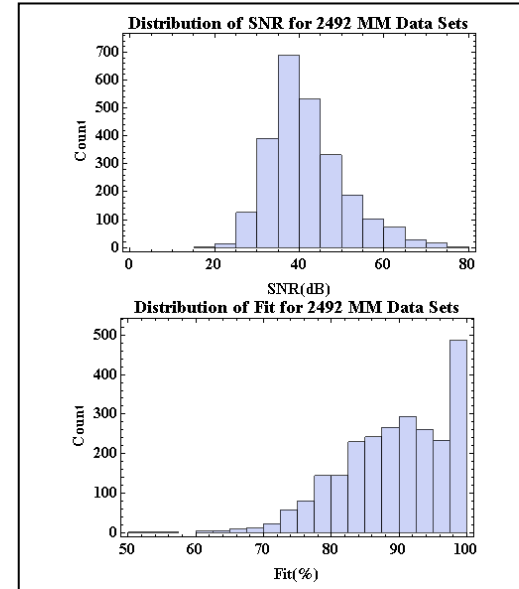


Figure 6.22: Histograms showing the distribution of SNR and Fit statistic for 2492 MM static files acquired at SLO.

We used data sets and ground-truth from the calibration lanes at both YPG and APG to determine that analyzability of target parameters from data sets with an SNR less than 10 and/or a Fit statistic of less than 90% fall off rapidly. The values for the 3-parameter analyzability function (equation 6.3) have been chosen by analyzing MM data sets from the calibration lanes at the Standardized UXO Technology Demonstration Site(s) located at YPG and APG. These values are provided below. The behavior of the 2 functions for the parameter values we used at SLO shown in Figure 6.23: Plots showing the figure of merit functions defined in equation (3-1) for the parameter values in Table 3-1. As we show in Figure 6.21, the penalty function is applied as a

Table 6.3: Parameter values for figure of merit function M_a

Parameter	Value
snr_0	20
a	2.5
b	8

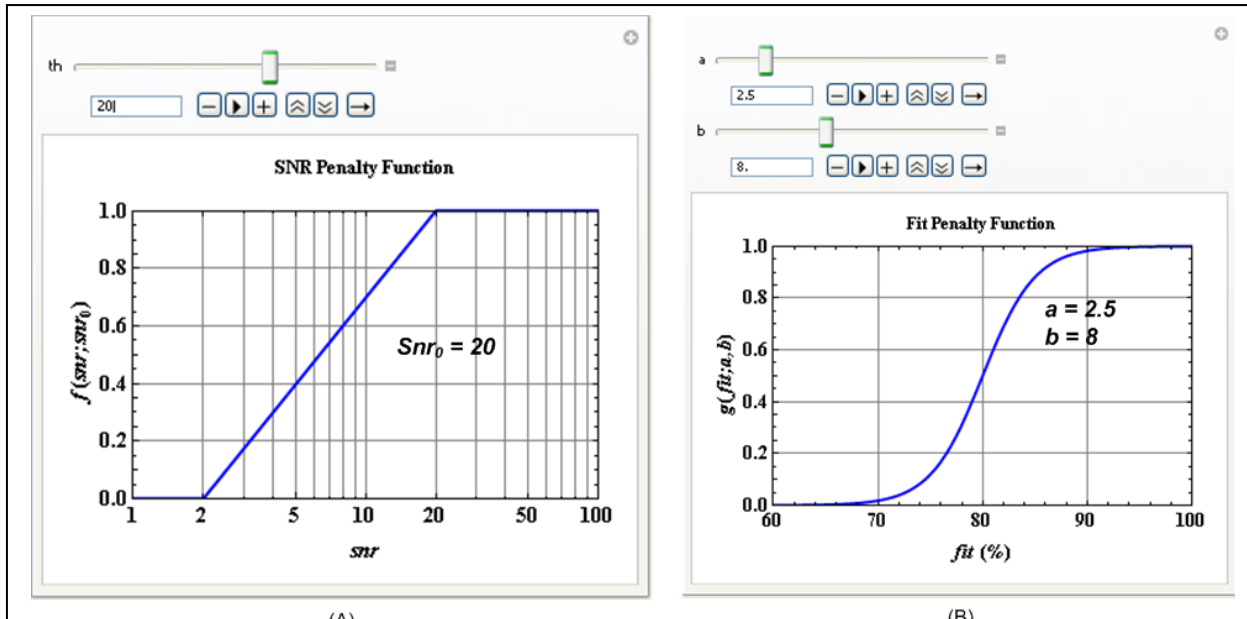


Figure 6.23: Plots showing the figure of merit functions defined in equation (3-1) for the parameter values in Table 3-1.

multiplier to the outputs of the ANN. While not changing the classification, the function decreases the confidence level for each of the classes. Thus, all targets with a fit value substantially lower than 85% will have low confidence and can be screened using two thresholds (T_{cl} , and T_0). Targets falling within these boundaries are designated as “*Ambiguous*” (i.e., Analyzable – Can’t Decide).

We have calculated the cumulative number of data points as a function of Fit using all 2492 static points that we measured at SLO and plotted the results together with the Fit histogram (Figure 3.1) in Figure 3.3. If we use a cut-off value of 75% below which all points are declared as “*Cannot Analyze-Must Dig*”, 111 data points (~4.5%) will be excluded.

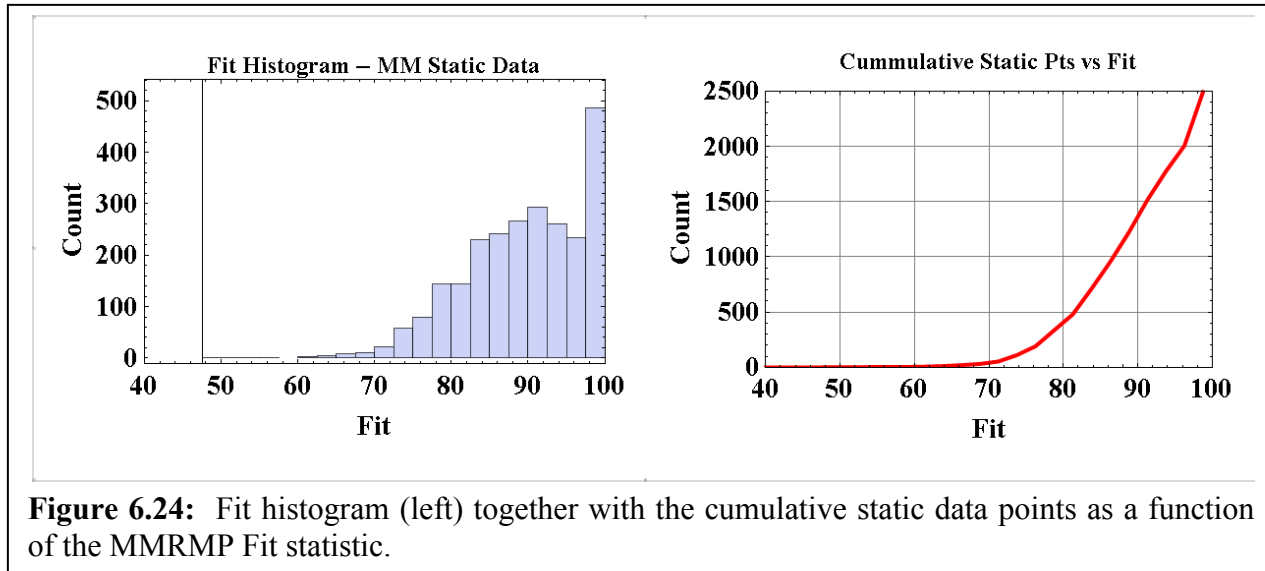


Figure 6.24: Fit histogram (left) together with the cumulative static data points as a function of the MMRMP Fit statistic.

Target Size

As a result of initial reconnaissance at the SLO demonstration site, the ESTCP program office identified 4 targets of primary interest. Those targets were the 2.36-in “Bazooka” rocket, 60mm mortar, 81mm mortar, and 4.2 in mortar. Our static measurements over specimens of these 4 targets in the test pit and in the test lanes at SLO have provided us with 14 test data sets for each of these targets at different depths and attitudes. From the target parameters we have extracted from these data sets, we estimated a threshold target size such that any target that has been placed in the ***Can Analyze*** category whose electromagnetic size (i.e., P_0) falls below $P_{0\min}$ falls into the category of high-confidence not munition (i.e., “clutter”). From the training data acquired in the test pit, the test strip, and the training dig, we have determined the minimum value of P_{0x} based on measured statistics of P_0 -values for each of the 4 TOI. Table 6.4 summarizes these statistics. The table also contains the static P_{0x} values observed over 3 additional targets, a 5-in rocket, a 3-in (Stokes) mortar, and a 37mm projectile that were found during subsequent digging (shaded grey in the table). There are no statistics for these targets because only one instance of each type has thus far been identified. Figure 6.25 is a graphic that summarizes the distribution of polarizability for the static data measured over the TOI included in the Training Dig (6.25A & 6.25C) and over targets placed in the test pit and buried in the test strip at SLO (6.25B & 6.25D). Figures 6.25A and 6.25C summarize results for approximately 200 targets excavated at SLO for which the ground-truth was released to demonstrators for use as training data. For reference, we have generated scatter plots in Figures 6.25B and 6.25D that contain only results measured in the test pit and test strip. The statistics were developed in log space and, therefore, the corresponding values in linear space are the “*Geometric Mean*” and the “*Geometric Standard Deviation*”. The “hi/lo” values in the table are estimates for a 95%

Table 6.4: Table summarizing the statistics of the 4 MOI’s of interest at SLO. We use this table to define the range of target sizes that may be munitions.

Target	P0x (Test Pit & Strip)				P0x (Training Dig)			
	GM	GSD	Hi	Lo	GM	GSD	Hi	Lo
2.36-in Rocket	5159	0.133	9419	2825	3617	0.326	15751	831
4.2-in Mortar	19546	0.076	27531	13877	19505	0.084	28496	13351
81mm Mortar	6067	0.107	9817	3751	7168	0.029	8170	6289
60mm Mortar	2585	0.050	3241	2062	1534	0.114	2566	917
5-in Rocket					3612	N/A	N/A	N/A
3-in Mortar					1259	N/A	N/A	N/A
37mm Mortar					615	N/A	N/A	N/A

Comments:

GM Geometric Mean
 GSD Geometric Standard Deviation
 Hi Expected high value (95% confidence)
 Lo Expected low value (95% confidence)
 Units All values in units of cm^3

confidence interval assuming a lognormal distribution. Based on the hi/lo values of the 4 TOI in Table 6.4 for the P_{0x} parameter²⁰ we set our decision rule for size based on P_{0x} values for all TOI staying in the range $500 \leq P_{0x} \leq 55,000$. The 37mm projectile has a P_{0x} that is uncomfortably close to the lower limit of our target size range. Further work at SLO will require a change to the lower limit of the size range (perhaps $P_{0xmin}=400$) and a recalculation of detection thresholds using 37mm mortar. In establishing this range, we set the minimum value

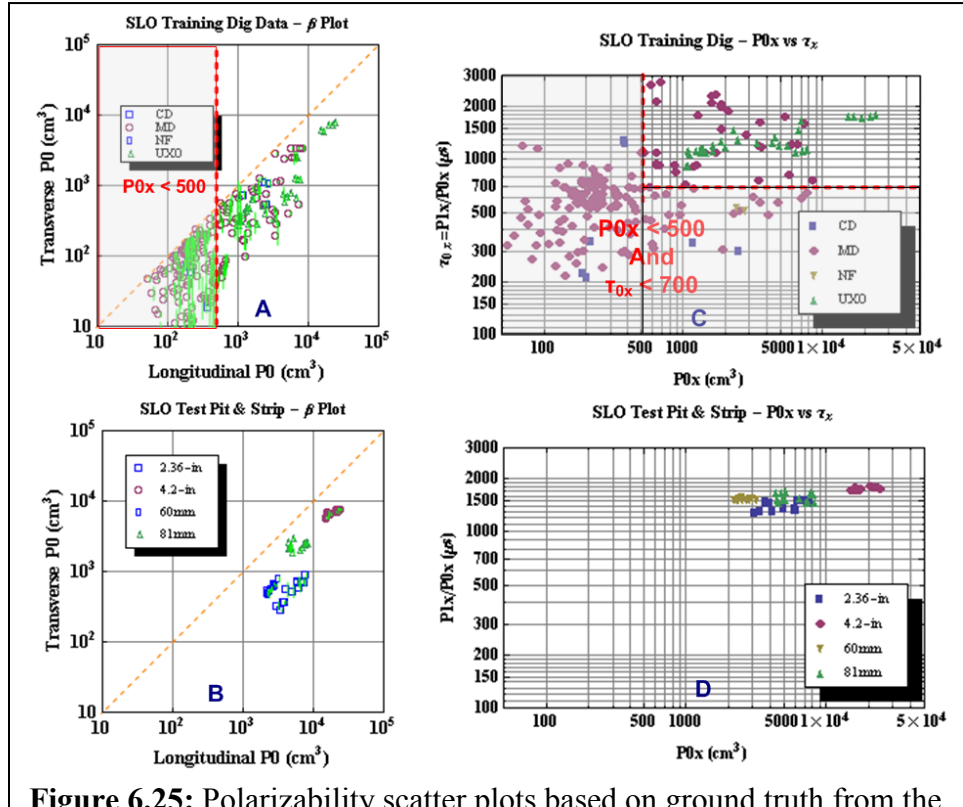


Figure 6.25: Polarizability scatter plots based on ground truth from the training dig (Top – 177 targets) and training data from the test pit and test strip at SLO (67 targets). The vertical bars (green) represent the parameter P_{0E} . Targets with large P_{0E} do not exhibit an axis of symmetry that is generally associated with ordnance items

to be substantially below the “lo” value for P_{0x} for the 60mm mortar (and 2.36-in rocket pieces that were classified as “TOI”) and the high value at twice (2 x) the “hi” value of the 4.2-in mortar. Targets falling outside this target size range were classified as “**High-Confidence Not Munitions**”.

²⁰ We chose P_{0x} because it is the largest and most reliable of the 3 scalar principal polarizability (“betas”) estimates.

Target Types for Library Matching

Initial reconnaissance dig information, later buttressed by results from the training dig, identified 4 targets of primary interest. Consequently, the ESTCP and the MetalMapper demonstration plans provided for the acquisition of static data over specimen targets of those types. And, as we mentioned in the previous section, it was not until after the training dig was completed and those results had been distributed that digging unearthed other munitions types (e.g., 3-in Stokes mortar, 37mm projectile, and 5-in Rocket). We developed our initial “type” polarizability curve library from the static measurements we acquired with the MetalMapper in the test pit and the test strip. Using, the specimen targets provided at SLO we measured the free-air response of each target placed at 4 different attitudes and 2 different depths. In addition, we took static measurements over each of the targets buried in the test strip several times during the course of our demonstration. In total, we were able to collect 14 independent data sets for each of the 4 static target types. The principal polarizability curves for each of the 4 type ensembles are shown in Figure 6.26. As a result of the training dig, we learned that the 60mm mortars that we unearthed often had neither the fuses nor the fins that were present on the specimen that we used for test pit measurements and on those that were buried in the test strip. The differences in the principal polarizability curves for the two types of 60mm targets can be seen in the average principal polarizability curves shown Figure 6.27. The 60mm types with no fins and fuses

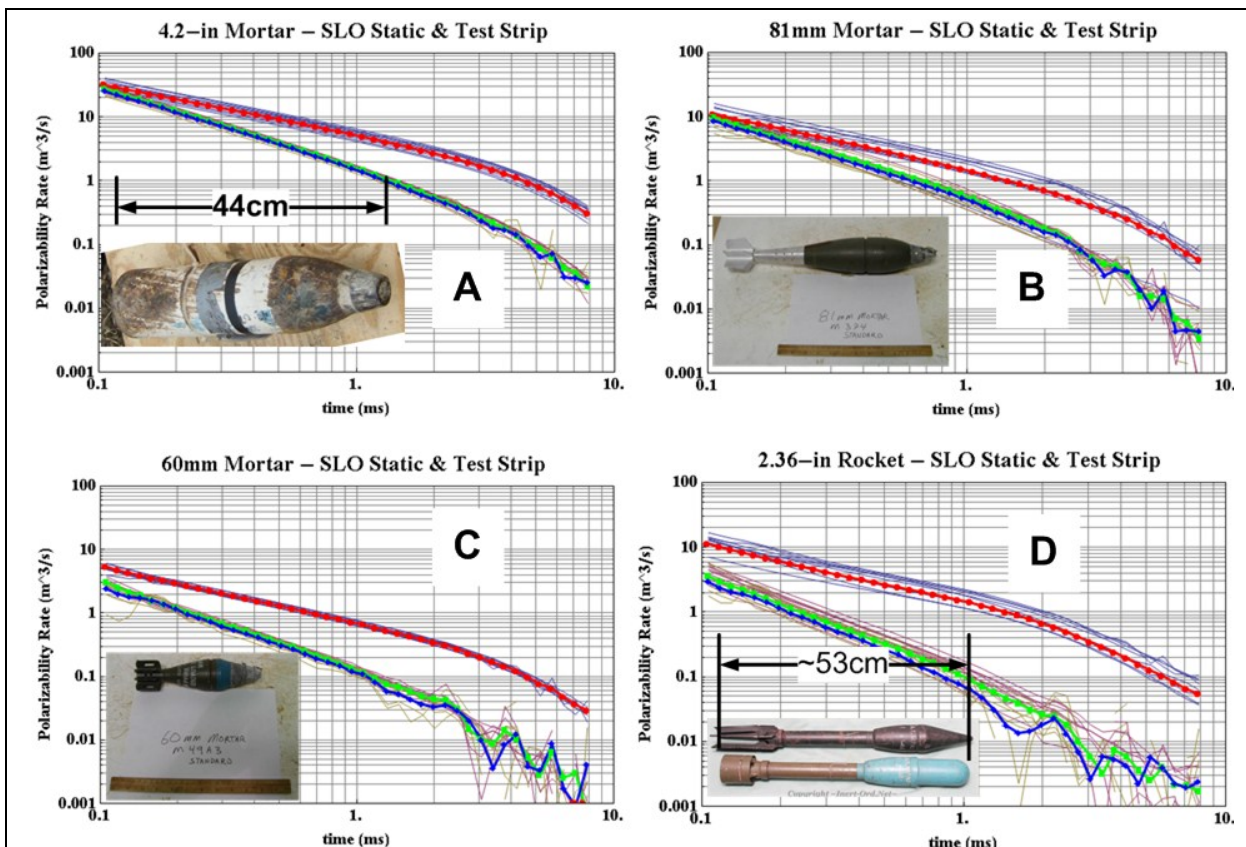
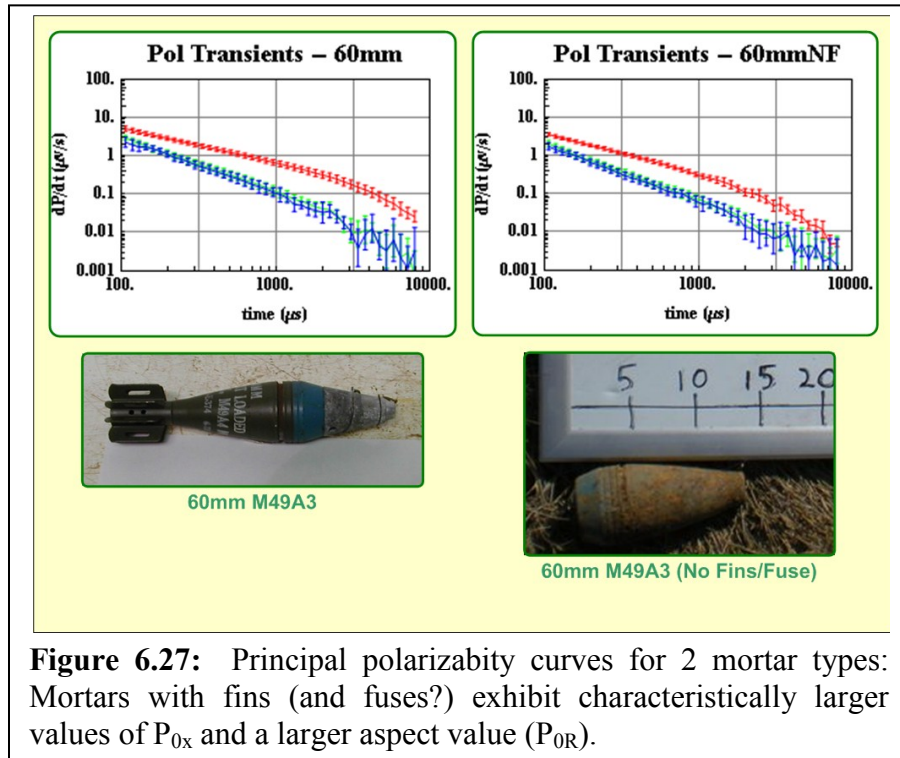


Figure 6.26: Principal polarizability curves for the 4 munitions of primary interest at SLO. Each curve set is derived from an ensemble of 14 static measurements over targets at different depths and orientations. The heavy curves (red/green/blue) are the geometric mean curves computed by taking the geometric mean of their respective ensemble.

exhibit a smaller aspect ratio P_R at later time. In the scalar features, this manifests itself primarily in smaller values for the two moments (P_{0x} , and P_{1x}) and in the aspect ratio parameter P_{0R} . Mortars with fins often exhibit a size as indicated by the feature P_{0x} that is twice that of a mortar without fins and a fuse. During the training dig at SLO, the excavated 60mm mortars were mostly ones without fins and fuses. To insure that our library matching algorithm recognized both types of 60mm mortars, we included both type curves for both configurations of the 60mm mortars in our library.



Artificial Neural Net (ANN) Classifier

The introduction of an ANN to generate a binary decision regarding whether a particular target is a target of interest represents the most significant change our classification procedure. For this purpose, we used the commercially available software package Statistica version 6.0/9.0. We analyzed scalar polarizability parameters extracted from static MM data sets collected over 2,177 targets. The 23 polarizability parameters we examined are listed in Table 6.5.²¹

Table 6.5: Table of scalar target parameters extracted from static data sets acquired with the MetalMapper

P0x	P0y	P0z	NormP0	P0T	P0R	P0E
P1x	P1y	P1z	NormP1	P1T	P1R	P1E
K1x	Gamma1x	K1y	Gamma1y	K1z	Gamma1z	
P1x/P0x	P1y/P0y	P1z/P0z				

Our objective was to combine a basic statistical analysis of the data with expert knowledge about the data and the ANN choice of parameters to select a subset of parameters to use for the ANN analysis. Input parameters should be selected to provide the best separation between clutter and TOI signatures. In order to keep the number of connection weights in the ANN small, we want to identify the smallest set of input parameters that can provide effective classification.

We visually classified 2,177 targets as UXO or clutter. This was a rough classification so the statistics for the two categories no doubt included some incorrectly classified targets. The statistics for TOI are shown in Table 6.6 and for clutter in **Table 6.7**. There is good separation of the mean for each parameter in the two classes and there is little overlap of minimum and maximum values of each parameter between classes. Next we look at the correlation of parameters. Ideally we want parameters that are not correlated with each other as input parameters as they are redundant.

²¹ See 6.3 for definitions. The P0 parameters represent the 0th moment of the respective component of the principal polarizability transients. Likewise, the P1 parameters represent the first moment in of the principal polarizability transient. K1, and Gamma1 are parameters arising from the parametric fit of equation 6.1 to a polarizability transient.

Table 6.6: TOI Statistics

Variable	Descriptive Statistics (TEM_Edited_AllSections_Test_wOutp)				
	Valid N	Mean	Minimum	Maximum	Std.Dev.
P0X	315	9620	43.6	907142	51360
P0Y	315	3315	25.3	356674	20182
P0Z	315	2855	21.8	263770	14992
NormP0	315	10612	61.6	1009801	57175
P0_T	315	3085	24.9	310222	17584
P0_R	315	4	1.2	19	3
P0_E	315	0	0.0	0	0
P1X	315	12796980	13806.9	732048528	43005289
P1Y	315	2674054	-1426.4	238871126	13638109
P1Z	315	2325361	-10441.2	193343618	11089878
NormP1	315	13331739	16603.9	793937162	46443719
P1_T	315	2499708	2161.9	216107372	12362255
P1_R	315	8	1.2	178	12
P1_E	315	0	-0.4	0	0
K1x	315	17009	0.0	1000000	57441
gamma1X	315	161246	0.0	10000000	1251515
K1y	315	13610	131.1	1000000	57044
gamma1Y	315	2101627	634.0	10000000	4073333
K1z	315	12827	97.5	862810	49486
gamma1Z	315	2352410	0.9	10000000	4244463
P1x/P0x	315	1237	271.7	2323	441
P1y/P0y	315	723	-30.7	1144	194
P1z/P0z	315	681	-33.5	1494	221

Table 6.7: Clutter statistics

Variable	Descriptive Statistics (TEM_Edited_AllSections_Test_wOutput)				
	Valid N	Mean	Minimum	Maximum	Std.Dev.
P0X	1862	1429	13	1.430998E+06	33733
P0Y	1862	819	1	8.271481E+05	19635
P0Z	1862	472	0	4.301327E+05	10272
NormP0	1862	1730	16	1.707906E+06	40360
P0_T	1862	646	1	6.286404E+05	14952
P0_R	1862	4	1	5.013927E+01	4
P0_E	1862	0	0	8.718334E-01	0
P1X	1862	1205184	-59510	1.157193E+09	27649922
P1Y	1862	544935	-433417	5.325576E+08	12884785
P1Z	1862	307480	-1355761	3.008459E+08	7211944
NormP1	1862	1375617	3599	1.308901E+09	31344850
P1_T	1862	426207	-545712	4.167018E+08	10045979
P1_R	1862	5	-340	4.233777E+02	20
P1_E	1862	0	-35	1.943966E+01	1
K1x	1862	4497	15	1.000000E+06	31990
gamma1X	1862	1545149	175	1.000000E+07	3610199
K1y	1862	3706	6	1.000000E+06	30333
gamma1Y	1862	3756215	260	1.000000E+07	4836931
K1z	1862	3208	0	1.000000E+06	28577
gamma1Z	1862	4034866	0	1.000000E+07	4900366
P1x/P0x	1862	572	-372	2.743929E+03	320
P1y/P0y	1862	473	-13619	1.946209E+03	511
P1z/P0z	1862	692	-21772	1.830876E+05	5651

For clutter targets, P0X is highly correlated with P0Y, P0Z, NormP0, P0_T, P1X, P1Y, P1Z, NormP1, K1x, K1y, and K1z. The parameters P0_R, P0_E, P1_R, P1_E, γ1x, γ1y, γ1z, P1x/P0x, P1y/P0y, and P1z/P0z are not correlated with other parameters.

Table 6.8: Correlation matrix for the 9 scalar parameters (features) selected for use in discrimination at SLO.

Variable	Correlations (TEM_Edited_AllSections_Test_wOutput)								
	P0X	P0Y	P0Z	P0_R	P0_E	P1_E	P1x/P0x	P1y/P0y	P1z/P0z
P0X	1.00	0.99	1.00	-0.01	-0.01	-0.00	0.07	0.03	0.00
P0Y	0.99	1.00	0.99	-0.02	0.01	0.00	0.05	0.03	0.00
P0Z	1.00	0.99	1.00	-0.02	-0.00	-0.00	0.08	0.03	0.00
P0_R	-0.01	-0.02	-0.02	1.00	-0.32	-0.03	0.07	-0.12	0.12
P0_E	-0.01	0.01	-0.00	-0.32	1.00	0.15	-0.34	-0.01	0.00
P1_E	-0.00	0.00	-0.00	-0.03	0.15	1.00	-0.02	0.03	-0.03
P1x/P0x	0.07	0.05	0.08	0.07	-0.34	-0.02	1.00	0.32	0.00
P1y/P0y	0.03	0.03	0.03	-0.12	-0.01	0.03	0.32	1.00	0.01
P1z/P0z	0.00	0.00	0.00	0.12	0.00	-0.03	0.00	0.01	1.00

The selection of parameters for the ANN is dependent on the total number of parameters and the quality of the training data and is not unique. We ran a hierarchical classification tree, discriminant analysis, and 4 ANNs. For each ANN, we looked at the sensitivity of the classification to the input parameters. The list below (Table 6.9) indicates in how many of the trials each parameter was selected as important (total of 6 trials):

Table 6.9: Results of ANN (and other) parameter selection

Param	Sel Cnt	Param	Sel Cnt	Param	Sel Cnt	Param	Sel Cnt
P0x	2	P1x	0	K1x	3	Gamma1x	1
P0y	0	P1y	0	K1y	2	Gamma1y	2
P0z	0	P1z	0	K1z	3	Gamma1z	2
NormP0	0	NormP1	1	P1x/P0x	5		
POT	0	P1T	0	P1y/P0y	4		
POR	3	P1R	2	P1z/P0z	3		
POE	6	P1E	4				

Using parameters that were selected at least twice in our analyses, the input parameter set (feature vector) would be:

(P0x, P0R, POE, P1R, P1E, K1x, K1y, γ1y, K1z, γ1z, P1x/P0x, P1y/P0y, P1z/P0z)

The various K1 and γ parameters are derived from the fit of their respective principal polarizability curves with a parametric relation (equation 6.1). The K and γ parameters have the same units and, indeed, the same physical meaning (i.e., target size, and time decay) as their more robust counterparts (P0, and P1/P0), which are calculated by simple numerical integration and ratios. Therefore, we eliminated K's and γ 's from our list of features where they provide redundant information (e.g. K1x~P0x; γ 1z~P1z/P0z,etc) and have substituted P0y for K1y, and P0z for K1z. Our final feature vector includes 9 robust parameters that capture (in scalar form) the properties of target size (P0 – 3 axes), target aspect (P0_R), target symmetry (P0_E), and target polarizability time persistence (P1/P0 – 3 axes):

(P0x, P0y, P0z, P0R, POE, P1E, P1x/P0x, P1y/P0y, P1z/P0z)

In our initial experimentation, the only training data we had were those that we acquired in the test pit and over the test strip. Therefore, we selected targets to use as training data by visual inspection of all the target data with the goal of selecting clear examples of the 4 types of UXO together with representative clutter. The resulting training set contained more examples of clutter than UXO because there is more variability in the clutter. We chose 257 examples of clutter and 165 examples of UXO. There were at least 76 targets that we classed as clutter based on P0x amplitude ($<500 \text{ cm}^3$) but which had good symmetry. Based on our visual classification we found 315 TOI and 1,862 clutter. Thus we used approximately 52% of the UXO examples and 14% of the clutter in our training set.

After the results of the training dig were distributed to those involved in the classification processing, we had (barely) sufficient data (when added to the test pit and test strip) so that we were able to train a network totally on data for which the ground truth was known.²²

ANN - We used a feed-forward multi-layer perceptron architecture with backpropagation and quasi-Newton training algorithms. We ran backpropagation for 55 epochs and then switched to quasi-Newton for 20 epochs. Backpropagation is a fast algorithm but often has trouble converging to the minimum. Quasi-Newton is computationally more intensive and needs to run when we are closer to the minimum. Hence, we use backpropagation to get close to the minimum error and then quasi-Newton for the final few epochs. Input parameters were linearly scaled to a range of [-1,1] by taking the minimum and maximum value for each parameter and scaling that range to the ANN input range. We used a starting step size of 0.02 and momentum of 0.4. The step size and momentum were automatically adjusted each epoch with a final step size of 0.1, and a final momentum of 0.3. We had 9 input parameters, 1 hidden layer with 6 hidden nodes, and 1 output. We used a hyperbolic tangent activation function for the hidden layer and a logistic activation function for the output. We used an entropy calculation to determine the output error during training. This error is the sum of the products of the target value and the logarithm of the error value on each output unit.

The output was coded as 0 for clutter and 1 for TOI. We set a threshold of 0.5 and all outputs less than 0.5 were classed as clutter and those greater than 0.5 were UXO. The closer an output is to 0 the more confidence we have in the clutter classification and the closer the output is to 1, the more confidence we have in the UXO classification.

Statistica randomly selects half of targets for training, a quarter for “selection”, and a quarter for testing. The samples are chosen to have similar means, ranges, and standard deviations. The training samples are used to adjust the connection weights. Periodically the weights are frozen and the selection targets are passed through the network once and their outputs are compared with their desired output. This is done to monitor for overtraining. The training process can proceed until all training samples are learned perfectly but this runs the risk of learning noise or irrelevant information in the data and the resulting network will not generalize or test well. We monitor the training and selection error to make sure that they track each other. If the training error is improving and the selection error degrades, we have over trained and must return to the best previous network configuration. Once we have the “best” network, the weights are frozen and the test data are presented to the network. We monitor the training, selection, and test errors.

Classification Results – Training & Test

As we indicated above, we ended up training two networks:

1. **ANN Network 1:** This ANN was trained with test pit and test strip data (58 data points), data from the test dig (208 points), and 12 data points that were visually classified as 60mmNF (No Fins). Although we had MM static points associated with only 154 of the targets in the training dig, many of those targets had 2 or more MM data points associated

²² The program office allowed us to submit a target list resulting from the two ANN’s (i.e., one trained with known data only, and one trained with a training set “augmented” with visually classified data points.

with the target. By using these (54) repeated data points, we “augmented” our training set so that it had 278 targets.

2. **ANN Network 2:** This ANN was trained with a total of 563 targets comprised of the 58 points from the test pit and test strip, the 208 points (as above) from the training dig, and 296 points that were visually classified.

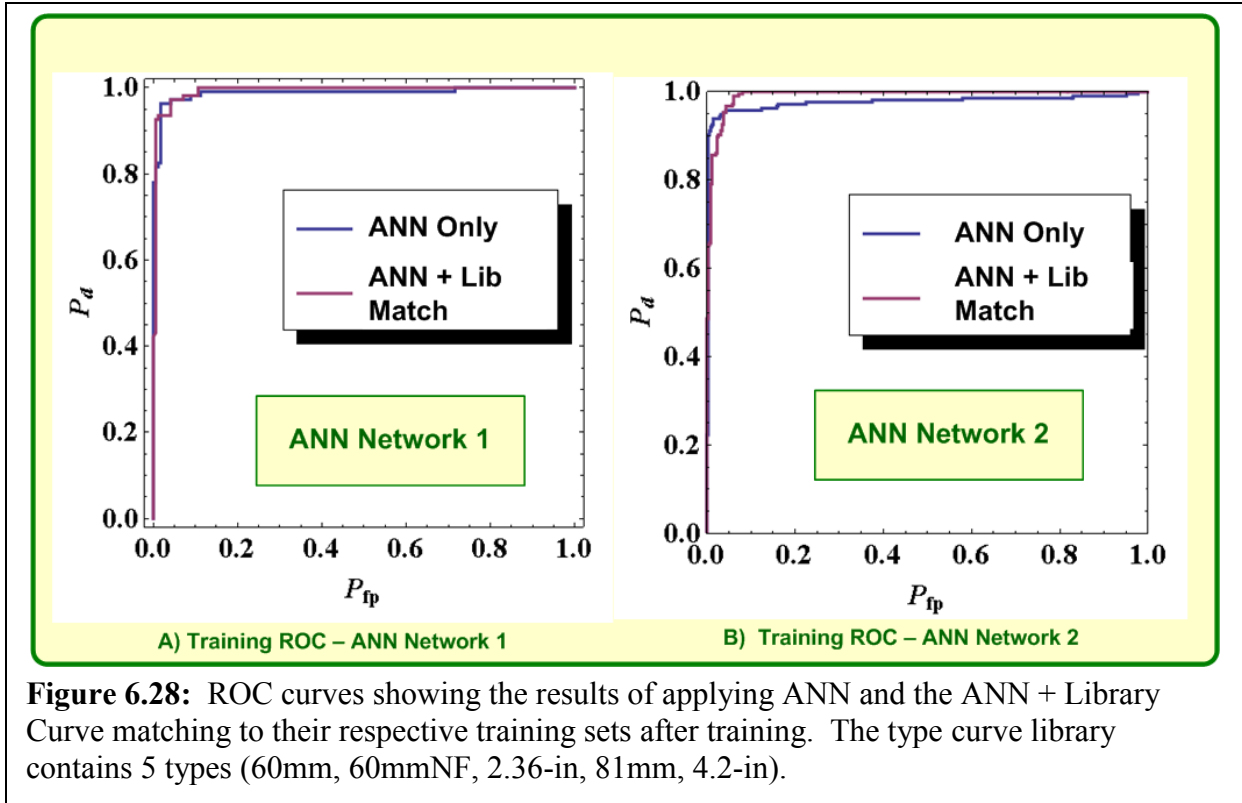


Figure 6.28: ROC curves showing the results of applying ANN and the ANN + Library Curve matching to their respective training sets after training. The type curve library contains 5 types (60mm, 60mmNF, 2.36-in, 81mm, 4.2-in).

Figure 6.28 shows the ROC curves that result from applying the two ANN's to their respective training data. Note that in both cases, the ANN leaves a few “hard” false negatives that would require us to dig a high percentage of all the targets before digging the last TOI. However, after applying the library matching, the hard false negatives are moved closer to the knee (operating point) of the curve thereby dramatically reducing the number of targets we need to dig before we dig the last TOI (100% detection point).

It is interesting to look at the decision surfaces generated by the ANN only and then how it's modified by applying library matching. In Figure 6.30, we overlay a contour plot of the decision metric on top of a categorized beta plot. The categories here are “TOI” (blue squares) and “Clutter” (magenta diamonds). In these plots, we have emphasized our decision threshold with a dashed yellow line. Lighter shaded areas reflect areas where $P_d > 0.5$ and hence the points are more probably “TOI”. The darker areas indicate $P_d < 0.5$ and hence points in these areas are more likely to be “Clutter”. In the ANN Only plot (Figure 6.30 left - center), notice that there are many TOI falling on or near the decision threshold indicating that many of the decisions are either ambiguous or even worse are declared clutter (i.e., false negatives). Most of those points represent targets with the type “60mmNF” (60mm mortars with no fins and fuses). After applying library matching, the decision boundary is moved so that the targets in question are

more firmly on the “TOI” side (Figure 6.30 right). Overall, the differences are minor. However, the benefit of using library matching is that it reduces the number of false negatives.

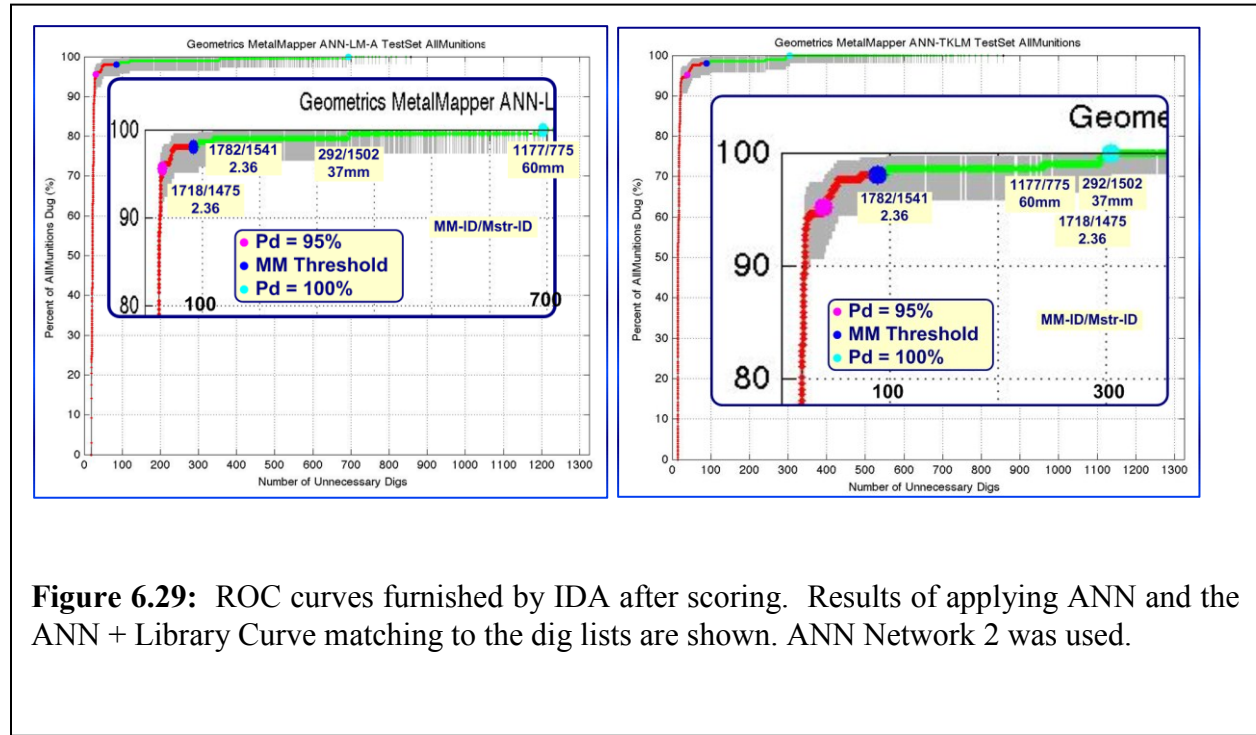


Figure 6.29: ROC curves furnished by IDA after scoring. Results of applying ANN and the ANN + Library Curve matching to the dig lists are shown. ANN Network 2 was used.

Figure 6.29 shows the ROC curves furnished to us by the IDA after scoring the two target lists that we submitted. Note that panels A) and B) of the training ROC curves each have two ROC curves. The curve labeled “ANN Only” reflects the scoring based on the ANN output only. The 2nd curve (labeled “ANN + Lib Matching”) reflects an adjustment of the discrimination scores based on the output from the library curve matching algorithm. The library curve matching clearly identifies most of the false negatives and changes their discrimination score so that in the final list they usually fall on the high side of the operating point (nominally 0.5).

Both of ANN’s yield results that very quickly reach a value of Pd=95%. Network 1 (Figure 6.28A) has a few false negatives bunched together near the operating point. However, there are two pathological false negatives occurring at approximately 350 and 700 digs (Figure 6.29A) and at 250 and 300 digs, respectively, for Networks 1 and 2. These data points arise from 2.36-in rocket parts. The difference between the relative positions in each dig list reflects the ANN scores. Network 1 indicates a higher probability that the targets are clutter than does Network 2. The library curve matching in both cases is no help since in both cases the polarizability curves exhibit clutter-like properties (Figure 6.31).

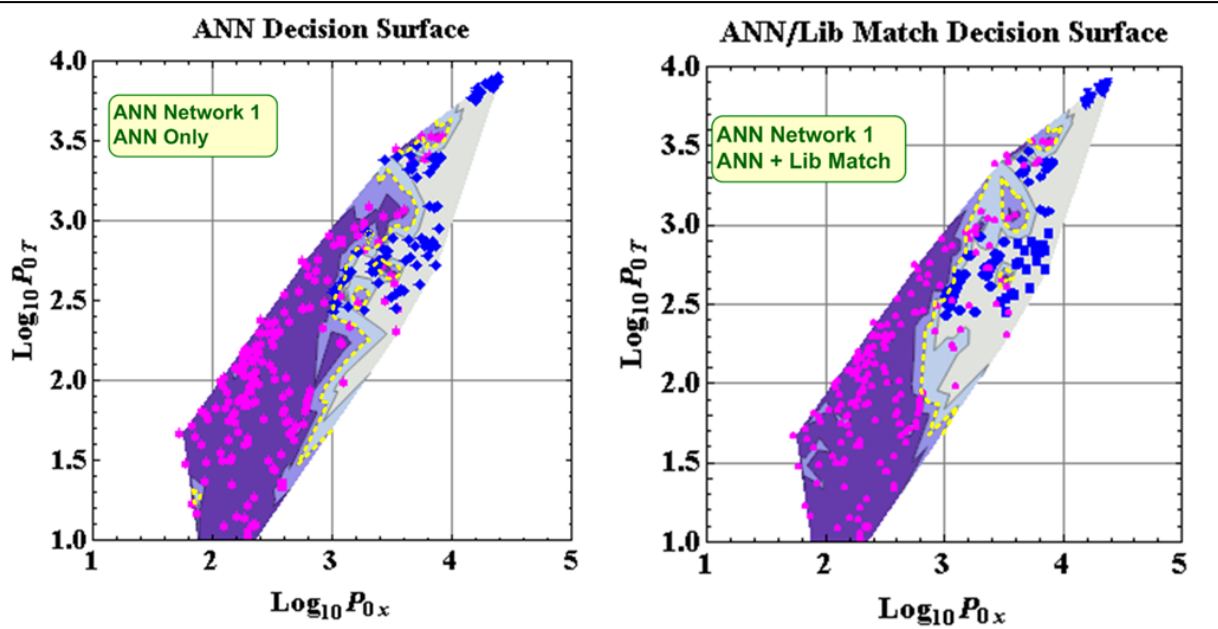


Figure 6.30: Categorized “beta” plots overlaid with a contour plot of the ANN only (left) and ANN plus Library Matching (right) decision surface. The decision threshold contour line (dashed yellow)

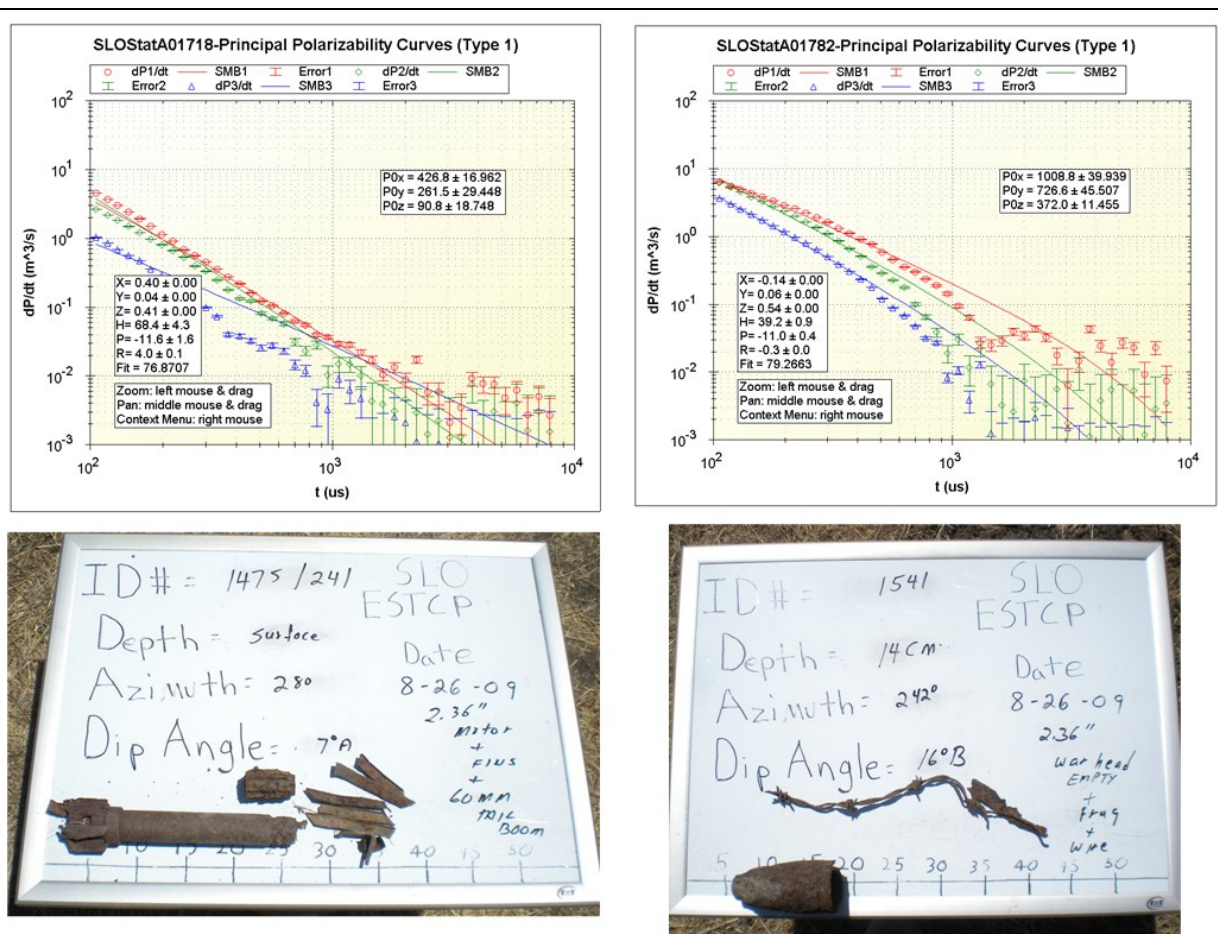


Figure 6.31: Polarizability curves and dig photos for 2 targets in the MM target list. Both targets were classified as “Clutter” with relatively unambiguous scores.

6.5. DATA PRODUCTS

As suggested by the flow diagrams in Figure 6.17 and Figure 6.21, the principal data product arising from the processing is a prioritized dig list which can be scored against ground-truth. We have tried to emphasize throughout this section that our procedures and ability to construct a prioritized dig list have evolved during the course of the three demonstrations we have conducted and have reported on here. Indeed, the SLO demonstration has led us to develop and document each step in the classification process.

While the prioritized dig list is the primary product of the demonstrations, there are also many other data products required in order to adequately document and measure the performance of the MetalMapper against the various performance objectives that we have enumerated in Section 3.

7. PERFORMANCE ASSESSMENT

In this section we will assess the performance of the MetalMapper system against the performance objectives contained in Table 3.1. So as to avoid needless duplication, we will introduce results from YPG and/or APG where appropriate. Quite apart from whether we met our performance goals at APG, the performance measures from previous demonstrations provide useful benchmarks that demonstrate improvement in our ability to efficiently acquire high-quality data effectively interpret them.

7.1. SITE COVERAGE

At both APG and SLO, we ran our dynamic surveys using a profile offset of 0.75m. We were able to meet the “tight” 0.75m line specification for the SLO detection survey by processing our profile data into “split-cube” profiles wherein each MetalMapper profile becomes 7 split-cube profiles with 13cm offsets.

For convenience in processing and data QC/QA, we divided the survey area into 13 sub-areas. Those sub-areas are identified in Figure 6.4 and again in Figure 7.1. In Figure 7.1 we have zoomed in on a 6-block area so that the reader can see some detail on the profiles. To be sure, there are some “gaps” in the coverage. However, gaps such as we see near the SW corner of block M7 and the center of N7 reflect the presence of obstacles (usually outcropping bedrock) that were impossible for the survey tractor to survey over.

7.1.1. GPS Data Quality

The site coverage performance objective (section 3.1) mentions spurious GPS positions. As part of our field QC, we always plot the profile tracks. However, the quality of the GPS fix is monitored in real time by the MetalMapper acquisition software and a visual alarm is shown on the acquisition display when that fix is no longer RTK quality. We suspend survey operations when the quality of the GPS fix is not RTK. Based on these 2 QC checks, we can say with the utmost confidence that our GPS positions contain virtually no spurious points or drop-outs.

Table 7.1: Summary of footprint coverage for the 13 sub-areas comprising the 11.8-acre (4.78 ha) SLO study area. The instrument footprint was assumed to be 0.75m.

Sub Area	% Coverage	Area (m²)	Area Covered
E	99.26%	6782.43	6732.15
NE	98.34%	5587.82	5495.06
NEa	98.72%	1611.35	1593.92
Nn	99.96%	3609.39	3608.04
Ns	98.65%	3642.05	3592.73
NWA	99.79%	1807.05	1803.17
NWB	98.32%	2719.86	2674.14
NWCa	99.95%	2593.71	2592.50
NWCb	98.46%	2807.85	2764.71
SA	99.51%	5398.66	5372.26
SWA	100.00%	2703.27	2703.27
SE-A	98.26%	4596.34	4516.18
SE	99.86%	3940.05	3934.73
<i>Totals</i>	99.13%	47799.83	47382.86

7.1.2. Area Coverage - SLO

To quantify the percentage of area covered by the MetalMapper, we used UCEFOOTPRINTCOV GX. We applied the GX using a 0.75m footprint to each of the 13 Geosoft split cube GDB's using a polygonal shape file that coincides with the sub-area under

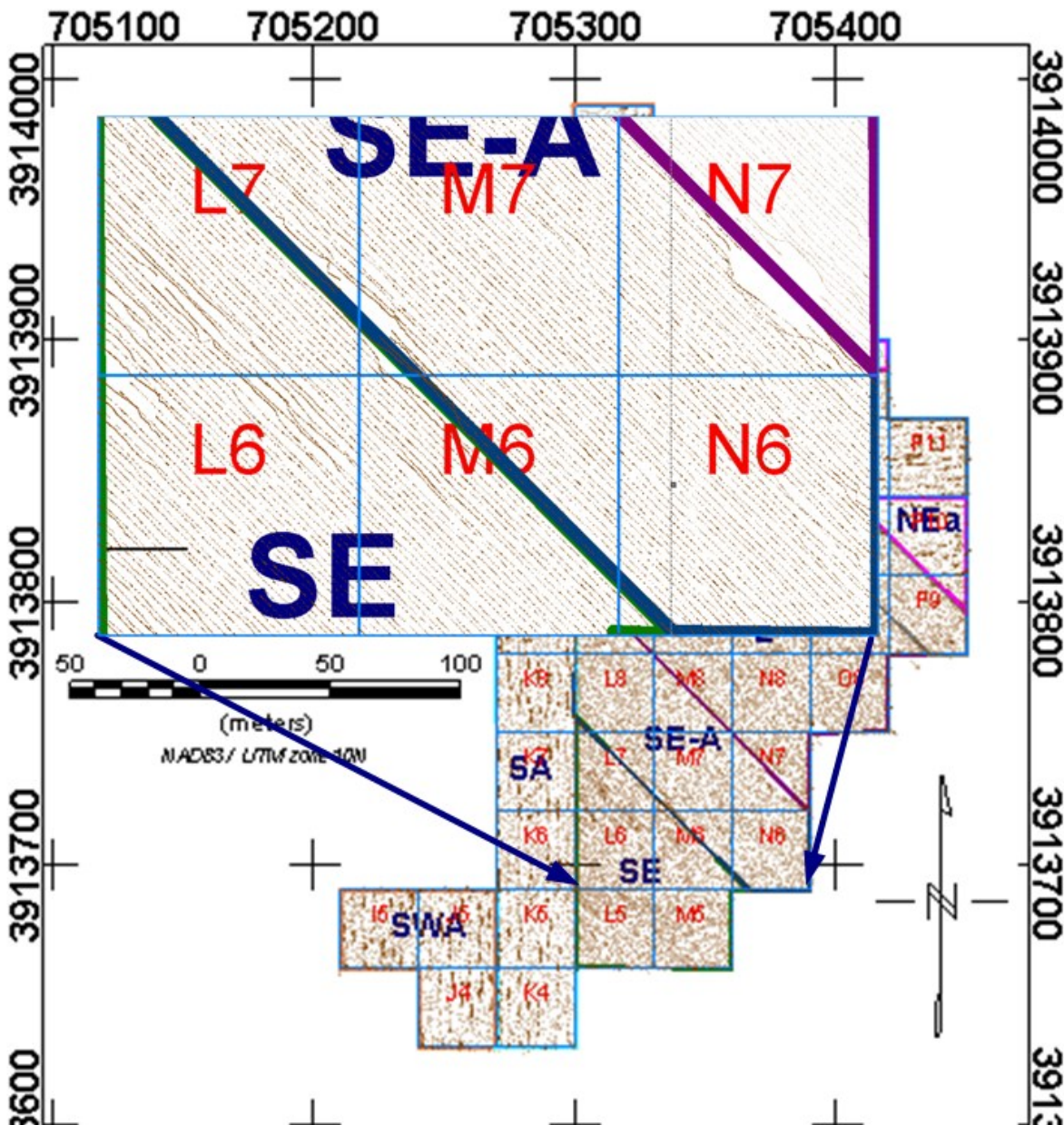


Figure 7.1: An index map showing the 53 survey blocks of the SLO study area. The study area was divided into 13 sub-areas. The brown shading is actually survey points. The inset shows the actual survey profiles for a small area. The plotted profiles are on 0.75m centers and represent the track of the MetalMapper survey platform.

investigation. The results from those 13 analyses are tabulated in Table 7.1. More than 99% of

the study area has been covered with no gaps greater than 0.75m. All of the areas that were not covered were inaccessible to our survey vehicle. We believe that these results show that the MetalMapper has substantially met the objective in Table 3.1 for survey coverage.

7.1.3.

7.2. Repeatability of Test Strip Calibrations

7.2.1. Dynamic Calibrations

Figure 6.7 is a pseudo-map generated by compiling 60 repeated profiles over the test strip at SLO. These data were processed in exactly the same way as we processed the detection maps for the study area. All target picks shown on the map (yellow triangle symbols) were picked from the split cube grid using the GRIDPICK GX from Oasis Montaj. Because the test strip was not entirely clean prior to the seeding of the 10 targets (T-001 through T-010), it was necessary to delete many target picks. However, none of the remaining picks have been moved or adjusted. We ended up with a set of 59 points for each target. Each target pick consists of an X-Y coordinate point (in Local coordinates) plus a grid value. We have tabulated the means and

Table 7.2: Summary statistics for repeated surveys over the 10 targets seeded in the test strip at SLO. All position errors are given in meters. The peak amplitude values are in units of $\mu\text{T/s}$. Note that the local Y coordinate is along the survey track. The columns relevant to repeatability performance objectives are highlighted in blue.

Name	Type	Av _{ΔX}	$\sigma_{\Delta X}$	Av _{ΔY}	$\sigma_{\Delta Y}$	Config	Av _{Amp}	σ_{Amp}	σ_{Amp}	N
T-001	Shot put	-0.02	0.13	0.21	0.08	Wheels	26.47	5.85	22.1%	32
						Skids	69.56	13.23	19.0%	27
T-002	81mm_V	-0.24	0.08	-0.35	0.09	Wheels	23.65	3.79	16.0%	32
						Skids	58.42	10.60	18.1%	27
T-003	81mm_H	-0.01	0.09	-0.01	0.08	Wheels	11.33	1.33	11.7%	32
						Skids	26.37	5.24	19.9%	27
T-004	60mm_V	0.08	0.06	0.04	0.09	Wheels	9.69	1.91	19.7%	32
						Skids	20.68	6.36	30.7%	27
T-005	60mm_H	0.21	0.11	0.00	0.09	Wheels	3.88	0.95	24.4%	32
						Skids	8.16	2.90	35.5%	27
T-006	4.2-in_V	0.12	0.08	0.10	0.09	Wheels	61.24	16.99	27.7%	32
						Skids	143.99	32.00	22.2%	27
T-007	4.2-in_H	0.17	0.09	0.07	0.07	Wheels	38.76	8.40	21.7%	32
						Skids	82.27	20.10	24.4%	27
T-008	2.36-in_V	0.02	0.07	0.03	0.10	Wheels	25.78	7.14	27.7%	32
						Skids	59.78	17.57	29.4%	27
T-009	2.36-in_H	0.12	0.15	-0.05	0.07	Wheels	3.83	0.64	16.7%	32
						Skids	7.95	1.47	18.5%	27
T-010	Shot put	0.10	0.10	0.08	0.10	Wheels	12.47	2.80	22.4%	32
						Skids	25.59	8.97	35.1%	27

standard deviations of the cross-track (Local X) and the along track (Local Y) errors between the picked anomaly peak and the ground-truth for each target as provided to us in the ESTCP demonstration plan. In addition, we have computed the mean and standard deviations for the peak amplitudes. Recall that the dynamic survey was conducted using two configurations for the deployment of the MetalMapper antenna array: a) Skid-Mounted; and b) Wheel-Mounted. The height of the antenna array above ground level is 21cm and 29cm, respectively, for the skid-mounted and wheel-mounted deployments so it is necessary to report repeatability statistics for the peak amplitudes for each configuration. In Table 7.2, we have summarized the statistics using the split cube map (Figure 6.7) together with an automatic peak picker. The repeatability of the target coordinates is very good with standard deviations along track (Y) of 0.1m or less. Over some targets (e.g., T-002 the error has a bias of more than 0.1m (e.g., T-001 and T-002). We have no explanation as to why this bias (0.21m, and -0.35m). What is significant however is that the standard deviation in position error along track is well below the performance objective of 0.25m indicated in Table 3.1. The standard deviations of peak amplitudes with a few exceptions are below the performance standard of 25%. But we fail to meet the standard of 15% or less.

We tried an alternative method of compiling the repeatability statistics. Instead of compiling the

Table 7.3: Summary statistics for repeated surveys over the 10 targets seeded in the test strip at SLO. All position errors are given in meters. The peak amplitude values are in units of $\mu\text{T/s}$. These statistics are based on line by line picking of targets and more extensive editing than those shown in Table 7.2. The columns relevant to repeatability performance objectives are highlighted in blue.

Name	Type	Av_ΔE	σ_ΔE	Av_ΔN	σ_ΔN	Av_ΔY	σ_ΔY	Config	Av_Amp	σ_Amp	σ_Amp	N
T-001	Shot put	0.15	0.08	0.10	0.09	0.16	0.12	Wheels	24.95	5.88	23.55%	32
								Skids	65.75	12.44	18.92%	27
T-002	81mm_V	-0.31	0.09	-0.24	0.08	-0.37	0.12	Wheels	22.60	3.54	15.68%	32
								Skids	55.58	9.72	17.49%	27
T-003	81mm_H	0.07	0.08	-0.09	0.07	-0.04	0.11	Wheels	10.92	1.26	11.49%	32
								Skids	25.56	4.93	19.27%	27
T-004	60mm_V	0.18	0.08	-0.09	0.07	0.02	0.11	Wheels	9.31	1.75	18.77%	32
								Skids	19.73	6.01	30.49%	27
T-005	60mm_H	0.26	0.11	-0.17	0.12	0.00	0.15	Wheels	3.91	1.00	25.64%	32
								Skids	8.02	3.12	38.95%	27
T-006	4.2-in_V	0.26	0.10	-0.07	0.05	0.08	0.10	Wheels	58.12	16.08	27.67%	32
								Skids	137.08	29.64	21.63%	27
T-007	4.2-in_H	0.27	0.11	-0.12	0.05	0.05	0.10	Wheels	38.44	8.39	21.82%	32
								Skids	79.23	19.00	23.98%	27
T-008	2.36-in_V	0.15	0.08	-0.09	0.08	0.00	0.11	Wheels	24.40	6.36	26.05%	32
								Skids	55.87	16.21	29.02%	27
T-009	2.36-in_H	0.21	0.15	-0.20	0.10	-0.06	0.16	Wheels	3.78	0.63	16.64%	32
								Skids	7.68	1.47	19.09%	27
T-010	Shot put	0.31	0.11	-0.12	0.09	0.07	0.13	Wheels	12.06	2.95	24.44%	32
								Skids	25.78	8.41	32.61%	27

test strip data lines into a map (through the artifice of adding 1m to the x-coordinates of each successive lines, we compile each line into a separate map consisting of 7 (split-cube) lines. Then we used GRIDPEAK GX to pick the lines, followed by a manual edit to remove spurious picks and (in some cases) to move the target pick. With this method, it was much easier to edit the target picks to make sure they were all picking the same target. However, the process of picking had to be repeated 59 times and was time consuming. The results of that exercise are in Table 7.3. Note that we processed these data in UTM coordinates. So in order to report along track position errors, we calculated ΔY based on the azimuth angle 32.4° that we calculated as the azimuth between north and the straight line extending from target T-001 to target T-010 of the test strip. The results are similar to those shown in Table 7.2. The MetalMapper meets the performance goal for repeatability of the anomaly position. However, as in the previous results, the repeatability of the peak anomaly amplitudes is more like 25% (relative to the associated mean value) as opposed to the performance goal of 15%.

Discussion

We were concerned that the results from our (dynamic) repeatability tests may indicate instability that we do not observe when we compile statistics from repeated static measurements wherein the platform is positioned much more precisely over the target. We make the following observations:

1. When viewed in a local coordinate system in which the line $x = 0$ represents a line connecting target T-001 to target T-010, the only targets having the local coordinate $x=0$ are the aforementioned targets. The other 8 targets have x-coordinates with non-zero x-offsets as large as 0.28m (see Table 7.4).
2. The test strip survey was conducted as a single-profile survey in which the vehicle operator navigated along a pre-planned straight-line profile extending from T-001 to T-010. So even when the navigation was perfect and the antenna platform followed the line $x = 0$, there would be cross-track offsets exceeding 10cm between the antenna reference point and the target for targets T-002, T-003, T-005, and T-008. Figure 7.2 is a base map showing the line and target locations. The target symbols are approximately 0.8m in diameter. The figure shows that the survey lines were slightly bowed toward the grid east (local x). This could be because our navigation software does not account for the GPS antenna height and platform attitude in real time. In any case, the figure shows the profiles to be biased toward grid east in the center.

Table 7.4: Local coordinates for target locations in the test strip at SLO.

Tgt	X (m)	Y (m)
T-001	0.	0.
T-002	0.2845	6.854
T-003	0.1112	13.05
T-004	0.003835	19.61
T-005	-0.1802	26.08
T-006	0.06596	32.57
T-007	-0.02991	39.14
T-008	0.1058	45.39
T-009	0.04832	52.08
T-010	0.	58.67

3. Analysis shows that the ensemble of 59 repeat profiles can be contained within the limits $-0.4 \leq x \leq 0.4$ m. Thus, the variation in cross-track distance from the target may be 40cm or more.

In view of the range in the cross-track distance from a target, we decided to look at the attenuation of the peak amplitude of a target as a function of profile offset from the target center. We varied the offset in 5cm increments out to 30cm. We analyzed target peaks for both split-cube anomalies and for the EM61-like average of the inner 5 Z-components from the MetalMapper cube array (“Avg5IZ”).

In Figure 7.3 we show stacked profiles for the for the 7 MetalMapper cubes as they move across the target.²³ Regrettably, the MetalMapper cubes are ordered according to their cart y-offset value (along track). For viewing this figure it would be more convenient if they were ordered according to increasing x-coordinate. The reader can refer to Figure 2.6 to find the location of the receivers. Cube 4 is the center cube. Cube 1 has the largest cross-track coordinate ($x=39$ cm) while cube 7 has the smallest cross-track coordinate ($x = -39$ cm). The other 4 cubes have cross-track coordinates that alternate in sign.

At YPG and APG, we used a detection parameter that is easier to compute, the Avg5IZ parameter.²⁴ To complete this analysis, we also computed the Avg5IZ profiles as a function of antenna array offset. Those profiles are shown in Figure 7.5. Note that the profiles with non-zero offset do not exhibit perfect symmetry as one might expect from a real single loop receiver. That is because of the lack of bilateral symmetry in the MetalMapper receiver array.

Both Figure 7.3 and Figure 7.5 show that the attenuation in the peak anomaly signal is significantly affected by offset with gradients increasing at the larger offsets.

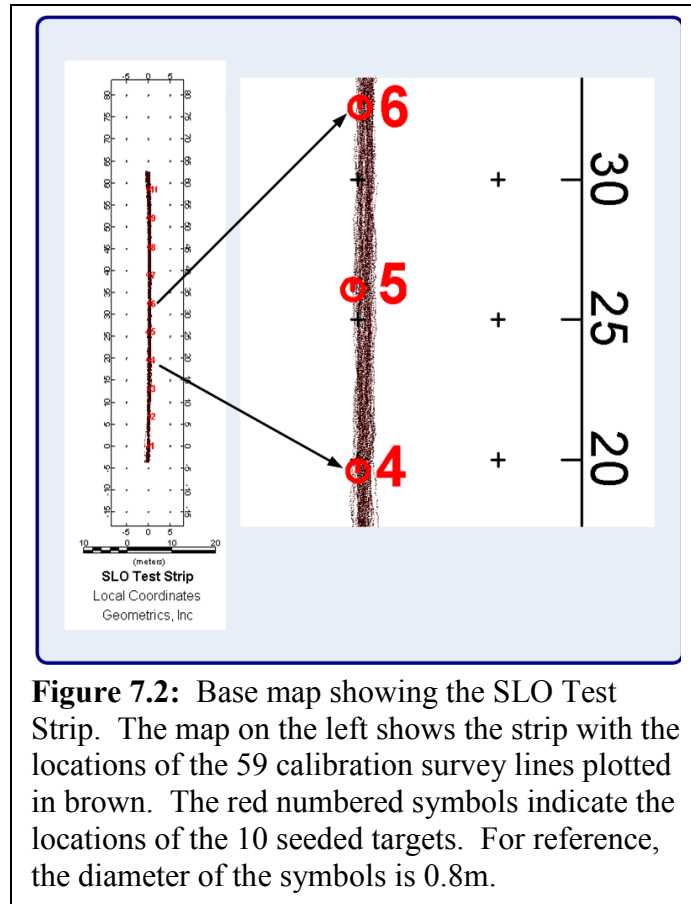
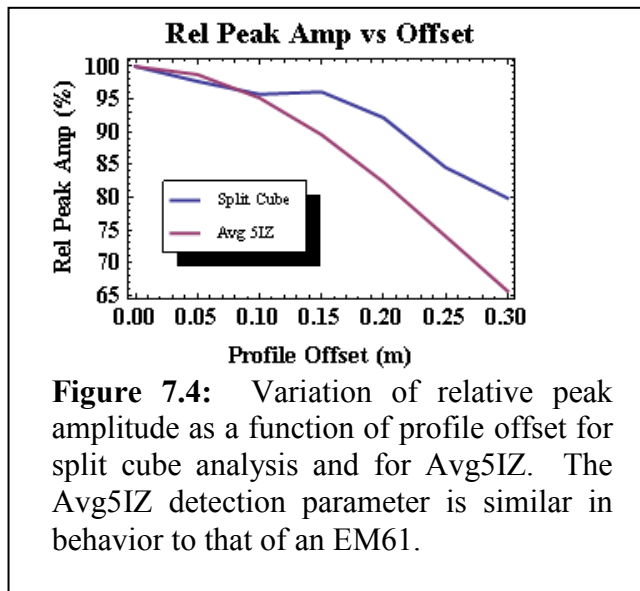
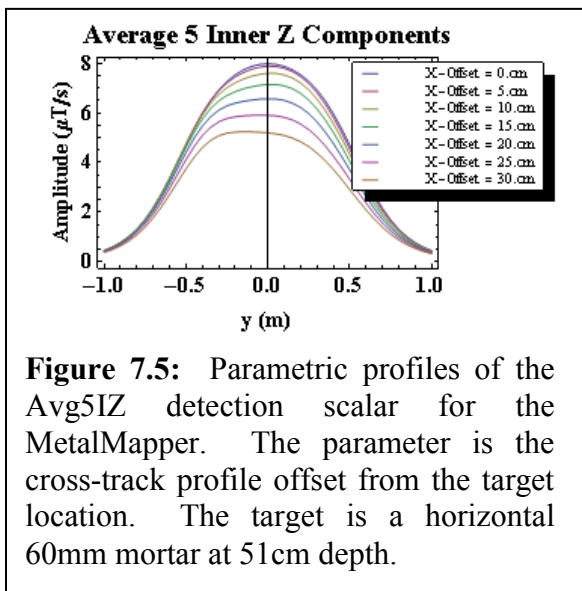
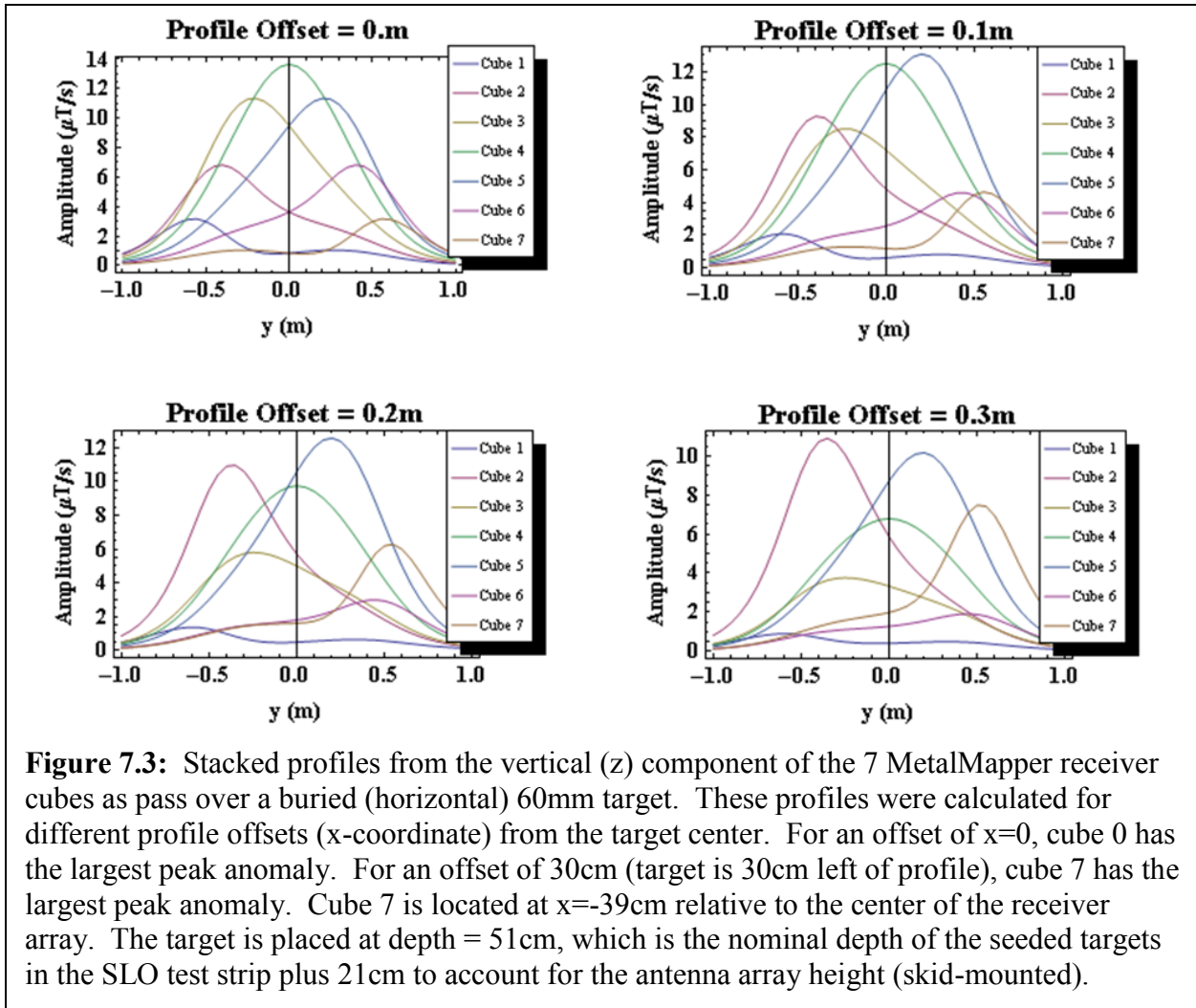


Figure 7.2: Base map showing the SLO Test Strip. The map on the left shows the strip with the locations of the 59 calibration survey lines plotted in brown. The red numbered symbols indicate the locations of the 10 seeded targets. For reference, the diameter of the symbols is 0.8m.

²³ The reader must imagine that these 7 profiles have been spread out laterally on 13cm centers and shifted along the y-axis so that the peaks line up.

²⁴ The Avg5IZ parameter is simply the average z-component from cubes 2 through 6. This parameter behaves much like a large single-loop receiver like those on an EM-61.



In Figure 7.4 we summarize the attenuation of target amplitude as a function of offset for the two detection types (split-cube, and Avg5IZ). Note that the attenuation for both cases is about the same for offsets out to about 15cm. Then, the signal strength for the Avg5IZ detector falls at a significantly faster rate. What is most significant, however, is the relative peak signal strength can vary by as much as 20% for split cube analysis and by 35% for Avg5IZ. This study shows that great care must be taken when attempting to demonstrate repeatability in dynamic surveys. For relatively shallow targets such as those in the SLO test strip, the survey profile must be repeated with maximum cross-track errors on the order of $\pm 0.10\text{-}0.15\text{m}$. We simply did not take sufficient care that the survey followed the same track.

Because we processed our calibration data into split-cube lines, we were able to make rough estimates of both the along-track and cross-track target positions. This provides us with data that can verify whether our failure to achieve the $\pm 15\%$ amplitude repeatability goal is at least in part due to large variations in offsets. In Figure 7.6, we show scatter plots of the (relative) peak anomaly value as a function of the estimated offset distance to the target. These data still exhibit more scatter than we would like. Nonetheless, they suggest a relationship between offset and the peak value. In particular, in Figure 7.6B the quadratic trend line peaks at an offset of approximately 0.25m. This is the correct offset for target T-002 (see Table 7.4).

As a final check on repeatability, we went back to our APG dynamic calibration data. At APG, we laid out a line approximately 20m long in an area of low background. At the center of the line, we buried a 12-lb shot put at a depth of approximately 20cm. We ran a dynamic survey consisting of 2 reciprocal lines over this target a minimum of twice each day during those days that we were surveying in dynamic mode. Figure 7.7 is a base map showing the calibration lines at APG. We have plotted the location of 25 lines in brown. The red circle represents the mean location for the anomaly peak from the calibration sphere (shot put). The inset drawing is an expanded view of a 1.5-m section of the line that includes the target. For reference, the outside diameter of the red circle is 0.75m. The cross-track envelope of the 25 lines that have been plotted is less 10cm. The statistics for the peak amplitude of our calibration sphere at APG was 37.90 ± 3.83 (1σ) for a repeatability of $\pm 10\%$.

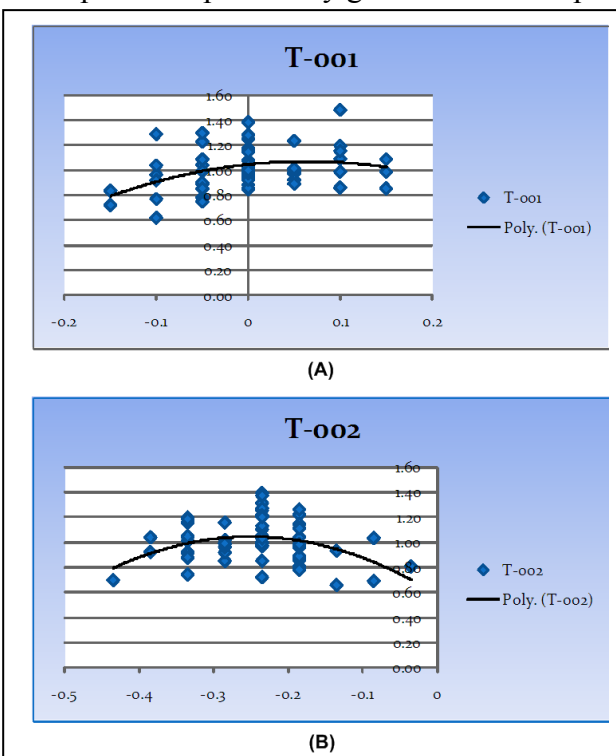


Figure 7.6: Scatter plots suggesting that part of the problem with poor anomaly amplitude repeatability is due to offset. In these scatter plots, the horizontal axis is the cross-axis error between the anomaly peak and the target position. The vertical axis is the observed anomaly relative to its mean.

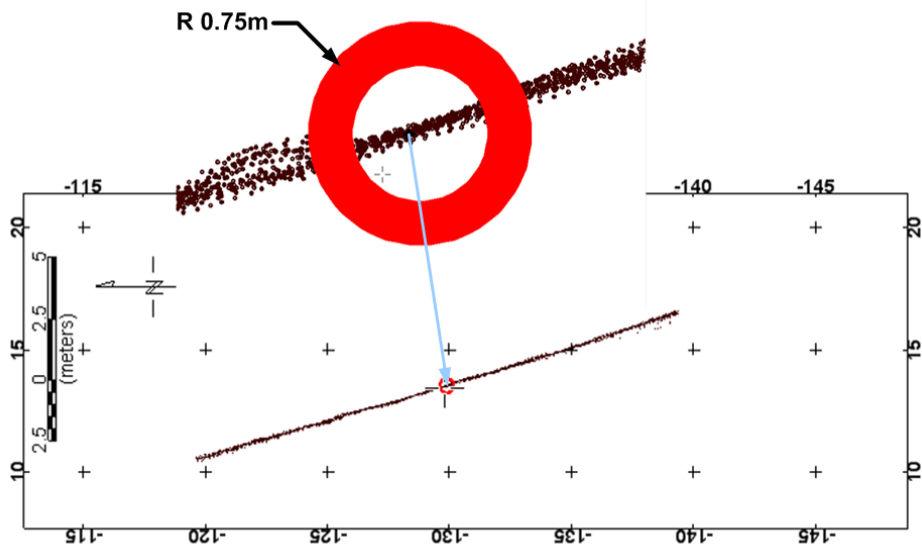


Figure 7.7: Base map upon which has been plotted the location of 25 dynamic calibration lines at APG. The red circle marks the target (shotput) and the inset shows that the envelop of the line tranverse to the direction of motion is less than 10cm.

7.3. Target Detection

At SLO, there were 187 seeded targets.²⁵ The MetalMapper failed to detect four (4) of those seed targets. The four targets we missed were all 60mm mortars. Therefore, we achieved the

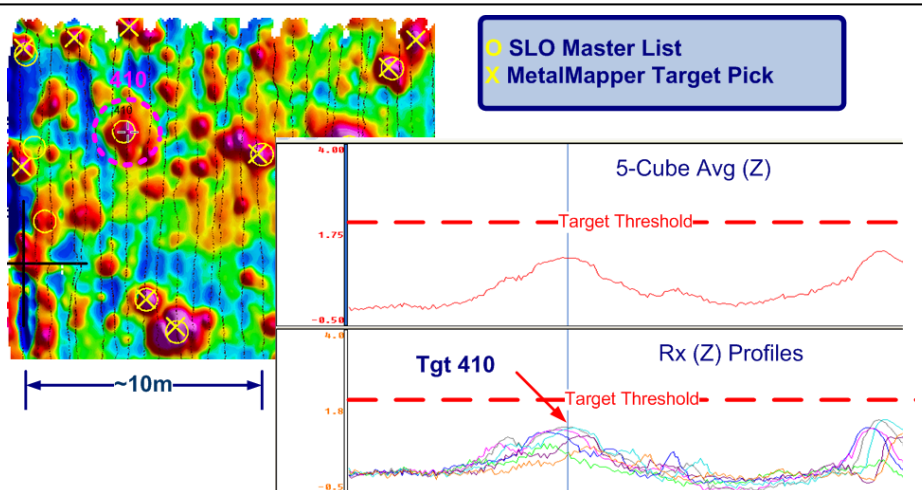


Figure 7.8: Figure showing one target that went undetected in the MetalMapper dynamic survey. Target 410 is readily discernible on both map and on the profiles. Although it has a broad areal extent indicating a deep target, its amplitude fails to rise above the detection threshold.

²⁵ We obtained an unofficial list of the seeded targets from Dean Keiswetter (SAIC).

stated performance goal of $P_d \geq 98\%$.

It is instructive to look at the reasons we failed to detect these 4 targets (SLO targets 59, 478 410, and 16. All 4 of the targets that we failed to detect were 60mm mortar bodies. Target 410 is typical of the other 3. The issue is summarized graphically in Figure 7.8. The anomaly is obvious in both the map and the profiles. But it fails to rise above the experimentally verified detection threshold. The “expert” interpreter would have recognized this anomaly as likely arising from a deep target because of its broad extent and coherence notwithstanding its low amplitude. A look at the recovered target object (Figure 7.9) explains why this target had a lower detection signal amplitude than we expected for a 60mm object. The seeded target was a 60mm mortar (body only) target. We defined the detection threshold based on the signal amplitudes for a 60mm M49A4 (see Figure 7.22), the type of 60mm mortar seeded at APG and YPG, buried in the test lanes at SLO, and provided at SLO for free-air tests. The mortar body target has an electromagnetic size that is approximately half the size of the complete mortar including fins and a fuse. Obviously, the detection threshold was set too high. However, had we set the threshold to 1 uV/Am^2 we would have easily doubled or perhaps tripled the number of targets detected. This example of a “**false negative**” in detection identifies two important weaknesses in basing detection on the criterion that the peak anomaly must exceed a threshold:

1. The threshold value, even when chosen in a “principled” manner as we have done, does not always account for variations in the configuration of the “smallest” target of interest. Nor can a threshold value account for the presence of a target of interest that has not been identified as being present in the survey area and therefore was not considered when establishing setting the detection threshold. One such target, a 37mm projectile, was found during the target recovery at SLO.
2. By simply lowering the threshold, we can easily double or triple the number of targets, a very high percentage of which are bound to be near-surface clutter. Most low-amplitude anomalies arise from small bits of near-surface clutter having very different anomaly characteristics from those shown in Figure 7.8. We believe that by using the fact that each sample of MetalMapper dynamic data actually includes vector measurements at 7 different spatial data points relative to the platform position can be used to recognize the difference between anomalies having roughly the same peak amplitude arising from small objects at shallow depths and large objects at deeper depths. Such a capability can provide the basis for a better “physics-based” method of target detection or anomaly screening.

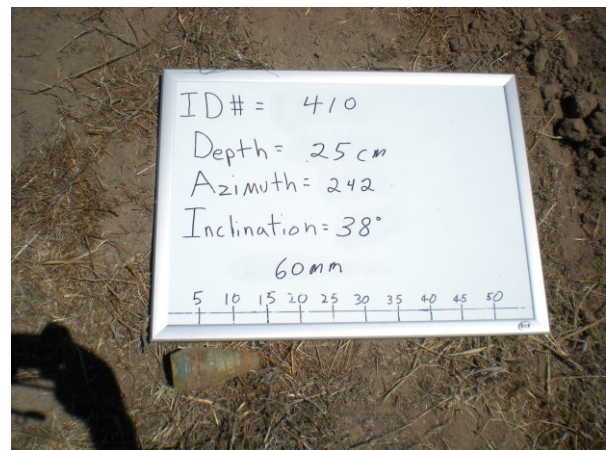


Figure 7.9: Photograph of the recovered 60mm “body” associated with SLO target number 410.

7.4. Analysis and Classification Performance

In section 6 we tried to show how our capabilities for making “principled” decisions have developed throughout the course of this project. The SLO project served as a catalyst that permitted us to develop a methodology that, in most respects, achieves the performance objectives set out in the ESTCP demonstration plan. The bases for discussion in this section are the scoring results that we received from IDA in early November 2009. In Figure 7.10 below, we have reproduced and annotated the IDA ROC curves. These ROC curves summarize the scoring results representing a partial dig (1064 items²⁶ from a list of 1408) of the MetalMapper target list.

7.4.1. Maximize Correct Classifications - Munitions (see Section 3.4)

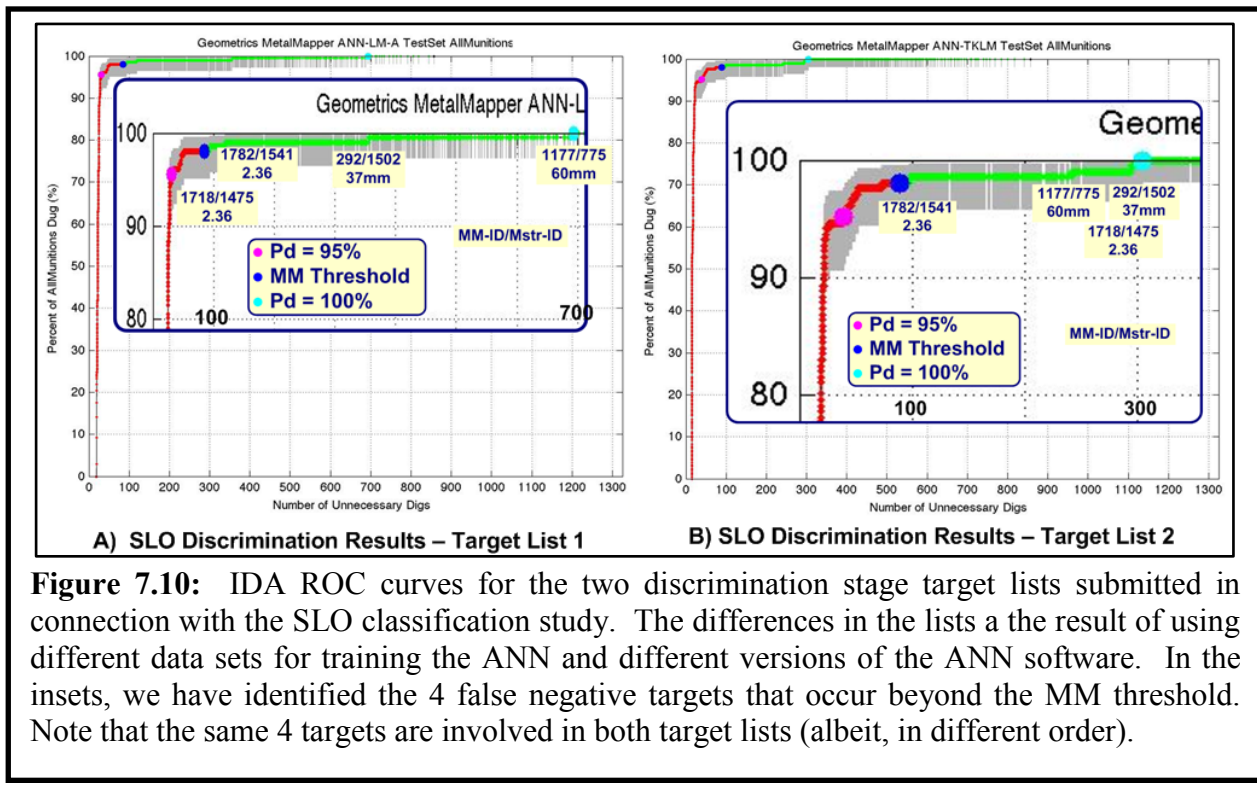


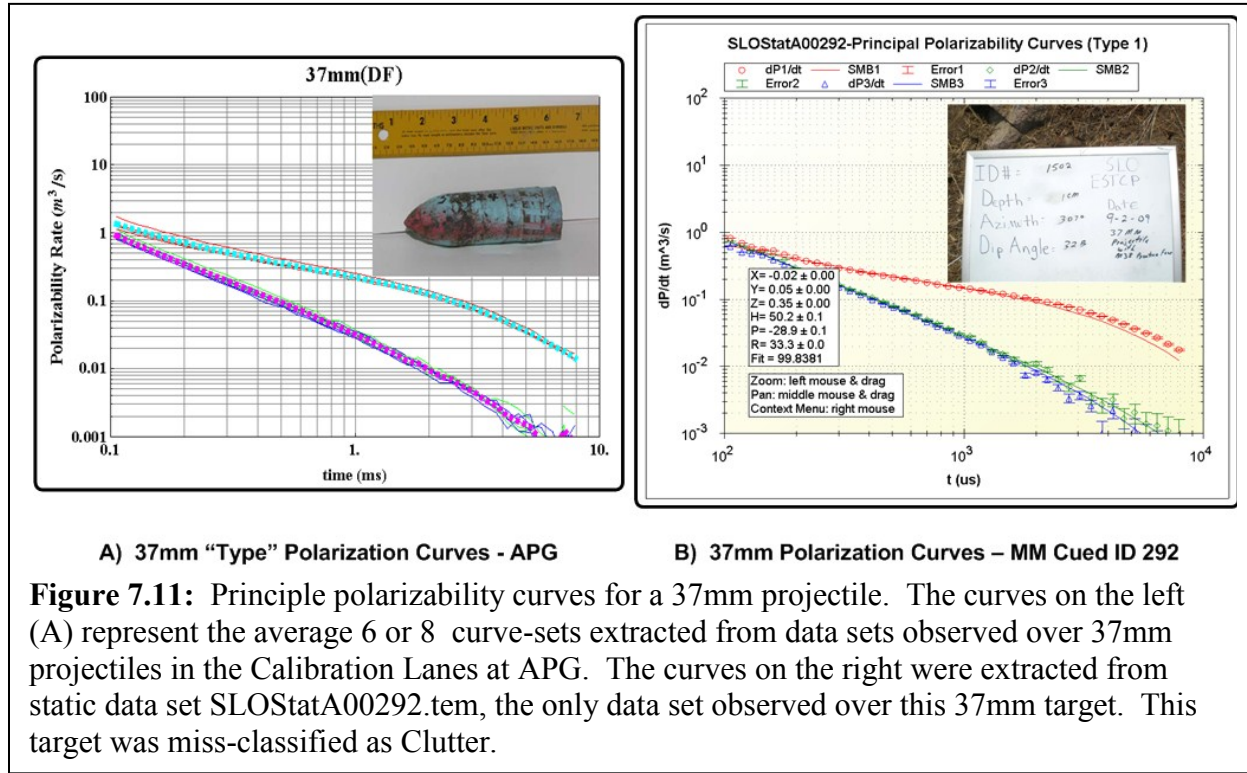
Figure 7.10: IDA ROC curves for the two discrimination stage target lists submitted in connection with the SLO classification study. The differences in the lists are the result of using different data sets for training the ANN and different versions of the ANN software. In the insets, we have identified the 4 false negative targets that occur beyond the MM threshold. Note that the same 4 targets are involved in both target lists (albeit, in different order).

The ROC curves (Figure 7.10) speak directly to the objectives for maximizing the correct classification for both TOI and clutter. With regard to TOI, the results show that at our operating threshold, in both cases we had 4 false negatives, two of which were very “hard” in the sense that our classifier indicated that it was highly probable that these objects were clutter. However, target list 2 (Figure 7.10B) distinguishes itself from its companion in that significantly fewer unnecessary digs are required before the last TOI is eventually found.

We have examined the dig results from the four targets associated with the hard negatives. In the expanded ROC curves (inset Figure 7.10 A & B) the 4 targets are identified according to their MetalMapper ID and Master List IDs, respectively, with the “/” character as a separator. The

²⁶ The test data used by IDA consists of 1064 targets of which 206 were designated TOI and the balance (858) as clutter or non-ordnance items.

37mm target is the only target that is an obvious “miss” that could have (should have) been avoided by a comprehensive visual examination of the polarizability curves. After assembled our prioritized dig list, we did in fact perform a partial visual QC involving perhaps 100 targets on either side of our operating threshold. We did this in order to identify a set of targets bounded on one side by the operating threshold (i.e., the boundary between “High Confidence Not Munitions” in Figure 6.21) and on the other side by targets designated as “High-Confidence-Munitions” targets. These “Ambiguous” targets are those that we believe are associated with analyzable data for which we get ambiguous classifications. However, in both target lists the 37mm target (the only one in the test data set) was very strongly identified as clutter (non-munition). The problem here is that our classifier was not trained to identify a target of the size and shape of the 37mm. In our retrospective study, we added the polarizability curves for a 37mm from our library of munitions types for APG (see Figure 7.11). Our library matching algorithm identified the 37mm with very high probability. Therefore, we conclude that we will be able to detect and classify 37mm using library matching provided we add a 37mm type to our matching library (a 6th type) and that we include specimens of the 9-component feature vector extracted from static measurements of 37mm projectiles.



The second hard false negative that we wanted to examine is the 60mm mortar found in association with MM-ID 1177 (Master List ID 775). The polarizability curves together with the dig photo are in Figure 7.13. A segment of the detection map together with the associated data profile is shown in Figure 7.12. For reference on the map, the target symbols have a diameter of 1m. The profiles show the average 5IZ detector (top – red) and the 7 vertical components plotted

together in the bottom panel as color-coded profiles. The horizontal coordinate is the easting value. But the profile is generally in the NW-SE direction so the horizontal scale as indicated by the axis grid is misleading. The peak 1176 adjacent to and SE of 1177 is on the MetalMapper target list but had not been excavated at the time that IDA released the scoring to SLO demonstrators. In any case, the polarizability curves suggest a shallow equi-dimensional object which is consistent with the 60mm tail boom segments sitting on the board. The anomaly amplitude is less $10 \mu\text{T/s}$ which means it is only slightly above the detection threshold for a deep mortar. Yet the solution for the target position indicates a target at a depth of 13cm.²⁷ It appears therefore that the anomaly produced by the tail boom(s), which no

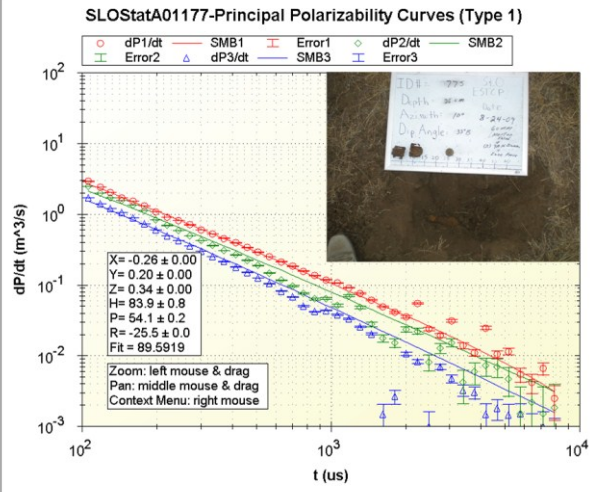


Figure 7.13: MM Cued ID No. 1177 and the corresponding dig photo. The target in the hole is a 60mm mortar. The polarizability curves appear to represent the associated tail booms and/or fuse.

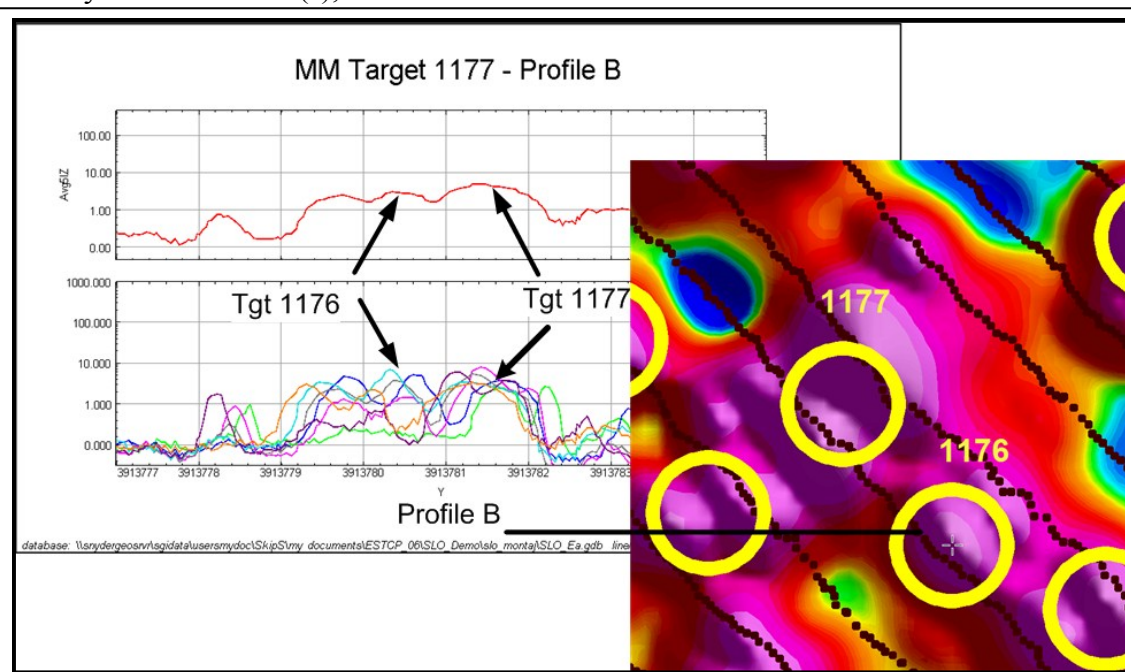


Figure 7.12: Detection profiles and a segment of the associated split cube detection map for MetalMapper Cued ID target number 1177. The anomalies seem to reflect a shallow target such as the tail booms found (presumably) above the deeper 60mm mortar.

²⁷ The z values given in the polarizability plot is with respect to the platform reference point. That point is 21cm above the ground surface.

doubt were found above the deep mortar shown in the photo, totally overpowers the low-signal level from the mortar. This is a case where the interference from several shallow sources obscures the deeper TOI. The best and only chance we have of mitigating this type of anomaly is to recognize that it is a complex response that cannot be analyzed and therefore must be dug.

The remaining two false negative targets have MM-ID's 1718 and 1782. These targets correspond to 2.36-in rocket parts. The dig photos and the associated polarizability plots are shown in Figure 7.14. On target List 1 (Figure 7.10A), neither of these targets is very "hard" false negative and require only a few extra 10's of digs before they are found. However, on List 2, 1718 (at about 300 extra digs, Figure 7.10B) is very close to the 37mm target (292). Therefore, the fact that we can, in a "principled" way reorganize our dig list to

remove the 37mm doesn't help us much because we have target 1718 with about the same dig priority. In both cases, the polarizability curves are in no way suggestive that the target is a TOI.

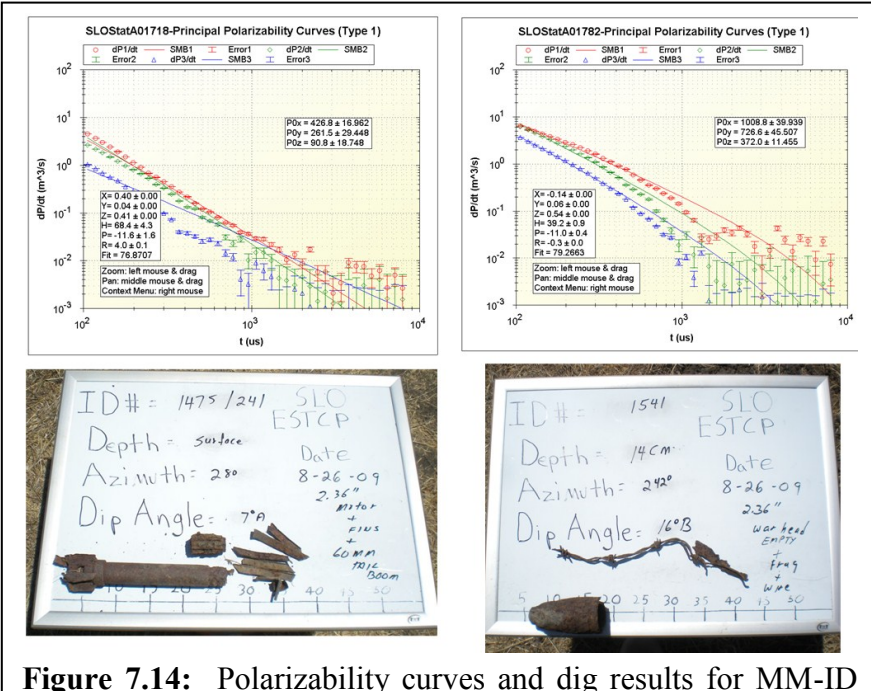


Figure 7.14: Polarizability curves and dig results for MM-ID Numbers 1718 and 1782, two of 4 false negatives in both target lists submitted to IDA.

MM-ID 1718: The profiles for the dynamic survey line crossing directly over this target together with a segment of the split cube detection map that includes the target are shown in Figure 7.15. Although there is some noise in the individual cube profiles, both the map and the profiles suggest a single target. Target 1717 is located less than 1m to the SE of 1718 and looks to be the 2nd peak of the anomaly. Our inversion software predicts that the source point for the target lies 0.4m east of the target pick (center of target circle). The polarizability curves for MetalMapper targets 1717 and 1718 and the size estimates ($P0x=428$ in Figure 7.18 right) indicate that the parameters most likely belong to the 60mm tail boom shown in the dig photo rather than the rocket motor. The polarizability response of an isolated rocket motor is significantly larger and shows good symmetry and large aspect. This target intrigued us partly because it is a hard false negative, but also because the dig reports that the target was found laying on the surface. How then could we have missed a target like that? In looking through our field notes, we came across a note for file SLOStatA01715, a static data point acquired in the immediate vicinity of 1718. The note (see Figure 7.16A) indicates that a measurement on an unpicked point was acquired near or over a "rocket shaft" that had obviously been moved recently because it was laying on top of the grass. It is likely that the rocket motor shown in

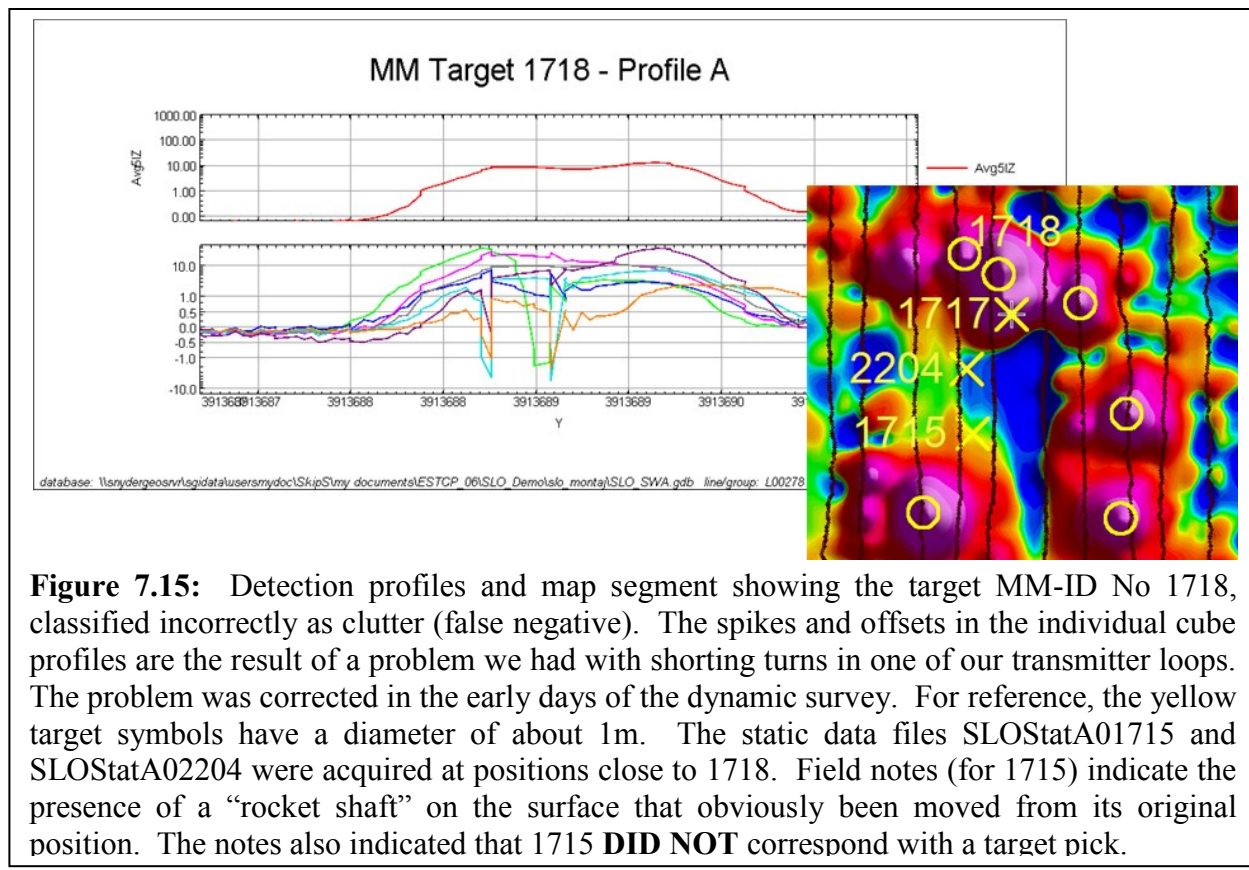


Figure 7.18 was found in the immediate vicinity (i.e., within a radius of 1m or so) and lumped in with the 60mm tail boom. The ground-truth indicates the target was found within a distance of 0.3m of the location of MM 1718.

1715 Rocket shaft surfaces not picked. Griss under north so has been moved since spray. Marked with flag.

A) Excerpt: Field notes (p. SLO61 6/13/09)

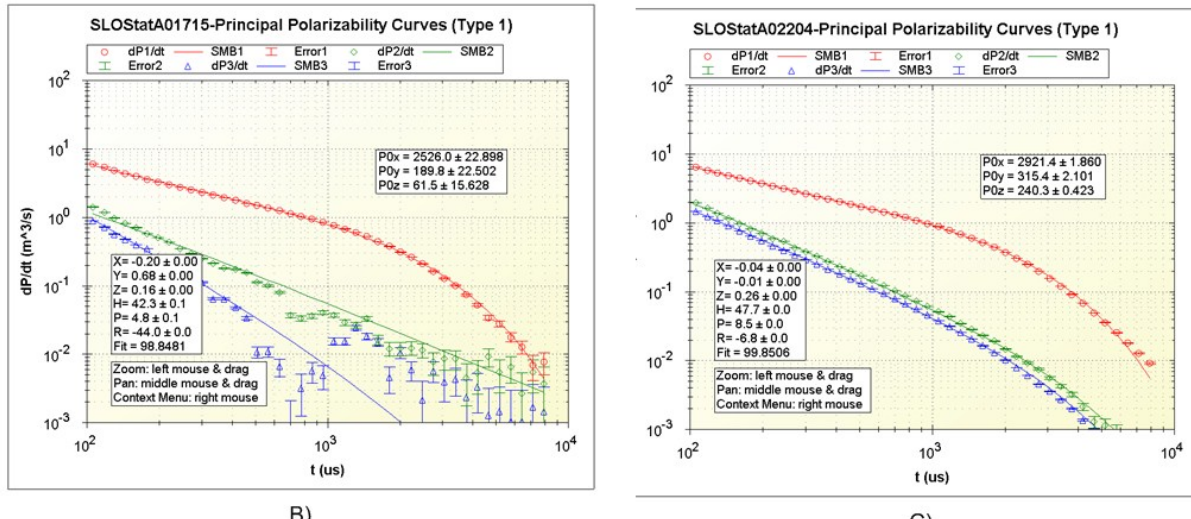
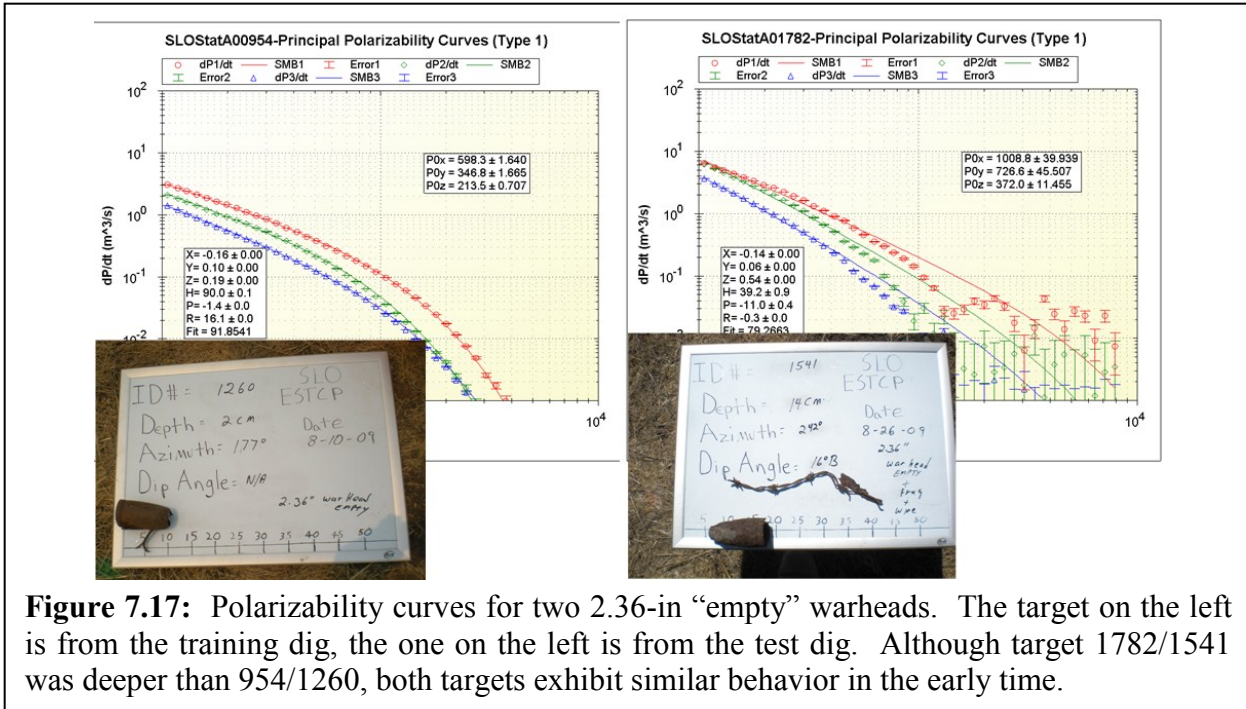
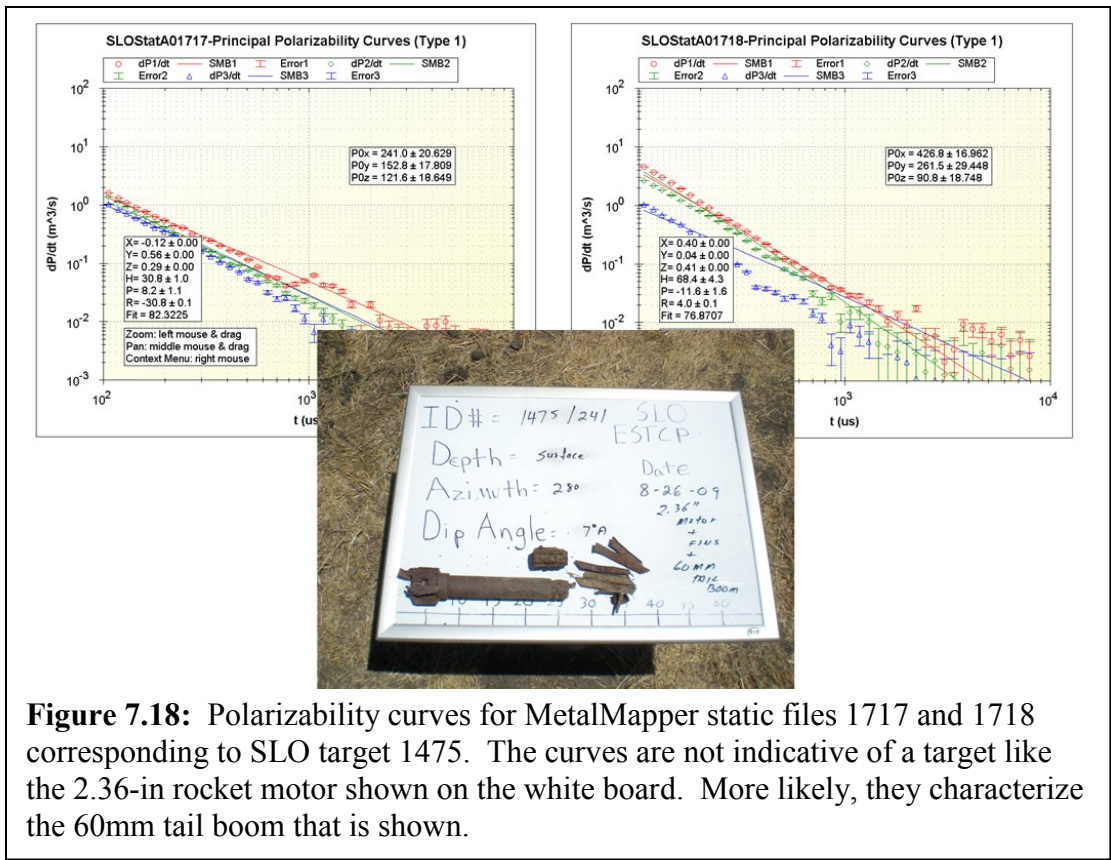


Figure 7.16: Field note describing target near 1715 as a “rocket shaft” (A) together with the polarizability curves for 1715 and a repeat (2204). The polarizability curves both look like rocket parts. These two data sets are within a meter or two of MM-ID 1718.



MM-ID 1782: Relatively speaking, target number MM-ID 1782 (Master ID 1541) is the least important of the 4 false negative targets that are labeled on both panels of Figure 7.10. The position of this target is roughly the same on both ROC curves (Figure 7.10 A & B) and requires only a few unnecessary digs past the operating point (dark blue dot) to get to the target. We mention it here only for completeness. We would like to note however, that the target (Master ID 1541) is similar in both appearance and in the behavior of its principal polarizability curves to target SLO Master ID 1322 that was belatedly labeled “MD” after a more careful examination. The polarizability curves and photos of MetalMapper targets 954 and 1782 provide a comparison between the two targets, one labeled “MD” and the other labeled “TOI”. The similar behavior of the polarizability curves suggests that target 1782 is cracked or otherwise physically damaged in a way similar to that of 954.

Remarks: The forgoing discussion contains reasonable explanations 3 of the 4 false negative targets appearing in both target lists. After considerable analysis, we can find no explanation for why our polarizability parameters do not indicate a 60mm mortar other than the mortar was reasonably deep (26cm) and were two 60mm tail booms found above the mortar. The polarizability curves seem consistent in shape and size with the tail booms and therefore it is most likely that the low-level signal from the mortar was overwhelmed by much larger signals arising from shallow tail boom targets.

7.5. Maximize Correct Classification of Clutter

In the test data set, there were a total of 857 clutter objects. The results from List 2 (Figure 6.28B), shows that after \sim 300 unnecessary digs, we have excavated all the TOI ($P_d = 100\%$). Therefore we found all the TOI after a total of 506 digs and would be able to safely leave the remaining 557 clutter targets in the ground. This represents a reduction of 65% in false alarms and thus we exceed the performance goal of a 30% reduction. We note, however, that if we use our List 1, it would take approximately 906 digs before we had excavated the last TOI. This represents a reduction of only 18%.

Discussion: Prior to submitting our second target list (List 2), we made what appeared to be a minor correction in the rules algorithm that we apply to the stream of the ANN decision scores and the target matching scores. These changes did not appear to affect our training ROC. However, we applied the same (revised) decision rules to both Lists 1 and 2 and plotted new ROC curves. These curves are shown in Figure 7.19. In making these ROC curves, we used all

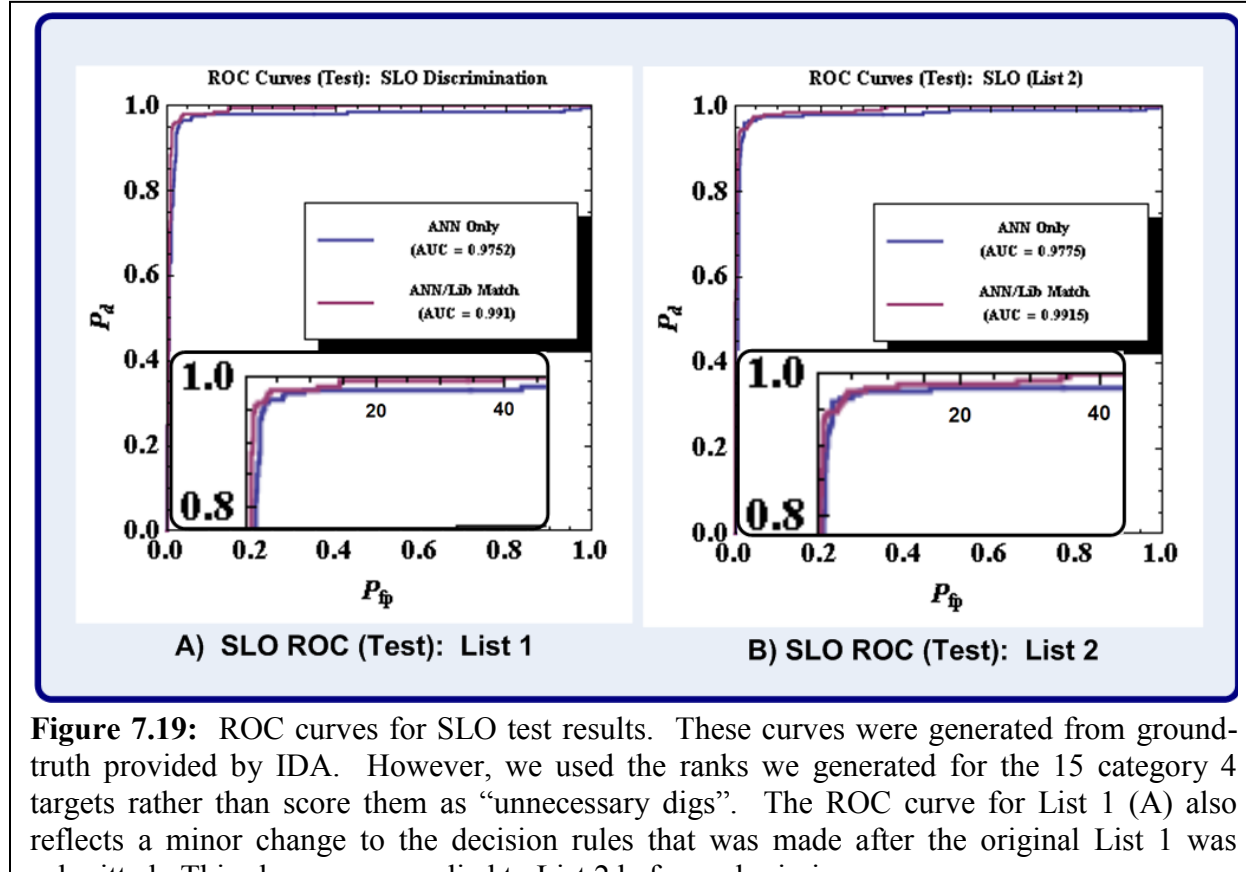


Figure 7.19: ROC curves for SLO test results. These curves were generated from ground-truth provided by IDA. However, we used the ranks we generated for the 15 category 4 targets rather than score them as “unnecessary digs”. The ROC curve for List 1 (A) also reflects a minor change to the decision rules that was made after the original List 1 was submitted. This change was applied to List 2 before submission.

category 4 targets since the ground-truth provided by IDA showed that our decisions on those (15) targets were all correct. Moreover, the List 1 ROC reflects a minor change to the rule-based decision algorithm that we made after we submitted List 1 and before we submitted List 2. These curves reflect exactly the same rules. Note that the rule change moved the very hard false negative in Figure 7.19A down to about $P_{fp}=40\%$. This means that now, only 342 unnecessary targets are dug before we get to $P_d=100\%$. With this minor change to our rules, List 1 also achieves the performance goal of a 30% reduction in unnecessary digs. There is no change to the performance of List 2 (about 300 unnecessary digs at $P_d=100\%$).

7.6. Operating Point Specification (No-Dig Threshold)

The operating points for Lists 1 and 2 are indicated as dark blue points in Figure 7.10. In both cases, this operating point is at $P_d=98\%$ (202/206). At that point, there have been approximately 90 unnecessary digs. This leaves a total of 767 clutter objects (85%) correctly classified and thus exceeds the performance goal of >30% of the clutter objects correctly classified at the demonstrator-specified operation point.

7.7. Minimization of Cannot Analyze Points

Of the 1063 targets that were scored, there were 15 category 4 points (“Cannot Analyze”). Those points were points for which the fit statistic was less than 75. The points represent 1.4% of all the targets analyzed. Using the ground-truth from the test dig, we determined that the discrimination results for all 15 category data points were correct. Although we do not feel comfortable with completely eliminating a screening rule that relegates data points with poor fit to category 4, in retrospect we think that we were too conservative in assigning the Fit<75% threshold. By assigning a slightly lower threshold (e.g., Fit < 70%) we can eliminate half of the category 4 points with little or no danger of introducing a false negative. In any case, MetalMapper has clearly met the performance goal of >90% of all targets being analyzable.

7.8. Correct Estimation of Parameters

In the MetalMapper data set, there were a total of 187 data files whose positions correlated with the known position of a seeded target.²⁸ We used the inversion results from these data files as the basis for judging how well we did on our parameter estimates. To attain the performance goals, it is first necessary to correctly estimate the 3-dimensional position of the target. Provided we have a good estimate of position, estimates of the principal polarizability curves are straight forward. Errors in the magnitude of the principal polarizability curves are proportional to the position error according to a power-law [25] and, hence, a bad estimate of the former guarantees a worse estimate of the latter.

7.8.1. Position Estimates

We computed the 3-D position errors between the position of the seeded target (as measured after the dig) and the position estimated from the associated MetalMapper static data point. We analyzed the horizontal positions and the depths separately.

Depth Errors: The distribution of depth errors for the 187 seed targets analyzed is shown in the histogram (Figure 7.20). The mean and the standard deviation (4.9cm and 6.5cm, respectively) are also noted on the diagram. The solid red curve is a Gaussian curve with the indicated mean and standard deviation that has been normalized to the number scale of the histogram. These data show that depth errors are reasonably approximated by a normally distributed random process. The mean value of 4.9cm shows that the MetalMapper depth estimates are biased too deep. We have not been able to explain this bias in the depth estimate, thought the bias was not seen in other surveys at APG and Camp Butner. In any case, the figure shows that the MetalMapper depth estimates easily meet the

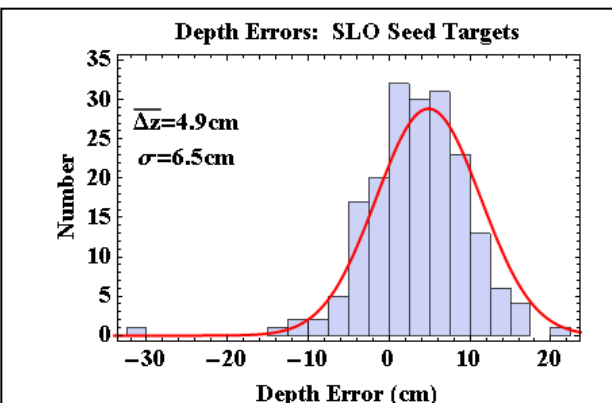


Figure 7.20: Depth error histogram for 187 seed targets at SLO.

²⁸ There were an additional 34 MetalMapper data files that were associated with seeded targets but were not as close to the target as the primary target file.

performance goal of ± 10 cm (1σ). The systematic error is attributable to how the depths were measured.

Horizontal Position Estimates: In Figure 7.21 we have plotted the horizontal error as a polar plot. The plot has been annotated with the mean and standard deviation for both the error radius (Δr) and the error azimuth (ϕ). The plot shows that the errors are biased by 4.5cm. It is possible that this bias reflects a misalignment between the GPS antenna (elevated 1.48m above the platform reference point) and the normal to the Z transmitter coil that passes through the center cube. It is also possible (and perhaps more likely) that the bias reflects an output bias in the X-Y accelerometers on the attitude sensor. With the GPS antenna waving around at a height of 1.48m above the platform, an error of only 1.8° would introduce a bias of 4.5cm. However, even with the bias included in the error, the horizontal position estimates are well within the performance goal of 15cm (1σ).

7.8.2. “Beta” Estimates

The term “Beta” as used in Table 3.1 refers to the principal polarizability transients and/or composite values derived there from by numerically integrating the principal polarizability transients over a specific time gate. As we have stated previously, these principal polarizability transients are the source of all the intrinsic information about the target. In the October, NRL/SAIC undertook to make static free-air measurements of each of the seeded target items that were used during the SLO field demonstration using the TEMTADs system. Typically, each target was measured in three attitudes (flat, nose up, and nose down) at a single depth. These data were reduced using the SAIC dipole-based inversion program to yield a set of 3 principal polarizability curves for each target and each attitude. Unfortunately, the ground-truth that was recorded failed to identify a specific seed item with a specific target site or SLO Master List target number. However, from the ground-truth information provided, we were able to identify 186 MetalMapper targets as “Seed” targets. Moreover, the ground-truth that we were provided allowed us to associate each of those targets with 6 different UXO types.²⁹ Therefore, statistically at least, we have a basis for measuring how well we were able to estimate the target “Betas” by comparing “Beta” values extracted from the free-air measurements that SAIC conducted on SLO seed items, and similar “Beta” values extracted from MM data sets corresponding to the same type of seeded target.

SAIC was kind enough to supply us with a well documented set of principal transient curves resulting from the inversion of TEMTADs data sets acquired over the seeded items. As we

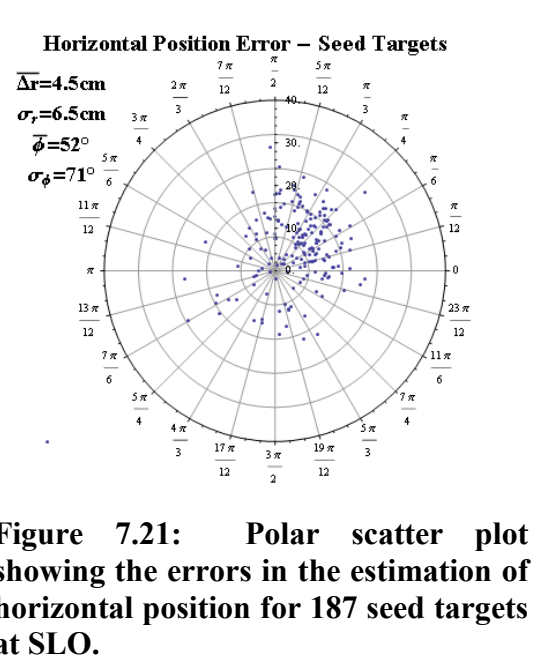


Figure 7.21: Polar scatter plot showing the errors in the estimation of horizontal position for 187 seed targets at SLO.

²⁹ Although there were only 4 targets of primary interest (60mm/81mm/4.2-in mortars plus 2.36-in rockets), we learned 60mm and 81mm mortar seed items consisted of “mortar bodies” and “complete mortars” (i.e., with fuse and fins).

indicated above, this documentation identifies the specific target type (e.g., “60mm mortar”, “60mm mortar body”, “4.2-in mortar”, etc) but was not able to identify a particular target specimen with a particular SLO Master List target number. All TEMTADs data were acquired using a base acquisition frequency of 10 Hz that resulted in principal polarizability curves with a time bandwidth of 25ms. Moreover, SAIC reduction procedures apply a delay time correction of -28 μ s and an amplitude correction of 0.175 to their data before inversion. The delay correction accounts for analog delay in the acquisition system and was empirically determined by SAIC so that test data acquired with the TEMTADs system better matches the theoretical curves for a sphere. Likewise, the amplitude factor was established for similar reasons before SAIC was provided with information about the gain settings in the TEMTADs data acquisition system. In its reduction, MetalMapper does not apply these correction factors³⁰ and so we have “backed out” the SAIC corrections from their data in order that we can fairly compare “Betas” extracted from either system.

³⁰ There is validity in the time delay correction. However, we have not attempted to experimentally establish its value. We are confident that the voltage amplitudes that we measure are correct with a precision of approximately 1%.

Comparison of “Beta” Curves – For each target class (e.g., 60mmM49A4) we have a number of free-air measurements acquired with the MTADs system and, likewise, a number of measurements made over *in situ* targets with the MetalMapper. In Figure 7.22, we have plotted the principal polarizability transients of all the measurements for both 60mmM49A4 and 81mm targets. Although there is some scatter in the individual curves due to different target attitude and perhaps minor differences between various instances of the target types, the resulting geometric mean principal curves (heavy red/green/blue curves) are virtually identical. Similar results were obtained for 4 other target types: a) 60mm M49A4 Body; b) 81mm Body; c) 2.36-in rocket; d) 4.2 in mortars. It is difficult to compare the geometric mean curves since they are based on different time gates and time bandwidths.³¹ In principle, it would be possible to quantitatively compare the resulting geometric mean transient curves using the same curve matching procedure that we applied for discrimination. However, because of the different time

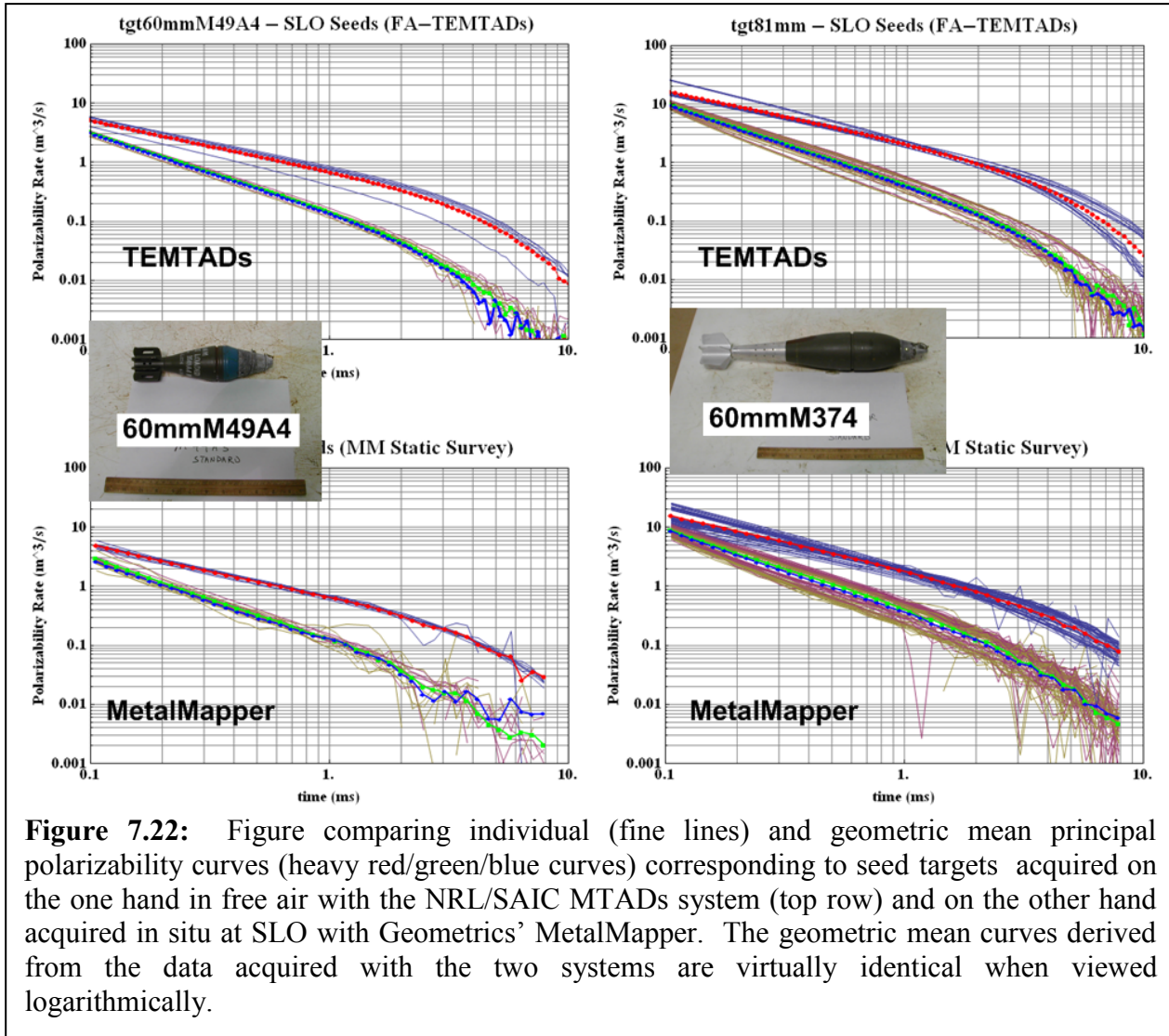


Figure 7.22: Figure comparing individual (fine lines) and geometric mean principal polarizability curves (heavy red/green/blue curves) corresponding to seed targets acquired on the one hand in free air with the NRL/SAIC MTADs system (top row) and on the other hand acquired *in situ* at SLO with Geometrics’ MetalMapper. The geometric mean curves derived from the data acquired with the two systems are virtually identical when viewed logarithmically.

³¹ The TEMTADs data were acquired with a time bandwidth of 25ms and a smaller decimation factor (5%).

bandwidths and logarithmic window sampling parameters, we elected a simpler procedure to affect a quantitative comparison as we explain below.

Comparison of Composite “Beta” or P_0 ’s – In section 6.3.2 we explained how we derived certain “meta” parameters from the principle polarizability curves. The simplest of these meta-parameters are the 3 P_0 ’s, which are nothing more than a numerical integration of the principal polarizability curve over a specified time window. This integration is standard in our inversion program MMRMP and it was easily performed on the SAIC principle polarizability curves from the SLO seed target objects. We used the composite time gate $100 \leq t \leq 8333 \mu\text{s}$ to compute the parameters P_{0x} , P_{0y} , and P_{0z} . From these three parameters we calculated the transverse polarizability parameter P_{0t} (also explained in section 6.3.2). We can visually compare how the 6 target types plot on a scatter plot as we shown in Figure 7.23. We have calculated the geometric means and the geometric standard deviation for each of the 6 target groups. These values are presented as Table 7.5. The table shows that we are able to reproduce the actual beta values (assumed to be those measured in free-air by SAIC) with an error (1σ) of considerably less than ± 20 , which is our performance objective.

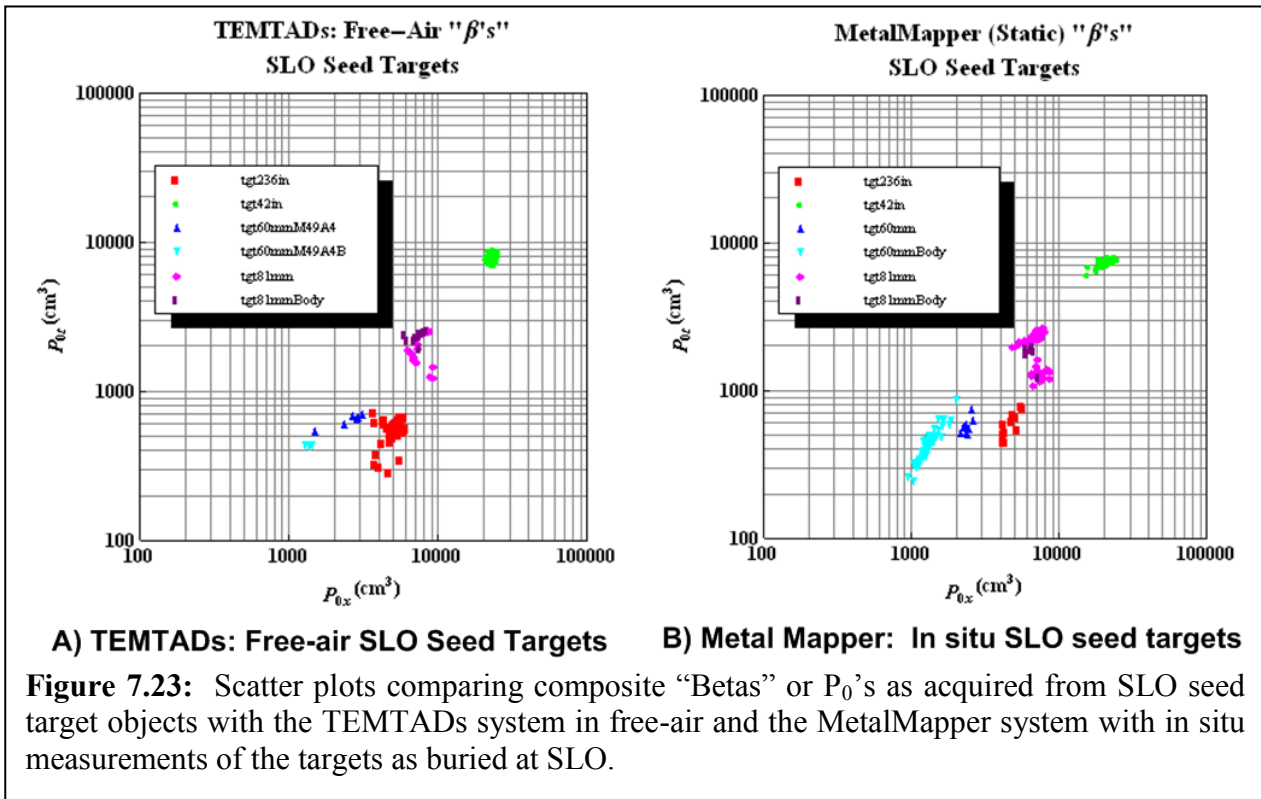


Table 7.5: Table comparing TEMTADs “Betas” to “Betas” recovered by MetalMapper for seed targets at SLO. The table shows that we are able to recover primary “Betas” (P0x) with errors less than $\pm 15\%$ which is well under our performance objective.

Type	TEMTADs	MM	Error	TEMTADs	MM	Error
	Geom. Mean - P0x (cm ³)	Geom. Mean - P0t (cm ³)		Geom. Mean - P0t (cm ³)	Geom. Mean - P0t (cm ³)	
tgt236in	5167	4790	7.30%	538	568	5.60%
tgt42in	23566	20853	11.51%	7804	7304	6.40%
tgt60mm	2524	2403	4.79%	638	571	10.47%
tgt60mmBody	1374	1325	3.52%	430	426	0.91%
tgt81mm	7560	7018	7.17%	1896	1842	2.84%
tgt81mmBody	7468	6460	13.49%	2295	1747	23.86%

7.9. Dynamic-Mode Survey Productivity

Our performance objective for dynamic-mode survey productivity was 1.2 Acres/day. In Table 7.6, we have tabulated the work time for each of the sub-areas that we defined within the overall demonstration area. These time intervals (Δt) represent the time between the first and last dynamic calibration of the day (or last calibration for a particular sub-area survey) and therefore include time for breaks/breakdowns. What those time intervals do not include is the time for set-up and take-down each day. We estimate that time to be 0.5 hr/day. We based our production estimates on the number of work hours. At SLO, we generally worked about 9-10 hrs in the field. Therefore, we converted hourly production to daily production by multiplying by 9 hr/day. Based on the table, we met our slightly exceeded our production goal ($0.054 \text{ ha/hr} = 0.49 \text{ ha/day} = 1.22 \text{ acre/day}$).

We also tabulated dynamic data production for the MetalMapper demonstration at APG (see Table 7.7). At APG, the mapping mode survey productivity was significantly larger ($\sim 0.07 \text{ ha/hr} \sim 0.56 \text{ ha/day} = 1.4 \text{ acre/day}$).³² This was due in large part we think because the survey lines over both Indirect Fire and Direct Fire areas were approximately 100m. This reduced the number of turn-arounds at the end of each survey line.

The tables show that, at both SLO and APG, we have met or exceeded our performance goal for dynamic-mode survey productivity (1.2 acre/day).

³² For APG, we based our daily production estimate on an 8-hr field day (plus 0.5hr for set-up and take-down). Based on the 9-hr field day that we used for the SLO estimates, the comparable production rate would be 0.63 ha/day.

Table 7.6: Table showing dynamic survey productivity at SLO.

Sub-Area	Date	Work Time				Production		File No		Blks	Area (ha)
		Start	End	Δt	Δt (hr)	Rte (ha/hr)	Rte (ha/d)	1st	Last		
NWA	5/25/09	12:33	17:45	5:12	5.20	0.035	0.18	1	47	2	0.18
NWB	5/26/09	7:12	14:51	7:39	7.65	0.035	0.27	48	101	3	0.27
NWC	5/26/09	15:48	17:48	2:00	2.00			102	116	6	0.54
NWC	5/27/09	7:16	16:14	8:58	8.97	0.046	0.43	117	232		
NWC	5/28/09	6:59	7:46	0:47	0.78			233	254		
SWA	5/28/09	9:13	15:41	6:28	6.47	0.042	0.27	255	338	3	0.27
SA	5/29/09	6:59	16:51	9:52	9.87	0.055	0.54	339	424	6	0.54
SE	5/30/09	7:11	12:14	5:03	5.05	0.088	0.54	425	516	9.5	0.855
SE-A	5/30/09	12:52	17:32	4:40	4.67			517	576		
E	5/31/09	6:01	15:59	9:58	9.97	0.068	0.68	577	687	7.5	0.675
NE	6/1/09	7:24	17:13	9:49	9.82	0.057	0.56	688	785	6.2	0.558
NE-A	6/2/09	7:41	12:22	4:41	4.68	0.035	0.16	786	861	1.8	0.162
N	6/9/09	5:42	15:47	10:05	10.08	0.071	0.72	862	1061	8	0.72
NWB-Rep	6/15/09	8:45	11:23	2:38	2.63	0.103	0.27	1062	1105	3	0.27
1.1. Totals					87.83	0.054	0.46			53	4.77

Table 7.7: Dynamic survey productivity at APG.

Area	Date	Work Time				Production		File No		Area (ha)
		Start	End	Δt	Δt (hr)	Rte (ha/hr)	Rte (ha/d)	1st	Last	
CG	9/15/08	10:09	13:11	3:02	3.03	0.040	0.32	1	52	0.12
BG	9/16/08	9:09	14:48	5:39	5.65	0.028	0.23	56	119	0.16
IDF	9/19/08	7:17	13:46	6:29	6.48			140	211	1.3
IDF	9/20/08	6:26	11:29	5:03	5.05	0.084	0.67	212	271	
IDF	9/22/08	6:58	10:59	4:01	4.02			272	323	
DF	9/26/08	11:10	14:15	3:05	3.08	0.084	0.67	1	43	0.76
DF	9/27/08	6:25	12:21	5:56	5.93			44	114	
Totals					33.25	0.070	0.56			2.34

7.10. Static-Mode Calibration Repeatability

We placed a steel calibration sphere in the test pit at SLO after we completed the static measurements on specimen targets of interest. During the time period Jun 7-16, 2009, we returned to measure that calibration sphere 20 times. Each measurement consisted of reacquiring the target using the acquisition software to guide the operator backed to the known target position (measured and stored when we buried the target). Each static data set was inverted with MMRMP to get estimates for the 3D target position, and size. We have tabulated the statistics in Table 7.8. And in Figure 7.24 we have plotted the estimates of (horizontal) platform and target position. The table and figure show that we are able to consistently move the MetalMapper platform to within a few centimeters of a designated target position. The repeatability of target position estimates is at the sub-centimeter level. And finally, the estimate of target size (RMS(P_0)) is within $\pm 4.0\%$ (1σ), and the measure of signal strength (SNR) is repeatable to $\pm 4.4\%$ (1σ). These results show that we have easily met our MetalMapper performance goal ($\pm 10\%$ (1σ)) for repeatability based on measuring a reference target.

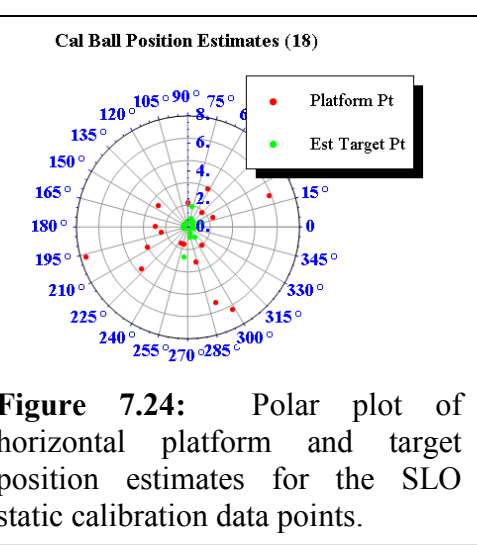


Figure 7.24: Polar plot of horizontal platform and target position estimates for the SLO static calibration data points.

Table 7.8: Summary statistics for static repeatability at SLO. The top table section speaks to the ability to repetitively re-position the platform over the same point. The bottom section contains the statistics for the estimates of target position and size.

Platform Position															
φ (°)		Δr (cm)		z (cm)											
Mean	σ	Mean	σ	Mean	σ										
10.9 ± 11.2		3.3 ± 2.1		N/A											
Target Position & EM Size						SNR									
φ (°)		Δr (cm)		z (cm)		RMS(P_0) (cm ³)									
Mean	σ	Mean	σ	Mean	σ	Mean	σ	Mean	σ	Mean	σ				
-17.7	± 103	0.7	± 0.5	40.4	± 0.6	4078	± 164	301.02	13.37						

7.11. Static-Mode Survey Productivity

Our performance goal at SLO was to acquire greater than 200 static data points per day. As shown in Table 7.9 and Table 7.10. These tables show that, at SLO, we improved static productivity by approximately 39 pts/hr versus 29 pts/hr at APG. At SLO, we measured 494 pts

on our best day.³³ The improved production rates reflect the front-mounted antenna deployment. Secondly, we decreased the stacking time by a factor of 2 because of the generally better SNR at SLO.

Table 7.9: Static-mode survey productivity at Camp SLO.

Area	Date	Work Time				Production		File Index	
		Start	End	Δt	Δt (hr)	Rte (pts/hr)	Rte (pts/d)	1st	Last
Tst Strip	6/3/09	7:27	8:40	1:13	1.22	17	201	2	22
Tst Pit	6/3/09	9:03	10:18	1:15	1.25	27		23	56
Tst Strip	6/8/09	7:39	8:35	0:56	0.93	13	242	57	68
NWC	6/8/09	9:22	14:25	5:03	5.05	43		1	217
NWC	6/10/09	14:37	17:40	3:03	3.05	41	197	364	489
NWB	6/10/09	8:23	11:48	3:25	3.42	43		218	363
NWA	6/10/09	17:41	18:34	0:53	0.88	40		490	524
NEPlus	6/11/09	8:35	15:21	6:46	6.77	40	405	525	795
E	6/11/09	15:33	18:18	2:45	2.75	57		796	952
E	6/12/09	8:13	13:10	4:57	4.95	51	494	953	1205
SEPlus	6/12/09	14:18	18:08	3:50	3.83	60		1206	1434
Splus	6/13/09	8:30	17:01	8:31	8.52	50	449	1435	1859
N	6/14/09	9:46	17:25	7:39	7.65	42	375	1860	2178
Stat-Rep	6/15/09	12:40	18:42	6:02	6.03	17	155	2179	2282
Stat-Rep	6/16/09	8:47	17:33	8:46	8.77	24	216	2283	2492
Totals					65.07	39	354	2559	

³³ At SLO, our access to the site was unrestricted. We generally stayed a full 10 hrs at the site. Daily production rates at SLO partly reflect longer work days than at APG. For comparing production rates it is better to use the hourly rates.

Table 7.10: Static-mode survey productivity at APG

Area	Date	Work Time			Production		File Index	
		Start	End	Δt (hr)	Rte (pts/hr)	Rte (pts/d)	1st	Last
CG(5%)	9/16/08	7:05	9:13	2.13	38	300	4	83
CG(10%)	9/16/08	13:49	14:43	0.90	34	305	2	32
CG(10%)	9/16/08	6:40	7:33	0.88	42		33	69
BG	9/17/08	7:43	14:47	7.07	27	247	71	264
BG	9/18/08	6:19	13:27	7.13	35		266	512
BG	9/19/08	6:30	7:02	0.53	26		513	526
IDF	9/22/08	14:16	16:31	2.25	25	213	2	58
IDF	9/23/08	6:35	14:50	8.25	25		60	263
IDF	9/24/08	6:45	14:44	7.98	28		265	486
IDF	9/25/08	6:04	14:03	7.98	27		488	703
IDF	9/26/08	6:24	9:59	3.58	28		705	806
DF	9/30/08	14:25	14:37	0.20	25	225	2	6
DF	10/1/08	6:23	13:10	6.78	22		7	158
DF	10/2/08	8:15	16:45	8.50	30		160	413
DF	10/4/08	6:28	10:47	4.32	34		416	561
Totals				68.50	29	229	1961	

8. COST ASSESSMENT

This section should provide sufficient cost information such that a professional involved in the field could reasonably estimate costs for implementation at a given site. In addition, this section should provide a discussion of the cost benefit of the technology. The following subsections with detailed discussions and examples should be provided.

8.1. COST MODEL

In Table 8.1 we provide a cost model for the deployment of the MetalMapper technology.

Table 8.1 Cost Model for a MetalMapper Deployment

Cost Element	Data Tracked During Demonstration	Estimated Costs
Instrument cost	Component costs and integration costs <ul style="list-style-type: none">Engineering estimates based on current developmentLifetime estimate Track consumables and repairs	<ul style="list-style-type: none">\$100K-\$120K
Mobilization and demobilization	Cost to mobilize to site Derived from demonstration costs	<ul style="list-style-type: none">\$20K/\$15K
Instrument setup costs	Unit: \$ cost to set up and calibrate Data Requirements: <ul style="list-style-type: none">0.5 hr22/day	<ul style="list-style-type: none">\$500/day
Survey costs (Dynamic)	Unit: \$ cost per hectare Data requirements: <ul style="list-style-type: none">Hours per hectare – 18 hrPersonnel required - 2	<ul style="list-style-type: none">\$7.2K/ha
Survey costs (Static)	Unit: \$ cost per 300 Targets Data requirements: <ul style="list-style-type: none">Hours – 9 hrPersonnel required - 2	<ul style="list-style-type: none">\$3.6K
Detection data processing costs	Unit: \$ cost per hectare Data requirements: <ul style="list-style-type: none">Time required – 18 hrPersonnel required - 1	<ul style="list-style-type: none">\$6.6K
Discrimination data processing costs	Unit: \$ per 300 anomaly anomalies <ul style="list-style-type: none">Time required – 9hrPersonnel required - 1	<ul style="list-style-type: none">\$3.3K

8.1.1. Equipment Costs

Major sub-systems comprising the MetalMapper system together with their respective cost estimates are listed in Table 8.2.

Table 8.2: Major components comprising a MetalMapper system

MetalMapper Component Name	Cost
Antenna platform and Data Acquisition System (DAQ)	\$65K
RTK GPS System	\$30K
Platform attitude sensor	\$5K
Vehicle Deployment	\$5K-\$20K
Software	\$10K-\$20K

Antenna Platform and DAQ - The antenna platform and the DAQ comprise the proprietary hardware. The platform can be deployed “as is” as a human-powered cart. The instrument containing the DAQ can be mounted on a pack-frame and carried by an operator. In most cases, the system is integrated with an RTK GPS system that periodically generates a NMEA position string to be read by the DAQ. And for precision static measurements, an orientation module is mounted on the antenna platform to sense the three attitude angles (heading, pitch, and roll) of the platform.

RTK GPS System-The location of the antenna platform is normally measured using an RTK GPS system in which the roving antenna is fixed to the antenna platform. The cost of an RTK GPS system (base + rover) is estimated in Table 8.2. However, the cost will vary depending on the manufacturer and the features of the system.

Platform Attitude Sensor-We use an attitude sensing module that contains a 2-axis accelerometer to measure pitch and roll angles and a 3-axis fluxgate magnetometer that provides reference heading to magnetic north. The module output is in the form of ASCI coded RS232C text strings.

Deployment – The MetalMapper can be deployed either as a man-powered cart or as a vehicle-towed system. Deployment in the vehicle-towed mode requires a tow-vehicle such as small lawn tractor. There is a large range of possibilities for tow vehicles and therefore we have provided a cost range for the deployment.

Software-The cost of software required to process MetalMapper data depends on the data type. Map data is processed using Geonics Oasis Montaj (OM) software. We supply a set Geosoft eXecutables (GX’s) that permit MetalMapper data files to be loaded into a Geosoft database (GDB). Standard features of OM are used to edit and further process the data, detect targets, and manage the resulting target lists. OM is not required to process static data. Target parameters are extracted using Geometrics’ proprietary modeling software based on the point dipole model. Results of this target parameterization are placed in a Microsoft Access database. Further processing for discrimination can be performed using standard commercially available software such as MS-Excel, MS-Access, and others.

8.1.2. Mobilization and Demobilization

The cost of mobilization includes the cost of equipment preparation and checkout plus the cost of transportation to the job site. The estimated costs are based on our experience in mobilizing from Grand Junction, CO to job sites at YPG (~1000mi), and APG (~2000mi). The estimated

cost includes labor, transportation, and per diem. Demobilization does not include cost for equipment preparation.

8.1.3. Instrument Setup and Calibration

Instrument setup and calibration procedures require approximately $\frac{1}{2}$ hr at the beginning and at the end of each field day. These procedures include setting up the GPS system, conducting operation checks, and performing static and/or dynamic calibration surveys.

8.1.4. Dynamic Survey Costs

The cost estimate is based on a crew cost of \$3600/day. The estimated areal production is based on survey profiles on 0.75m offsets. Survey speeds are less than 0.5m/s. Production rates can be improved by increasing the survey speed. Production of up to 1 ha/day is possible at a survey speed of 1m/s.

8.1.5. Static Survey Costs

The cost of static surveys is based on an average production rate of 300 static points/day. At APG, we were able to acquire up to 200 pts/day. At SLO we averaged well over 300 pts/day with the antenna array mounted to the front loader of a Kabota 4WD tractor. Production rates will vary depending on the type of deployment.

8.1.6. Detection Data Processing

A single data analyst can process the data produced by a MetalMapper crew. It requires approximately 1hr of the analyst's time per hour of field data production. Processing includes loading the data, producing a detection map, and picking targets. It also includes sequencing the target lists for static surveys.

8.1.7. Discrimination Data Processing

As with detection surveys, a competent data analyst is able to keep up with the processing of the data acquired by the MetalMapper field crew (~300 static points/day). Costs are figured accordingly. Note that these costs do not include the costs of training the discrimination algorithm.

8.2. COST DRIVERS

The cost estimates in Table 8.1 use higher labor costs that reflecting the personnel involved in early demonstrations. These labor costs will no doubt drop by as much as 1/3 as field operations and data processing tasks become routine and are accomplished by lower-level personnel. The productivity of detection surveys is likely to improve by as much as a factor of 2 as we increase survey speed. And finally, the productivity of the data analyst stands to improve markedly as processing tasks are integrated and automated. It is likely that cost of processing will decrease by as much as 50%.

8.3. COST BENEFIT

The cost benefit of employing of advanced EMI technology such the MetalMapper can only be realized to the extent that regulators gain sufficient confidence in the technology that they are comfortable letting targets that have been classified "High Confidence Not Munitions" remain undug in the ground. Based on the cost estimates provided in Table 8.1, the unit cost for "Cued ID" analysis of a target with the MetalMapper is approximately \$20/target with the costs likely to drop rapidly down to \$10/target. The unit cost to dig has been estimated to run between

\$100-\$200/target. The scoring results for the MetalMapper showed that fully 98% of the munitions would have been dug with a corresponding false positive dig rate of less than 10% if the targets had been dug according to the prioritized dig list. This suggests that by employing such dig list in a very conservative manner at least half of the targets could be left in the ground thereby reducing the digging costs by half. Since the MetalMapper static survey and data analysis costs are approximately 10-20% of the cost to dig, the overall cost of remediation would be reduced by 30-40% (i.e., dig 50% of targets and conduct a cued ID target survey with the MetalMapper of 100% of the targets at a cost of 10-20% of the cost to dig).

9. IMPLEMENTATION ISSUES

In Section 8 above, we highlighted the most important issue affecting the implementation of the MetalMapper technology. Clearly, the need is to prove to the authorities that regulate and supervise the remediation of sites contaminated with UXO that the MetalMapper technology can significantly reduce the cost remediation. We think that the ESTCP program office together with regulators and demonstrators are making some headway with their live site demonstration program. Thus far, successful demonstrations at Camp Siebert, AL and Camp San Luis Obispo have been completed. The ESTCP program office plans to continue the live site demonstration program. In 2010, a be a third live site demonstration is scheduled to be conducted at Camp Butner located in the Raleigh-Durham area of North Carolina.

Even with the reduction in the unit survey costs, the cost for deploying the MetalMapper will remain significantly higher than the cost for commercially available EMI technology such as the EM61. And clearly, this higher cost is justified provided that regulating authorities accept the discrimination capability of the system and use the results to reduce the number of unnecessary digs. UXO contractors will no doubt begin to deploy advanced EMI systems such as the MetalMapper only when regulating authorities start specifying the use of such technology in the big requests relating to UXO site remediation. Clearly, it is important that the MetalMapper participated in the demonstration at SLO and performed well. It is equally important that several other data processing demonstrators, using MetalMapper data, performed equally as well.

The MetalMapper system is available as a commercial product by Geometrics, Inc (San Jose, CA). It can be deployed in the field using personnel with same technical skills as those who routinely conduct UXO-related Geophysical Mapping surveys. In some respects, data processing is more demanding. However, we are confident that this too can be routinely performed by geophysical data processors with a few days training.

10. REFERENCES

- [1] T. Bell, H. Nelson, D. George, J. Kingdon, and D. Keiswetter, "EMI Array for Cued UXO Discrimination," in *SEG Las Vegas 2008 Annual Meeting*, Las Vegas, NV, 2008, pp. 2907-2911.
- [2] Defense_Science_Board, "Report of the Defense Science Board Task Force on Unexploded Ordnance," U.S. Dept. of Defense, Washington, DC, November 2003.
- [3] D. D. Snyder, and Dave C George, "Deployment of a Dual-Mode (EM and Magnetic) System for Detection and Classification of UXO at Blossom Point, MD," Blackhawk Geoservices, Inc, Golden, CO, Technical Report, August 1 2005.
- [4] D. D. Snyder, and Dave C George, "Demonstration of the AOL Dual-Mode (EM and Magnetic) System at Blossom Point and Indian Head," Blackhawk Geoservices, Inc, Golden, CO, Technical Report, June 15 2005.
- [5] J. S. McClung, "Standardized UXO Technology Demonstration Site Scoring Record No. 922 (G&G Sciences, Inc)," U.S. Army Aberdeen Test Center, Aberdeen Proving Ground, MD, Final, April 2009.
- [6] D. Teefy, "Standardized UXO Technology Demonstration Site Blind Grid Scoring Record No. 895 (G&G Sciences, Inc)," U.S. Army Aberdeen Test Center, Aberdeen Proving Ground, MD, June 2008.
- [7] G&G_Sciences, "Tests of the AOL-2 System at the UXO Technology Demonstration Site Located at Yuma Proving Grounds," G&G Sciences, Inc, Grand Junction, CO, Field Survey Report, June 2007.
- [8] G&G_Sciences, "Tests of the AOL-2 System at the Mag Test Site - Indian Head, MD," G&G Sciences, Inc, Grand Junction, CO., October 19 2007.
- [9] G&GSciences, "Advanced Ordnance Locator for Standoff Detection & Classification of Surface and Buried UXO," G&G Sciences, Inc, Grand Junction, Final Report, December 2008.
- [10] USAEC. (2009, 12 Oct 2009). *Standardized UXO Technology Demonstration Site Program*. Available: <http://aec.army.mil/usaec/technology/uxo01.html>
- [11] USAEC. (2009, 12 Oct 2009). *Demonstration Sites - Aberdeen Proving Ground (APG)*. Available: <http://aec.army.mil/usaec/technology/uxo01c01.html>
- [12] USAEC. (2009, 12 Oct 2009). *Yuma Proving Ground (YPG)*. Available: <http://aec.army.mil/usaec/technology/uxo01c02.html>
- [13] R. Loder, G. Robitaille, E. Cespedes, T. Berry, D. Teefy, A. Andrews, M. Chambers, B. Kaschenbach, G. Rowe, J. Moulton, S. Nussbaum, S. Patane, D. Reidy, R. Young, and F. Rotondo, "Standardized UXO Technology Demonstration Sites Handbook," U.S. Army Environmental Center, Aberdeen Proving Ground, MD., October 2002.
- [14] USAEC. (2009, 12 Oct 2009). *Demonstrator Scoring Results*. Available: <http://aec.army.mil/usaec/technology/uxo01f.html>
- [15] J. S. McClung, "Standardized UXO Technology Demonstration Site Blind Grid Scoring Record No. 915 (Geometrics, Inc)," U.S. Army Aberdeen Test Center, Aberdeen Proving Grounds, MD., September 2008.
- [16] J. S. McClung, "Standardized UXO Technology Demonstration Site Scoring Record No. 921 (Geometrics, Inc)," U.S. Army Aberdeen Test Center, Aberdeen Proving Ground, MD, FinalApril 2009.

- [17] S. Cazares, and Mike Tuley, "UXO Classification Study: Scoring Memorandum for the former Camp San Luis Obispo, CA," Institute for Defense Analyses, Alexandria, VA, Memorandum, March 20 2009.
- [18] H. H. Nelson, T. Bell, J. Kingdon, N. Khadr, and D.A. Steinhurst, "EM61-MK2 Response of Standard Munitions Items," Naval Research Laboratory, Washington, D.C., Interim NRL/MR/6110-08-9155, 06-10-2008 2008.
- [19] Y. Das, John E. McFee, Jack Toews, and Gregory C. Stuart, "Analysis of an Electromagnetic Induction Detector for Real-Time Location of Buried Objects," *IEEE Trans. Geosci. & Remote Sensing*, vol. 28, pp. 278-288, 1990.
- [20] R. E. Grimm, "Triaxial Modeling and Target Classification of Multichannel, Multicomponent EM Data for UXO Discrimination," *Jour. Envir. & Eng. Geophys*, vol. 8, pp. 239-250, 2003.
- [21] S. MacInnes, Scott Urquhart, and Kenneth Zonge, "Improving UXO Detection with Four-Dimensionsl Matched Filters," in *SAGEEP 2004*, Colorado Springs, CO, 2004.
- [22] H. H. Nelson, and J.R. McDonald, "Multisensor Towed Array Detections System for UXO Detection," *IEEE Trans Geosci & Rem. Sensing*, vol. 39, p. 7, June 2001.
- [23] J. T. Smith, H. Frank Morrison, "Estimating Equivalent Dipole Polarizabilities for the Inductive Response of Isolated Conductive Bodies," *IEEE Trans. on Geosc. & Rem. Sens.*, vol. 42, pp. 1208-1214, 2004.
- [24] L. R. Pasion, "Inversion of Time Domain Electromagnetic Data for the Detection of Unexploded Ordnance," Ph.D. PhD Department of Earth and Ocean Sciences, University of British Columbia, Vancouver, B.C., 2007.
- [25] J. T. Smith, H. Frank Morrison, "Estimating Equivalent Dipole Polarizabilities for the Inductive Response of Isolated Conductive Bodies," *IEEE Trans. Geosci. & Rem. Sens.*, vol. 42, pp. 1208-1214, 2004.
- [26] T. Bell, Barrow, B., and Miller, J.T., "Subsurface discrimination using electromagnetic Induction Sensors," *IEEE Trans. on Geosc. & Rem. Sens.*, vol. 39, pp. 1279-1285, 2001.
- [27] L. R. Pasion, and D.W. Oldenburg, "A Discrimination Algorithm for UXO Using Time Domain Electromagnetics," *Jour. Eng. & Envir. Geophys.*, pp. 91-102, 2001.
- [28] J. T. Smith, and H. Frank Morrison, and Alex Becker, "Parametric Forms and the Inductive Response of a Permeable Sphere," *Jour. Envir. & Eng. Geophys*, vol. 9, pp. 213-216, 2004.
- [29] A. Kaufman, "Frequency and Transient Responses of Electromagnetic Fields Created by Currents in Confined Conductors," *Geophysics*, vol. 43, pp. 1002-1010, 1978.
- [30] R. S. Smith, and Terry J. Jones, "The moments of the impulse response: A new paradigm for the interpretation of transient electromagnetic data," *Geophysics*, vol. 67, pp. 1095-1103, 2002.

APPENDICES

Appendix A: Points of Contact

POINT OF CONTACT Name	ORGANIZATION Name Address	Phone Fax E-mail	Role in Project
Mark Prouty	Geometrics, Inc 2190 Fortune Drive San Jose, CA 95131	408-428-4212 408-954-0902 markp@geometrics.com	Principal Investigator